Surface Wettability Impact on Water Management in PEM Fuel Cell

by

Saher Al Shakhshir

A thesis
presented to the University of Waterloo
in fulfillment of the
thesis requirement for the degree of
Doctor of Philosophy
in
Mechanical Engineering

Waterloo, Ontario, Canada, 2012

AUTHOR'S DECLARATION

I hereby declare that I am the sole author of this thesis. This is a true copy of the thesis, including any required final revisions, as accepted by my examiners.
I understand that my thesis may be made electronically available to the public.

Saher Al Shakhshir

Abstract

Excessive water formation inside the polymer electrolyte membrane (PEM) fuel cell's structures leads to the flooding of the cathode gas diffusion layer (GDL) and cathode gas flow channels. This results in a negative impact on water management and the overall cell performance. Liquid water generated in the cathode catalyst layer and the water moved from anode to cathode side due to electro-osmotic drag transport through the GDL to reach the gas flow field channels, where it is removed by air cathode gas stream. Due to high and uniform capillary force distribution effect of the pores through the GDL plane and surface tension between the water droplets and gas flow field channels surfaces, liquid water tends to block/fill the pores of the GDL and stick to the surface of the GDL and gas flow channels. Therefore, it is difficult to remove the trapped water in GDL structure which can lead to flood of the PEM fuel cell. The GDL surfaces are commonly treated uniformly with a hydrophobic material in order to overcome the flooding phenomena inside PEM fuel cell. Despite the importance impact of the surface wettability of both channel and GDL surface characteristics especially for the cathode side on the water management, few experimental studies have been conducted to investigate the effect of the two-phase flow in cathode gas flow channel and their crucial role.

The work presented in this thesis covers contributions that provide insight, not only into the investigation of the effects of hydrophobic cathode GDL and cathode gas flow channels, on water removal, two phase flow inside the channel, and on PEM fuel cell performance, but also the superhydrophobic and superhydrophilic GDLs and gas flow channels effects. Further, the effects of a novel GDL designs with sandwich and gradient wettability with driving capillary force through GDL plane have been investigated.

Two-phase flow especially in the cathode gas flow field channels of PEM fuel cell has a crucial role on water removal. Hence, in this research, ex-situ investigations of the effects of channels with different surface wettability; superhydrophobic, hydrophobic, slightly hydrophobic, and superhydrophilic on the two-phase flow characteristics have been tested and visualized at room temperature. Pressure drop measurements and two-phase flow visualization have been carried out using high speed camera.

The effect of the various coating materials on graphite and GDL surface morphology, roughness, static contact angle (θ), and sliding contact angle (α) have been investigated using scanning electron microscopy (SEM), Profilometry, and sessile drop technique, respectively. It has been observed that the two-phase flow resistance is considerably affected by surface wettability of the channels. Further, the overall cell performance can be improved by superhydrophobic gas flow channels mainly at high current density over slightly hydrophobic and superhydrophilic cases tested.

In addition, sandwich wettability GDL has been coated with a silica particle/ Polydimethylsiloxane (PDMS) composite. The porometric characteristics have been studied using, method of standard porosimetry (MSP). It has been found that sandwich wettability GDL has superhydrophobic surfaces with ($\theta = 162\pm2^\circ$), ($\alpha = 5\pm1^\circ$), and the internal pores are hydrophilic, while the mean pore radius is $7.1\mu m$. This shows a low resistance to gas transport. On the other hand, performance testing indicates that (PEM) fuel cell equipped with sandwich wettability GDL results in the best performance compared to those with raw (non-coated) (slightly hydrophobic), PTFE coated (commercial with micro-porous layer (MPL)) (superhydrophobic), and silica coated (superhydrophilic) GDL.

The wettability gradient has been introduced through plane of the one side hydrophobic GDL by coating one side of non-coated GDL with 15 wt. % of PTFE solution; however, the other side remains uncoated. The effects of wettability gradient on the water removal rate, droplet dynamics, and PEM fuel cell performance have been covered in this thesis. Water removal rate is determined using a 20 ml syringe barrel, wherein a 13 mm diameter GDL token is fixed on the barrel opening. The droplets penetrating through the GDL are visualized via a high speed camera to study the droplets' dynamic characteristics. The GDL wettability gradient has a significant impact on water removal rate, droplets' dynamic characteristics, and consequently enhances the overall PEM fuel cell performance.

Acknowledgements

This thesis would not have been possible without the guidance and the help of several individuals who in one way or another contributed and extended their valuable assistance in the preparation and completion of this work.

First and foremost, my gratitude to Professor Xianguo Li, my advisor, for all his time, support and efforts in this study and securing funds for maintaining the lab and supplying equipment. Members of 20/20 Laboratory Fuel Cells and Green Energy RD&D group, who helped me with their valuable knowledge.

I appreciate the opportunity of working with wide range of experts and supportive post-doctoral fellows, students, staffs and researchers at University of Waterloo.

Ibrahim Alaefour, my friend and colleague who helped me with his technical expertise in the experiments and encouraged me throughout the work.

Dr. Yongxin Wang who worked side by side with me, Dr. Ehab Abu Ramadan for his direct help and guidance in proof editing of some of my manuscripts, and Dr. Yongtaek Lee for his valuable help and consultation. I appreciate their time and efforts.

Thermal Fluids Lab Technician, Jason Benninger and Electronics Technician, Neil Griffett, for their technical support in manufacturing some of the parts and building the apparatuses. I am grateful for their assistance and The Optikon Corporation Ltd. for providing us their high speed camera system and associated expertise for the two-phase flow imaging reported in this study and Aaron Pereira - Lab. Administrator for his efforts, presence and observance in the lab, which made the work smoother.

Last but not the least, my family especially my parents who always support me with their unconditional love and never questioned my wisdom during my time studding away from home. The value of their support and of their belief in me is immeasurable.

My youngest brother Thaer showed his full support and understanding during his stay with me in the last three years of this project. He always pushed me to work harder and inspired me. I am grateful to have him in my life.

Table of Contents

List of Figures

List of Tables

Nomenclature

Alphabets

V_{rev}	Reversible Cell Potential	(V)
V_{cell}	Cell Voltage	(V)
J	Current Density	(A/cm^2)
a	Channel Width	(mm)
b	Channel Depth	(mm)
w	Land Width	(mm)
P	Pressure	(kPag)
T	Temperature	(°C)
R	Universal Gas Constant (8.3143)	(J/mol K)
l	Channel Length	(mm)
D_h	Hydraulic Diameter	(m)
$\dot{m}$	Mass Flow Rate	(kg/s)
Δp	Pressure Drop in Channels	(kPa)
Re	Reynolds Number	
v	Channel Air Velocity	(m/s)
V_g	Gas Kinetic Viscosity	
Pc	Capillary Pressure	(KPag)
Q	Volumetric Flow Rate	(m^3/s)
r	Maximum Radius of Pore Filled with Liquid	(µm)
s	Roughness Factor	

Abbreviations

PEM	Polymer Electrolyte Membrane
MEA	Membrane Electrode Assembly
PFSA	Perfluorosulfonic Acid

PTFE	Polytetrafluoroethylene	
Pt	Platinum	
CL	Catalyst Layer	
ORR	Oxygen Reduction Reaction	
HOR	Hydrogen Oxidation Reaction	
RH	Relative Humidity	
GDL	Gas Diffusion Layer	
CCD	Charge-Coupled Device	
CV	Coefficient of Variation	
CMOS	Complementary Metal–Oxide–Semiconductor	
SP	Silica Particles	
MPL	Micro Porous Layer	
S	Saturation	

Subscripts

w	Wetting	
nw	Non Wetting	
G	Gas	
L	Liquid	
S	Solid	
O_2	Oxygen	
H_2	Hydrogen	
i	Inlet Cross-Sectional Area	(m^2)
sb	Standard Body	
ob	Object Body	

Greek Letters

μ	Viscosity	(kg/m.s)

ρ	Density	(kg/m^3)
η	Over potential	(V)
γ	Interfacial Surface Tension	(N/m)
θ	Static Contact angle	(°)
α	Sliding angle	(°)
σ	Standard Deviation	

Chapter 1

Introduction

1.1 Background

Fuel cell is an electrochemical device that converts chemical energy of reactants directly into electrical energy. Polymer electrolyte membrane (PEM) fuel cell is one of the common types of the fuel cells. It has smaller volume and lighter weight compared to other fuel cell types. Furthermore, it operates at a relatively low temperature range between the freezing and boiling point of water. This contributes to its quick start-up and shut-down phenomena. In addition electrolyte is a solid material which makes the technology attractive for portable equipment and automotive applications. All these characteristics justify the fact that approximately 90% of fuel cell research and development work involves PEM fuel cell in most major automobile and electronic companies [1].

Recently, significant efforts have been made on investigating water management inside PEM fuel cell. Majority of the work was focused on studying water removal from the gas diffusion layer (GDL). Certainly more research is required to investigate water removal from the GDL and gas flow field channels. Flow blockage in the gas flow channels results in lowering the cell performance due to high surface tension. Removing this blockage requires high gas stream velocity to force the liquid water out of the cell. This involves significant power consumption for more air compression. In serpentine flow channel design, which has become an industry standard in PEM fuel cell, the needed power to purge the flow blockage out of the cell reaches to 35% of the fuel cell stack output. Therefore, facilitation of liquid water removal from the flow channel surfaces can have significant impact on enhancing the PEM fuel cell performance and cost reduction. The main concern in this work is to modify the wettability of flow channels and the GDL surfaces with different surface wettability so it can facilitate the water removal. Further, the effect of this modification on water removal from, and performance of the PEM fuel cell will be investigated.

1.2 Polymer Electrolyte Membrane (PEM) Fuel Cell

A schematic diagram of PEM fuel cell is shown in Figure1.1, which illustrates its operational principles. A PEM fuel cell is consist of number of major components; each of which has its own specific role in completing PEM fuel cell operating process. These will be explained in following sections.

Pure fully humidified hydrogen enters the anode channel and diffuses through the gas diffusion layer (GDL) towards the anode catalyst layer (CL). At the interface between the anode catalyst and the membrane electrolyte, fuel is converted to protons (H^+) and electrons (e^-). This is due to the effect of platinum which exists in the CL. The reaction is according to *hydrogen oxidation reaction* (HOR) as follows:

$$H_2 \rightarrow 2H^+ + 2e^- \qquad \textbf{1.1}$$

The unique property of the membrane electrolyte allows protons to transport to the cathode side and it prohibits the electron to pass. This property avoids cell shortening and forces the electrons to travel through the external circuit and deliver electric energy to the external load while reaching cathode.

At the cathode side, the transferred protons and the energy depleted electrons combine with oxygen in the cathode CL to produce water according to the following *oxygen reduction reaction* (ORR):

$${}^{1}/_{2}\,O_2 + 2H^+ + 2e^- \rightarrow H_2O \qquad \textbf{1.2}$$

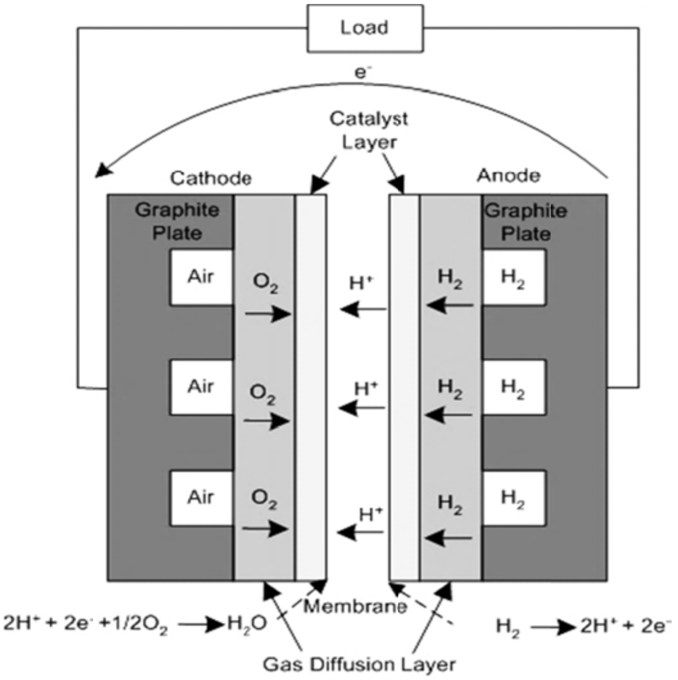

Figure 1.1: Schematic and operational principle of PEM fuel cell.

HOR is slightly endothermic and ORR is strongly exothermic, therefore heat is generated. Combining the anode-reaction and cathode-reaction together results in the overall reaction in PEM fuel cell:

$$H_2 + 2O_2 \rightarrow H_2O + \hbar eat + electric\ energy \tag{1.3}$$

Perfluorosulfonic acid (PFSA) is the most commonly used membrane material for PEM fuel cells. When the membrane becomes hydrated, the hydrogen ions (H^+) become mobile by bonding to the water molecules to form hydronium ions; these ions move between the sulfonic acid sites. The water content of the polymer electrolyte is essential for proton conduction; if the membrane becomes dehydrated, it will no longer be protonically conductive. Nafion® 112, 115, and 117 from DuPont are commonly used membranes in PEM fuel cells.

Catalyst layer (CL) is a thin layer (several microns to several tens of microns thick) on either side of the membrane. It usually consists of micro scale carbon particles, each of which can support nano scale platinum (Pt) catalyst particles, loosely embedded in a matrix of ionomer. HOR occurs in the anode CL, and ORR occurs in the cathode CL. The electrochemical reaction is not evenly distributed over the catalyst layer; therefore, the Pt particles must be properly distributed in the catalyst layer to maximize the reaction efficiency and minimize the cost.

Gas diffusion layer (GDL) is typically consists of randomly aligned carbon fibers (carbon paper) or woven spun yarns (carbon cloth) which have high porosity, with thickness ranging from 200 to 300μm. GDL transports the reactants toward the reaction sites and provide structural support for the catalyst layer. Further, they provide a path for electron transfer. It can be said that GDL plays significant role in water management and heat removal with regard to reaction sites of the cell.

After production of water at the cathode side, this water is discharged out of the cell through the gas flow field channels. For this reason the wettability of the channel surface is important for liquid water removal.

1.3 PEM Fuel Cell Performance

The typical performance of the fuel cell is shown in the form of current density J versus cell voltage V_{cell} plots, known as the *polarization curve* as shown in Figure1.2. This curve provides the steady state performance of a given fuel cell. The variation of individual cell voltage versus J is found from the maximum cell voltage and the various voltage losses. The sources of these losses, which are also called polarization, irreversibility or overvoltage, originate from: a) Activation polarization, b) Ohmic polarization, and c) Concentration (mass transport) polarization. The summation of these over potentials is known as the cell over potential, η_{cell}.

The maximum cell voltage, or reversible voltage, V_{rev} represents an ideal cell performance, and is independent of the quantity of current drawn from the cell. However, for a real fuel cell, irreversible voltage losses are considered.

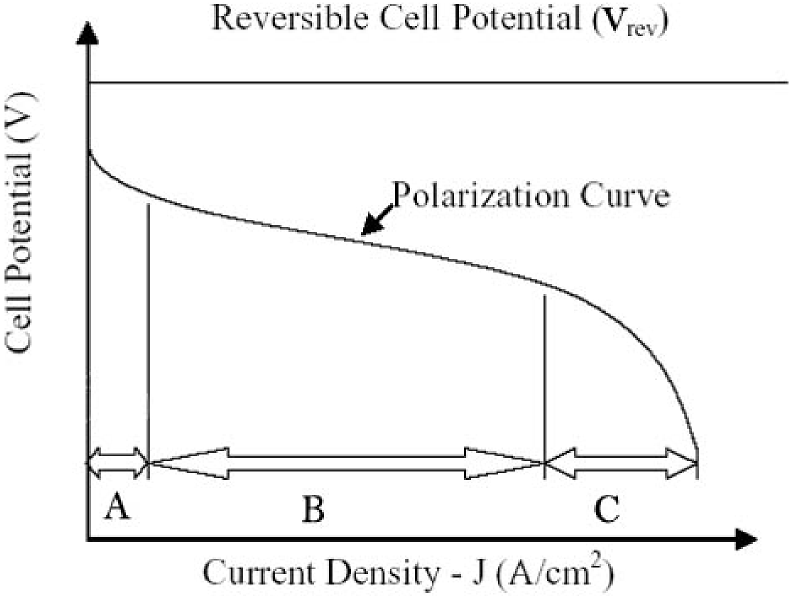

Figure 1.2: Schematic typical polarization curve showing three regions; (A) Activation polarization, (B) Ohmic polarization, and (C) Concentration polarization

In region A of Figure1.2 the reaction rate loss takes place. This region is called the *Activation polarization* region, which dominates at low current densities. It is present when the rate of the electrochemical reaction at an electrode surface is controlled by sluggish electrode kinetics. Activation losses increase as current drawn from the cell is increased.

In region B, *Ohmic polarization* dominates due to the resistances of the polymer electrolyte membrane to the ion transfer and of the rest of cell assembly to the electron transfer. Hence, the cell voltage drops steadily as current drawn is increased.

The third region C is known as the *Concentration polarization* region. This is due to the fact that the reactant concentration at the reaction sites decreases while current drawn from the cell is increased as a result of the limited rate of mass transfer. This loss becomes significant at high current densities.

Cathode performance is one of the key factors affecting fuel cell performance. Hence, the liquid water imposes transport limitation especially at high current densities. It is often difficult to remove the product water from the cathode side of the fuel cell, which leads to the compromised transfer of oxygen to the reaction sites through the GDL. The liquid water formed on the cathode CL transports through the GDL to reach gas flow channels, and later it is removed from the gas flow channels by cathode air stream. Due to high surface tension effect, liquid water clogs the flow channels and fills the pores of the GDL. The imbalance between water generation rate at the reaction sites and water removal rate from the flow channels leads to water flooding in the flow channels. Thus, water management a fairly complex phenomenon- is critical to PEM fuel cell, and is significantly influenced by water removal.

Changing the gas flow field channel surface wettability (such as the static contact angle and sliding angle), is relatively one of the conventional used techniques to enhance water removal from the flow channel. Hydrophobic coating for the gas flow channel has a direct effect on increasing the cell performance. While it reduces the required drag force which applied by air flow to drive the flow out of the channel, the cell performance increases. Polytetrafluoroethylene (PTFE) was extensively used to change the gas flow channel surface to hydrophobic surface. However, obtaining other surface properties such as the range between superhydrophobic to superhydrophilic requires applying different coating materials.

PTFE and its derivatives such as; polyvinylidene fluoride [2] and fluorinated ethylene propylene [3] are commonly used to treat the GDL to become more hydrophobic. GDL was dipped into the PTFE suspension or sprayed depositing with a mixture of PTFE and carbon powder which resulted in a uniformly PTFE treated GDL, resulting in a uniform capillary force through GDL plane. The PTFE loading should be carefully controlled. Sufficient loading is required to provide water repellant effect; while excess loading will likely decrease the water transport through GDL. Hence it is clear that, excess PTFE will decrease GDL structure and conductivity. This limits the amount of transported gases through GDL to the reaction sites, and lowers the thermal and electrical conductivity since PTFE is a non-conductive polymer. Further, a uniform capillary force distribution through GDL plane might slow down the water transport through GDL. Thus, another coating technique and/or material are required to modify the GDL surface wettability without changing the GDL structure and properties and to create a driving capillary force through GDL plane.

1.4 Advantages and Limitations

Graphite is the most common used material in gas flow field channels bipolar plate. It has a rough surface [4]. The static water contact angle (θ) is around 95° on non-coated graphite surface as measured in this work. Water droplets usually stick on this surface, and are difficult to be removed even by strong air flow. The appropriate design of flow channels built on the bipolar plates is critical to the tackling of water management. Serpentine flow field channel layout [5] is the most widely used layout which is often regarded as "industry standard". This is due to the fact that under constant / steady operating and design conditions, PEM fuel cells with serpentine flow field channels tend to have the best performance and durability. In this study for the purpose of flow channel graphite material and the serpentine design PEM fuel flow field design are deployed

In two-phase flow of mini-size channels, the capillary force is mostly negligible compared to the inertia and viscous forces. However, as the cross section area of the flow channel gets smaller , which is 1×1 mm in PEM fuel cell, the capillary effect starts to play an important role in determining the behaviour of two-phase flow patterns. In this case, the interfacial tensions between solid-liquid (γ_{SL}) and solid-gas (γ_{SG}) along with the surface tension between liquid and gas (γ_{LG}); should be considered. In other words, surface properties of the channel walls and the GDL surface as well as combinations of the gas and the liquid are other important factors which require to be emphasised in determining the flow behaviour in the gas flow channel.

Gas Diffusion layer (GDL) is commercially available in two different materials; carbon fiber based porous materials and carbon cloth based porous material. Carbon fiber based porous materials are made hydrophobic by adding PTFE to facilitate liquid water removal. Carbon paper is a non-woven carbon composite, while carbon cloth is a woven fabric. There are two major structural differences between the two materials; carbon cloth is more porous and less tortuous than carbon paper and liquid water coverage on carbon cloth is less than that on carbon paper. Due to the ease of applying a micro-porous layer to carbon paper, carbon paper is usually used as the GDL of PEM fuel cells [6]. In this thesis research, the experiments are based on carbon paper material; thus, the term GDL refers to a carbon paper sample.

1.5 Wettability of Solid Surfaces

The wettability and water repellency of the solid surface are important material properties. They strongly depend on both surface composition and the surface roughness [7]. While surface wettability indicates the hydrophilic characteristic of the surface, water repellency specifies hydrophobic characteristics.

The wettability of the solid surface may be evaluated by the contact angle given by Young's Equation:

$$\cos\theta = \frac{\gamma_{SG} - \gamma_{SL}}{\gamma_{LG}} \qquad \textbf{1.4}$$

Where γ_{SL}, γ_{SV} and γ_{LV} are interfacial free energies per unit area of the solid-liquid, solid-gas and liquid-gas interface respectively. The maximum contact angle can be obtained on a flat surface merely by lowering the surface energy [8]. The lowest recorded surface energy is 6.7 mJm^{-2}. It characterizes a surface with regularly aligned closest-hexagonal-packed Trifluoromethyl (CF_3) groups [9]. The calculated contact angle for this surface is 120° [10]. This angle is relatively small compared with the superhydrophobic contact angle 150° [11]. Other techniques should be used with surface coating to increase the contact angle to a superhydrophobic contact angle. For this purpose, creation of complex surface structure by changing the surface roughness and make it more homogeneous as one of these techniques is used to increase the hydrophobicity of the surface's contact angle [12].

Young's equation is applicable only on a flat surface. Modifications are required to account for rough surfaces. Wenzel proposed a model describing the contact angle θ' on a rough surface. He modified Young's equation as follows [13]:

$$\cos\theta' = \frac{s(\gamma_{SG} - \gamma_{SL})}{\gamma_{LG}} = s\cos\theta \qquad \textbf{1.5}$$

Where s is the roughness factor; defined as the ratio of the actual area of a rough surface to the geometric projected area. Since s value is greater than unity, the surface roughness enhances the hydrophobicity of the hydrophobic surfaces.

Using a gradient of some type can facilitate the water droplet to move along a solid surface [12]. On the thermal gradient, the drop will move from the warm side to the cool side. This movement is due to the fact that liquid-gas surface tension is affected by temperature. As temperature increases, surface tension decreases, and vice versa. On each area element at the liquid-gas interface, there are two forces pulling in opposite directions which tend to reduce the surface area of the drop. Since surface tension decreases with increasing temperature, the droplet is driven into the higher surface tension value (the coldest one). In other words, tension pulling in the cold direction is stronger than the one pulling in the warm direction. On a wettability gradient, a drop of a hydrophilic substance will move from the hydrophobic end to the hydrophilic end. This is attributed to the fact that the total energy of the system is at minimum when the drop is at the hydrophilic end of the gradient [14].

1.6 Thesis Objectives

According to previous discussion the surface wettability of the gas flow channel and GDL have a crucial role on the PEM fuel cell water management, thus the objective of this thesis will be divided into two parts.

1) To investigate the effect of the gas flow field channels with different surface wettability; superhydrophobic, slightly hydrophobic, hydrophobic, superhydrophilic, and combined surface wettability channel (channel's side walls are slightly hydrophobic and channel's bottom surface is superhydrophobic) on;

    a) Two-phase (Air-DI water) flow characteristics in one single channel,

    b) Pressure drop through the channel, and

    c) PEM fuel cell performance.

    This requires;

    i) Characterization of the graphite surface coated with different materials. This task covers below stages;

        (1) Analysis of surface topography,

        (2) Measurement of static contact angle (θ) and sliding contact angle (α),

        (3) Measurement of surface roughness,

        (4) Analysis and comparison of acquired data, and

        (5) Understanding the interaction between the graphite surfaces coated with different materials and liquid water on the coated surface.

    ii) Design and built an experimental set-up to perform;

        (1) An ex-situ visualization for two phase flow in a single channel, and

        (2) Pressure drop measurements through the channel.

    iii) Design and built PEM fuel cells with different cathode gas flow channels' surface wettability; superhydrophobic, slightly hydrophobic, and superhydrophilic,

    iv) Measurement of the PEM fuel cells performances using FCATS-S800 testing station,

    - v) Comparison and interpretation of collected data based on the surface wettability as will be explained in the following chapters, and
    - vi) Recommendation of further research study based on the present results.

2) To Study the effect of novel wettability GDL design referred as, sandwich wettability and one side hydrophobic GDL on;
    - a) GDL characteristics includes; GDL's pore size distribution, capillary pressure, θ, α, and water removal rate, and
    - b) PEM fuel cell performance.

    This involves;

    - i) Study of GDL characteristics using method of standard porosimetry (MSP) before and after modifying GDL wettability,
    - ii) Measurement of water removal rate using a designed and built experimental set-up for this purpose,
    - iii) Design and built of PEM fuel cells with different cathode GDL's with various surface wettability,
    - iv) Measurement of the PEM fuel cell performances using FCATS-S800,
    - v) Comparison and interpretation of deployed data as will be explained in the following chapters, and
    - vi) Finally recommend future work plan based on the obtained results.

1.7 Scope and Outline of Thesis

This work is organized as follows: Effect of gas flow channel and GDL surface wettability on the cell performance and two-phase flow in PEM fuel cell channels will be reviewed in Chapter 2. Experimental setups and procedures which were used in this study will be explained in Chapter 3. Chapter 4 will cover Surface characterization results of the graphite channel with different surface wettability and their effects on two-phase flow in the channel and the cell performance. Further, in this chapter, the GDL characteristics coated with different materials and their effects on PEM fuel cell performance will be discussed. Finally, in Chapter 5 study conclusion and future work recommendations will be presented.

Chapter 2

Literature Review

In this chapter the gas flow channels and GDL surface wettability effects in PEM fuel cell will be reviewed. Many studies were involved in studying the effects of increasing the flow channel hydrophobicity on PEM fuel cell performance, other were involved in studying the effect of hydrophobic and hydrophilic GDL on PEM fuel cell performance. Furthermore, a lot of studies were involved in studying the two-phase flow behaviour in the PEM fuel cell's flow channels. Thus the two-phase flow in the flow channels of the PEM fuel cell will be reviewed in this chapter.

2.1 PEM Fuel Cell Flow Channels Wettability

An extensive research has been done for gas flow channels surface modification, most of this work focused on improving the corrosion resistance and the electrical conductivity [15-29]. However, some researchers gave more attention to the surface wettability of the gas flow channels' surface.

Li *et al.* [30] began the coating process with chemical etching of 1.5 mm thick 316 stainless steel bipolar plate to form flow channels. Then the surface was coated using hollow cathode discharge (HCD) ion plating method with Titanium Nitride (TiN) as coating material. Furthermore, they measured the water contact angle on 316 stainless steel coated with TiN. It was close to the value of graphite contact angle 90° [31], while the uncoated 316 stainless steel was 60°. This indicates that 316 stainless steel gas channels has higher surface energy and more readily floods the cathode side than graphite and TiN-coated 316 stainless steel flow channels.

Lee *et al.* [32] employed the electrochemical theory for 316 stainless steel surface treatment. The work specimen was the anode, and it was immersed in the electrolyte. When it was connected with a cathode, the metallic ions were released from the work specimen to form a passive film. Different metallurgical compositions from the substrate were noticed in the passive film. These compositions increased corrosion-resistance. The surface morphology became smoother and shining. The surface roughness was gently improved and exhibited as a hydrophobic property, which improve the flow of gas and water in the gas channel of the bipolar plate.

Tanigushi and Yasuda [33] used plasma polymerization for titanium and stainless steel plates surface coating. The substrate was treated using combined processes of plasma polymerization and sand-blast pre-treatment. The water droplet static contact angle due to these combined processes was higher than plasma polymerization only. Pre-treatment of sand-blasting offered the significant improvement in water-repellency of the coated surface. This is attributed to the increase in surface roughness of the sand-blasted bipolar plate metals. This result was in accordance with Nakajima *et al.* [34]. Furthermore, the coated channels of PEM fuel cell with the sand-blasting followed by plasma polymerization showed an improvement in the PEM fuel cell's peak power. This improvement referred to the effective flow in the coated channel at low oxygen flow rate.

Low oxygen flow rate is important for improvement of the fuel cell system efficiency. Hence, high flow rate results in low oxidant utilization and larger power consumption for driving air compressor or blower to supply air as an oxidant to the fuel cell. Moreover, blocking the gas flow channel by condensed liquid water results in serious degradation as electrode area, reactant utilization, and humidifying temperature decrease [35].

2.2 PEM Fuel Cell Gas Diffusion Layer (GDL) Wettability

Wettability of the GDL is one of the properties which have a dominant role in controlling the transported water through the GDL. This property is controlled by adding a hydrophobic agent such as Polytetrafluoroethylene (PTFE) to increase its hydrophobicity and to enhance the water removal. Meanwhile, other researchers have added hydrophilic alumosilicate fibers on the GDL surface to improve the water removal [36].

The hydrophobic pores' surface distorts the molecular force balance at the line of contact, which results in forcing the liquid water to move towards an unstable state as depicted in Figure 2.1a. Unlike the hydrophilic treatment, the water is preferentially adsorbed by the fiber surface of the hydrophilic pores as shown in Figure 2.1b [37].

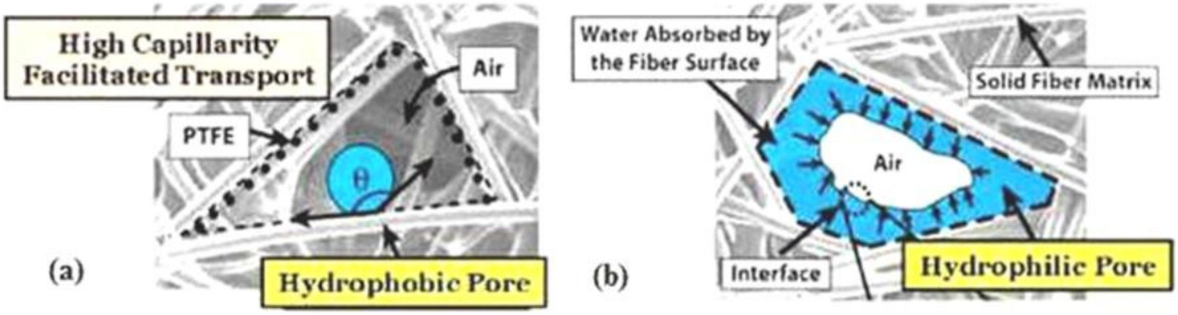

Figure 2.1: Liquid water droplet behavior inside pore of the GDL (a) hydrophobic pore and (b) hydrophilic pore [38].

Bevers *et al.* [37] coated a 9 cm × 9 cm carbon paper sample by PTFE. To coat the paper with PTFE, the sample was slowly lowered into PTFE suspension, never faster the suspension could absorb the paper. The paper was left standing in the suspension for 5 minutes and then removed. To guarantee a PTFE uniform distribution, the paper was laid out flat on a square arrangement of 13 needles (pointed ends up) to dry and then sintered in a sintering oven at a temperature less than 200 °C. They concluded that PTFE contents correlate negatively with conductivity, and the diffusion rate. While the sintering temperature correlates positively with the diffusion rate and negatively with the conductivity. This result was in agreement with Paganin *et al.* [39]. They prepared many GDL samples with different PTFE loadings. The 15 wt. % loading showed the best cell performance.

Giorgi *et al.* [40] coated the GDL with PTFE. A homogeneous suspension was prepared by mixing and stirring in an ultrasonic bath at room temperature for 25 min the carbon with an appropriate amount of PTFE dispersion. They obtained the best performance at the lowest PTFE loading 15 wt. %. On the other hand it was not possible to reduce the PTFE content to zero to avoid the electrode flooding for lack of hydrophobicity. Further, they pointed out that the minimum amount of PTFE in the GDL is necessary to bond the carbon particles together.

Lim and Wang *et al.* [3] treated GDL with fluorinated ethylene propylene (FEP) ranging from 10 to 40 wt. %. The GDL carbon paper was slowly dipped into FEP suspension, diluted to 20wt. % with de-ionized water. To obtain a uniform FEP distribution inside the GDL the sample was heat treated and sintered. The contact angle measurements indicated a similar level of hydrophobicity among GDLs impregnated with different amounts of FEP ranging from 10 to 40 wt. %. However, the contact angle was found to be a strong function of temperature, with the value close to 80 °C water temperature. Furthermore, the 10 wt. % FEP GDL cell gave the highest PEM fuel cell power density. This attributed to the fact that an excessive FEP impregnation results in significant blockage of pores' surface by thin FEP film as depicted in Figure 2.2, and hence a highly restricted surface for reactant transport and product removal.

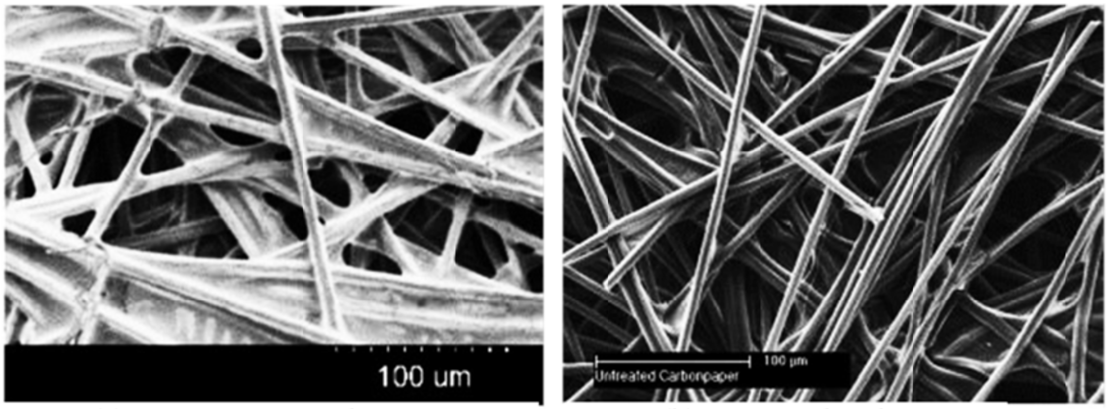

(a) 20 wt.% FEP carbon paper (b) Untreated carbon paper

Figure 2.2: Comparison of surface scanning electron microscopy (SEM) micrographs of carbon paper impregnated with; (a) 20 wt. % FEP (b) untreated [3].

Wang *et al.* [41] studied the effect of PTFE content on the static contact angle. In addition to that he studied the effect of carbonization treatment on the contact angle for the same PTFE content. In their work the cell with 10 wt. % PTFE carbonized GDL has the best performance, this attributed to the highest contact angle 137±1° for this sample. They concluded that, the contact angle value for hydrophobically treated GDLs does not depend only on the PTFE content, but also the uniformity of the PTFE distribution on the fiber stems and the fibers cross positions. For the non-carbonized carbon paper with low PTFE loading, the PTFE was mainly accumulated on the cross positions of carbon fibers. This results in low contact angle value. However, the carbonization process results in coating both the stem and the cross positions of carbon fiber. This leads to higher contact angle values. In their work the sample was carbonized by dipping the GDL sample into 20wt. % sucrose aqueous solution for 6 hours and then sintered in a tube furnace at 400°C under argon ambience to prevent oxidation. To carbonize all the sucrose the process repeated several times. After that the carbonized and non-carbonized samples were dipped into PTFE emulsion with different concentration in order to obtain different PTFE loadings.

Pai *et al.* [42] employed CF_4 plasma treatment to improve the hydrophobicity of the active carbon fibers (ACF) mats. After CF_4 plasma treatment, the ACF mats were dip-coated in 10 wt. % PTFE solutions. Their results showed that the CF_4 treated samples had the best performance compared with the untreated ones. This attributed to the surface GDL pores of the CF_4 plasma treated ACFs were apparently less sealed or blocked by excessive hydrophobic material residuals. In addition to that, the CF_4 plasma treated ACFs water contact angle and the non-treated ones were measured; 132.8 ± 0.2° and 128.4 ± 0.2° respectively.

Finally, Mukundan *et al.* [36] introduced hydrophilic properties for the MPL of the GDL using hydrophilic alumosilicate fibers. Their study showed that the hydrophilic MPL decreased the mass transport resistance associated with better O_2 diffusion kinetics. Thus the cell performance was improved. They attributed this improvement in cell performance to the hydrophilic pathways in the MPL layer, which wicking the liquid water away from the cathode catalyst layer.

2.3 Two-Phase Flow in PEM Fuel Cell Channels

The results of electro-osmotic drag of water from the humidified H_2 gas stream at the anode side through the membrane and the electrochemical water formation at the cathode side are the net accumulation of excess water in the cathode side of the MEA. In addition, the back diffusion from the cathode to the anode due to water concentration gradient is inadequate to keep the anode side hydrated at high current densities [43]. Furthermore, if the water content increases at the MEA cathode side to high levels, plus the generated droplets due to the condensation of the cathode fully humidified air stream at the channel inlet, due to heat loss at the connection pipeline, and on the channel surface, due to the cooling location behind the flow channel in PEM fuel cell stack, then the cathode GDL floods and liquid water accumulation in the form of droplets can occur in the cathode channels.

Tüber *et al.* [44] conducted an experiment with a PEM fuel cell having a simple bipolar plate with two gas channels. They observed that if the gas flow rates was not sufficient to keep droplets out of the channel either by evaporation or forced convection, a blockage occurred, causing 25% drop in the current density.

Yang *et al.* [45] built an optical PEM fuel cell using a two clear polycarbonate plates were placed outside the current collector plates to constrain the gas flow, and two stainless steel end plates compressed the entire optical cell. They showed a sequence of photographs looking through the top of transparent PEM fuel cell cathode gas channel onto the GDL surface. Between 0 and 180 seconds two discrete water droplets formed in the channel growing continuously on the GDL. By 480 seconds the droplets have grown to the point where their surfaces have contacted the channel surfaces, causing them to merge and then coalesce with more hydrophilic channels wall. Between 480 and 540 seconds the drop on the side wall is expelled to an annular flow regime and new droplets begins to emerge from a close locations to the first two. They observed that water droplets forming in the gas channels, may bridge between the walls of the channels under certain operate conditions. This leads to a partial or complete gas flow channel blockage. They photographed a complete gas flow channel blockage in their study. This blockage can hinder the reactant supply to the membrane, therefore the performance will be degraded significantly [46].

Kim *et al.* [47] designed a transparent PEM fuel cell with 25 cm^2 active area to allow for the visualization of cathode channel from the top with fuel cell performance characteristics. Two-phase flow due to the electrochemical reaction of fuel cell was experimentally investigated. The images photographed by charge-coupled device (CCD) camera with various cell temperatures (30-50 °C) and different inlet humidification levels were presented in this study. Results indicated that the flooding on the cathode side first occurs very close the exit of cathode flow channel. As the fuel cell operating temperature increased, it was found that water droplets evaporated easily because of increased saturation vapor pressure and it might have an influence on lowering the flooding level.

Liu *et al.* [46] used three transparent PEM fuel cells to investigate the liquid water and water flooding inside the PEM fuel cell. The plexiglass was used as a transparent material at the cathode side. The three transparent cells have different flow field channels design; parallel, interdigitated, and cascade flow field. The effects of flow field layout, cell temperature, and cathode gas flow rate and operation time on water build-up and cell performance were studied, respectively. Their results indicated that the liquid water columns accumulated in the cathode flow channels could reduce the effective electrochemical reaction area; this leads to mass transfer limitation resulting in the low cell performance. The water in flow channels at high temperature was much less than that at low temperature. When the water flooding appears, increasing cathode flow rate can remove excess water and lead to better cell performance. The water and gas transfer can be enhanced and the water removal is easier in the interdigitated channels and cascade channels than in the parallel channels. The cell performances of the fuel cells that installed interdigitated flow field or cascade flow field are better than that installed with parallel flow field. The images of liquid water in the cathode channels at different operating time were recorded. The evolution of liquid water removing out of channels was also recorded by high-speed video camera.

Ma *et al.* [48] designed a transparent PEM fuel cell with a single straight channel to study the liquid water transport in the cathode channel. Through this study they monitored water build up and removal in the channel directly. The real-time for water buildup information was determined. Furthermore, the water removal velocity was determined. The pressure drop between the inlet and outlet of the channel (ΔP) was measured during the fuel cell operation and ΔP was recorded. ΔP increased with the increase of water content in the channel and a ΔP sharp decline corresponds to water discharge of water blockage.

Air stream in the channel is forced to flow around these droplets, causing a substantial pressure drops inside the channels. The exact mechanism inside the GDL that trigger the water eruption are not completely known, however, some researchers referred that to the capillary pressure effect and the hydrophobic treatment of the GDL pores to change its wetting characteristics so that water is better expelled [49, 50]. Two cases were observed for water emergence; water droplet emerged away from the land area near the center of the gas flow channels and closer to the channel side walls, or even in contact with them [4, 51]. Water droplet behavior in the gas channel is one of the research topics which investigated experimentally and numerically in the literature, and it is beyond the scope of this work.

Kumbur *et al.* [52] employed a simultaneous visualization for both side and top views of a water droplet inside a 5 mm × 4 mm channel to determine the droplet behavior. They developed an empirical correlation of surface tension of a droplet on surface diffusion layer as a function of PTFE content based on the experimental data. Furthermore, they observed that the removal of the relatively taller droplets is easier than that of relatively spread out droplets and films, due to the squared dependence of the drag force acting on the droplet height, and the linear dependence of the surface adhesion force on droplet chord length.

Theodorakakos *et al.* [53] investigated the detachment of water droplets from carbon porous material surface under the influence of air stream flowing around them inside 2.7 mm × 7 mm channel. They indicated that the droplet shape changes dynamically from its static position, until finally loosing contact from the wall surface and swept away by air.

Bazylak *et al.* [54] employed an experimental apparatus which consists of the gas flow channel apparatus on the fluorescence microscope stage and a schematic of the gas flow channel apparatus in cross section. The GDL is placed between a plexiglass base and a Polydimethylsiloxane (PDMS) channel structure with dimensions (3.7 mm × 4.5 mm). The relatively large channel dimensions were chosen such that droplet emergence and transport could be studied in the absence of sidewall effects. A silicone rubber gasket was placed between the GDL and plexiglass base to prevent leakage. Air was delivered to the gas channel and controlled with a rotameter. Liquid water was injected through the bottom surface of the GDL using a syringe pump connected to the plexiglass base with Teflon FEP tubing. Liquid water was introduced from one side of the GDL from a single localized source and the images were captured using an upright fluorescence microscope through-plane evolution of liquid water transport. To facilitate fluorescence imaging, fluorescent dye was used to tag the liquid phase. They observed that individual droplets emerge, grow, and detach from the GDL. However, it was commonly observed that over time these droplets leave residual liquid water particles on the GDL, which provide pinning sites for other droplets. Droplets became pinned to the GDL due to its high surface roughness and high contact angle hysteresis. Furthermore, a droplet may detach more easily and roll away due to the surface hydrophobicity. Moreover, droplets sitting on this highly rough surface experience fewer tendencies for detachment due to longer contact lines between the droplet and fibers and to the presence of contact angle hysteresis. They observed also, the emergence and detachment of individual droplets was followed by slug formation and channel flooding.

Owejan *et al.* [55] investigated the liquid distribution in flow channels with and without PTFE coating using in-plane neutron radiographs and found large slugs inside the channel without PTFE coating and discrete droplet with PTFE coating. Zhu *et al.* [56] used micro-computed tomography to look in droplet formation in hydrophobic channels and found that droplet did not detach from the GDL before removal, meanwhile in hydrophilic channels, a thin water layer formed at the bottom of the channel away from the GDL. Bayzlak *et al.* [57] experimentally studied the effects of a hydrophobic land surface on droplet removal. They concluded that droplets experience minimal entrapment in the GDL/land interface. Turhan *et al.* [58] used through-plan radiography to analyze the liquid water distribution in flow channels and GDL with and without PTFE coating. They found the PTFE coated channels resulted in discrete water droplets on the walls and higher water removal frequency, whereas in uncoated flow channels liquid forms a film layer around the walls and it is more difficult to purge.

2.4 Summary

The findings of these studies were important in terms of understanding the effect of hydrophobic surface on channel level liquid accumulation and how liquid water interact with the PTFE coated and uncoated channels, but they did not describe the effect of surface wettability ranging from superhydrophobic to superhydrophilic channel due to narrowing their choices with PTFE as a coating material. In this study, silica/PDMS composite coating on graphite channel surface are used to obtain the superhydrophobic surface and silica particles coating to obtain the superhydrophilic ones. Meanwhile, in between these two surfaces the non-coated graphite (slightly hydrophobic), PTFE coated graphite (hydrophobic), combined surface wettability channel (channel side walls are non-coated graphite and channel bottom surface is superhydrophobic coated) are investigated in this study. Furthermore, an advanced and expensive experimental techniques have been used to investigate water transportation and distribution inside an operating PEM fuel cell, including; neutron radiography, nuclear magnetic resonance (NMR), and gas chromatographic (GC) measurements. These technologies have the ability to test a real closed cell without any modifications in the cell design. However, it is hard to investigate the real-time liquid water distribution and removal in the testing section. An optical diagnostics technique was applied to visualize two phase flow inside a single graphite channel as mentioned earlier. This technique gives obvious and more detailed images for the two-phase flow which helps in establishing a comprehensive understanding about the two-phase flow phenomena. However, Optically accessible technology limited by inherent nature, including; the change of the channel surface conditions, the fogging of the windows due to the higher temperature and almost fully saturated gas stream in the flow channels, and in different electrical and thermal conductivity due to the Plexiglass s material [45].

In addition to the gas flow channel, it is apparent from previous research that the treatment of GDL was split into two separate approaches: surface modification with a hydrophobic agent and pore control through a pore-forming agent. However, these two issues can actually be addressed simultaneously. For example, it is well known that the surface wettability of a solid depends on both surface chemical structures and physical configurations [59-63]. A superhydrophobic surface, upon which the static water contact angle is more than 150° and sliding angle less than 5°, may generally be prepared by the combination of low surface energy materials and appropriate surface structure [11, 64-66]. Hence, in the case of GDL treatment, the pore-forming agent could reasonably take two roles, controlling the pore structure, and also making appropriate surface roughness to control the surface wettability. In the present work, a silica particle/PDMS composite are prepared and coated on the GDL. Silica nano-particles are used as a pore-forming agent as well as to adjust the surface roughness and structure of GDL. On one hand, micro pores are blocked but uniform macro pores (about 7 μm) are kept in GDL by these particles; on the other hand, the adjusted surface roughness assisted low surface energy material PDMS to attain the high surface water repellent property of GDL. In this work the silica particles used here are essentially hydrophilic with rich hydroxyl groups on their surfaces. They could make hydrophilic pores in the GDL and reduce the resistance to water transport. Further, in some of the aforementioned studies, researchers focused on a uniformly PTFE treated GDL by dipping it into the PTFE suspension or spray depositing it with a mixture of PTFE and carbon powder, resulting in a uniformly PTFE treated GDL which has a uniform capillary force between the two GDL sides. In this work the raw GDL is coated with PTFE emulsion from one side only, and the other side remained non-coated, resulting in a wettability gradient through GDL plane, resulting in capillary driving force from the low wettable side to the higher wettable one.

Chapter 3

Experimental Apparatuses, Techniques, and Materials

In this chapter, the experimental apparatuses, procedures, setups, techniques, and conditions will be explained and discussed in details. The main objectives of the experimental present techniques are illustrated as follows; firstly, to investigate the effect of different coating materials on graphite surface on surface characteristics, surface wettability, two-phase flow inside the coated graphite single channel, and PEM fuel cell performance. Secondly, to investigate the effects of different coatings materials used to modify the GDL wettability on its characteristics including; surface wettability, pore size distribution, porosity, capillary pressure, water removal rate, and on PEM fuel cell performance. The selected materials that used for GDL and gas flow channel surface modifications will be discussed briefly in this chapter.

3.1 Coating Materials and Processes

3.1.1 Silica Particles and Silica Polydimethylsiloxane (PDMS) Composite

Hydrophobic and hydrophilic treatment of fuel cell components represents a research area of great interest due to the water accumulation and flooding issues at the cathode side of PEM fuel cell. Till now, the GDL and gas flow field channels are commonly treated by polytetrafluoroethylene (PTFE) [37, 67, 68] and its derivatives such as polyvinylidene fluoride and fluorinated ethylene propylene [3], to impart the hydrophobic properties on the GDL and gas flow field channel surface and alumosilicate fibers [36], to impart the hydrophilic properties on the GDL surface. Nafion and the loading of these materials is generally high, around 20 wt. % or more on GDL. On the other hand, the high cost and health concerns are big issues with PTFE [69, 70]. Further, the alumosilicate fibers coating is complex. In this work, silica particles and polydimethylsiloxane (PDMS) are chosen as a coating material, since they are cheap, non-toxic, ease of use and robust nature [71].

Silica and PDMS are mixed together, and applied to coat the gas flow field channels and the GDL, where silica particles are used to adjust the surface roughness and PDMS covered the top surface of silica particles and offered its low surface energy property in such composite coating. This combination of surface roughness and low surface energy material provide a hydrophobic coating on the surface of gas flow field channel and GDL [71, 72]. Further, adding silica nano particles to PDMS polymer reinforce the polymer matrix structure and increase the bonding force between the silica particles/ PDMS composite and the coated surface as PDMS polymer alone has low mechanical strength [73, 74]. This reinforcement is attributed particle-polymer interactions, through which hydrogen bonding between particles significantly increases the resistance to the applied force [75].

The size and loading of silica particles and the loading of PDMS polymer in silica/PDMS composite has a critical role in determining the surface properties. Wang *et al.*[71] concluded that the silica/PDMS optimum properties on the coated surface were obtained when the 3 wt. % of 262 nm silica particles mixed with 1 wt. % of PDMS in Tetrahydrofuran (THF), and referred to as silica particle/PDMS composite. This composite gives the highest contact angle (θ) and the lowest sliding angle (α) compared with other loadings ratios.

3.1.2 Graphite Coating

3.1.2.1 Coating Materials

A resin impregnated graphite sheets grade FU 4369 HT purchased from Fuel Cell Store Inc. Colorado, US, is cut into square samples (2 ×2 cm) and channels (150 × 4 × 4 mm, channel size). All these samples are cleaned by ultrasound to wash off the absorbed carbon powders. Tetramethyl orthosilicate (TEOS), ammonium hydroxide aqueous solution (28.0-30.0 wt. %) and Polytetrafluoroethylene (PTFE, 60 wt. % in H_2O) are obtained from Sigma-Aldrich Ltd., ON, Canada. The Sylgard 184 kit (PDMS), containing PDMS oligomers and curing agents, are purchased from Dow Corning, MI, USA. The solvents, ethanol, methanol, iso-propanol and tetrahydrofuran (THF) are of analytical grade and used as received from Sigma-Aldrich Ltd., ON, Canada.

3.1.2.2 Graphite Coating Processes

Surface energy of the graphite channels are modified accordingly using different materials. Four graphite channels are prepared with different surface wettability in addition to the raw (non-coated) graphite channel which is slightly hydrophobic as shown in Table 3.1.

Table 3:1: Chemical mixture composition and coating procedure parameters showing mixing time (t_{mix}) and sintering time (t_{sin}) for various surface wettabilities sol-gel spread coating

No.	Surface Wettability	Solvent	Contents	t_{mix} (min)	T(°C)	t_{sin}(min)
1	Superhydrophobic	Tetrahydrofuran(THF)	262 nm silica particles/PDMS[1] composite	10	180	5
2	Hydrophobic	Dispersed in water	PTFE[2] emulsion	10	180	30
3	Slightly Hydrophobic	--	Non-coated graphite	--	--	--
4	Superhydrophilic	Ethanol	262 nm Silica particles suspension	10	180	30
5	Combined surface wettability channel	--	Bottom surface is superhydrophobic and side walls are slightly hydrophobic	--	--	--

[1]PDMS: Polydimethylsiloxane, [2]Polytetrafluroethylene

Table 3.1 lists the parameters of chemical mixtures compositions used to coat the channel surfaces' uniformly as shown in Figure 3.1a. All channels are pre-cleaned with ethanol. The precursor solutions are prepared by dispersing the contents in the solvent and stirring vigorously. After adding specified amount of solvent, the resultant solution is kept stirring for time t_{mix} (mixing time) to produce the required solution. The prepared solution is spread on the surface of the channel using a brush. After coating, the samples are heat treated at T °C for time t_{sin} (sintering time). One more channel is modified with a superhydrophobic surface for the bottom surface only using the same mixtures, and the channel sides' surfaces are non-coated (combined surface wettability channel) as shown in Figure 3.1b.

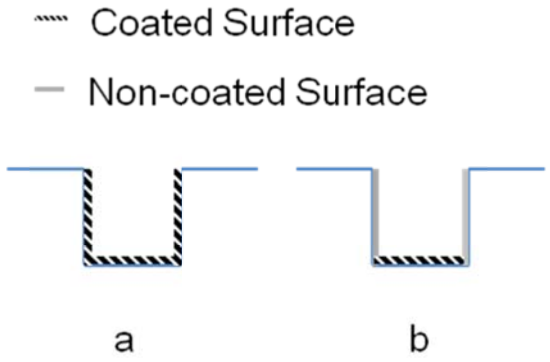

Figure 3.1: Cross section of the coated channels a) uniformly coated channel, and b) combined surface wettability channel.

3.1.3 Gas Diffusion Layer (GDL) Coating

GDL type A with micro-porous layer (MPL) is provided by SolviCore GmbH & Co. KG Fuel Cell Technology, Hanau-Wolfgang, Germany. Raw (Non-coated) GDL (SpectraCarb 2050-A, 10 ×10 cm, from Fuel Cell Store Inc., Colorado, and USA) is coated with different materials to obtain GDLs with different surface wettability; silica particles coated (superhydrophilic), PDMS coated (Hydrophobic) and silica particles /PDMS coated GDL (superhydrophobic). In addition to these modified samples, a one side hydrophobic GDL is produced by coating one side of the GDL with PTFE to study the effect of wettability gradient through GDL plane.

3.1.3.1 Coating Materials

Raw GDL (SpectraCarb 2050-A, 10 ×10 cm, from Fuel Cell Store, USA) is cut into 2cm × 2cm and circular with 2.3 cm diameter. All samples are cleaned by ultrasound to wash off the absorbed carbon powders. Tetramethyl orthosilicate (TEOS), ammonium hydroxide aqueous solution (28.0 - 30.0 wt. %) are purchased from Sigma-Aldrich Canada Ltd. The Sylgard 184 kit, containing PDMS oligomers and curing agents, are purchased from Dow Corning, MI, USA. The solvents, ethanol, methanol, iso-propanol, and tetrahydrofuran (THF) are of analytical grade and used as received from Sigma-Aldrich Canada Ltd. Water used is prepared from Milli-Q Ultrapure Water system (Millipore Co., USA). Polytetrafluoroethylene (PTFE, 60 wt. % in H_2O) is purchased from Sigma-Aldrich Ltd., ON, Canada.

3.1.3.2 Silica Particles Coating on GDL

Prepared silica particles are re-dispersed in ethanol, resulting in 1 wt. % suspension by ultrasound. 0.04 mL of this mixture is evenly spread on the both surfaces of raw GDL. After evaporating the solvent, the sample is cured for 5 min at 180 °C. The GDL samples are treated following the same processes and to be tested for the PEM fuel cell performance.

3.1.3.3 PDMS Coating on GDL

Dow Corning Sylgard 184 kit (2.0 g oligomers and 0.2 g curing agent) is dissolved in 17.8 g of THF, resulting in a 10 wt. % solution. 0.04 mL of the solution is spread on the raw GDL surfaces and cured for 5 min at 180 °C. The loading of PDMS on GDL is about 3.5wt. %.

3.1.3.4 Silica Particles/PDMS Composite Coating on GDL

Prepared silica particles (3wt %) and PDMS (1wt %) are dispersed in THF by ultrasound. 0.08 ml of this mixture is evenly spread on the surfaces of raw GDL .When the solvent evaporated, the sample is cured for 5 min at 180 °C. The GDL samples are treated following the same procedures and used in the fuel cell assembly instead of the conventional GDL in order to investigate the overall PEM fuel cell performance for each case.

3.1.3.5 Polytetrafluoroethylene (PTFE) Coating on GDL

Raw GDL is coated using PTFE 60 wt. % solution. The solution is diluted to 15 wt. % by De-Ionized water (DI water), and then coated on one side of the raw carbon paper by brushing the PTFE emulsion using a painting brush. The sample is dried in oven for 2 hours at 180 °C. Finally, the coated GDL is washed by methanol and water to remove the surfactants brought in by emulsion. The weight of GDL is measured before and after coating. This process is repeated at least 2 times till the PTFE wt. % is controlled to 15±2 wt. % of the GDL sample.

3.2 Characterization

3.2.1 Silica Particles Characterization

Prepared silica particles are dispersed in ethanol. Their sizes and size distribution (polydispersity index, PDI) are measured by Dynamic Light Scattering (DLS) (Zetasizer, Malvern Inc., UK) at 20 ºC. The PDI is calculated from the following equation:

$$\ln(G1) = a + bt + ct^2 + dt^3 \qquad \textbf{3.1}$$

where G1 is a correlation function, the second order cumulant b is converted to a size using the dispersant viscosity and instrumental constants. The coefficient of the squared term c, when scaled as 2c/b2, is defined as PDI, which can range from 0 (monodisperse) to 1 (polydisperse). The Z-average diameter and PDI of the prepared silica particles is 262 ± 5 nm and 0.02, respectively [76]. In this thesis the silica particle size referred as 262 silica particles.

3.2.2 Surface Topography and Roughness Measurements

The surface topography of non-coated and coated graphite and GDL samples are observed by field-emission Scanning Electron Microscope (SEM) (LEO 1530, Germany), and the surface roughness is measured on an ST400 Optical Profiler (NANOVEA, Affiliate of Micro Photonics Inc., USA).

3.2.3 Surface Wettability Measurements

The surface wettability of the graphite and GDL and graphite samples are determined by measuring the static contact angle (θ) and sliding angle (α) as follows.

3.2.3.1 Static Contact Angle Measurements

The static contact angle (θ) of water is measured for the coated and non-coated graphite and GDL surfaces using Kruss DSA contact angle apparatus, on which a PTFE needle (inner diameter 0.25 mm; outer diameter 0.52 mm) was equipped. To measure the static contact angle, 10 µl droplets are introduced at 5 different locations on each sample, and the standard deviation are estimated.

The contact angle is measured under room temperature and atmospheric pressure; however since the PEM fuel cell is running at 80 °C. The effect of temperature is investigated by measuring the static contact angle under different temperature for different coatings. The sample is replaced in a heat chamber equipped with a small transparent window to allow imaging the water droplet on the tested sample.

3.2.3.2 Sliding Angle Measurements

In this work the sliding angle for the water droplet is measured for the coated graphite and GDL surfaces using Kruss DSA contact angle apparatus with a tiltable plane using 10 μl of water droplet. The plane is attached to the angle measuring wheel which is scaled from 0° to 360°. The water droplet is placed into the coated channel or on the GDL surface, while both the channel and the GDL are in a horizontal orientation, and then by rotating the wheel the graphite/GDL surface is tilted. The tilting angle is recorded manually when the droplet starts to move on the channel surface. At least 5 readings are recorded for each surface and the error is determined from these readings. The Kruss DSA visualization systems are used to monitor the droplet when it starts to slide. The measurement is measured at room temperature and atmospheric pressure.

3.3 Experimental Techniques for Two-Phase Flow Visualization

3.3.1 Experimental Set-up

The experimental set-up used in this study is designed for co-current flow of air and DI water in 4 × 4× 150 mm horizontal graphite channel. Figure 3.2 shows the schematic of the graphite channel. The cross-section of channel is determined in macro-channel region which proposed by Mehendal *et al.* [77] with hydraulic diameters 1-6 mm, and to ease the channel coating, the channel cross-section area is determined 4 × 4 mm cross section.

Graphite channel is stacked between two Plexiglass plates for flow visualization purpose and sealed with silicon gasket by ten ¼" SAE 8 bolts as demonstrated in Figure 3.3.

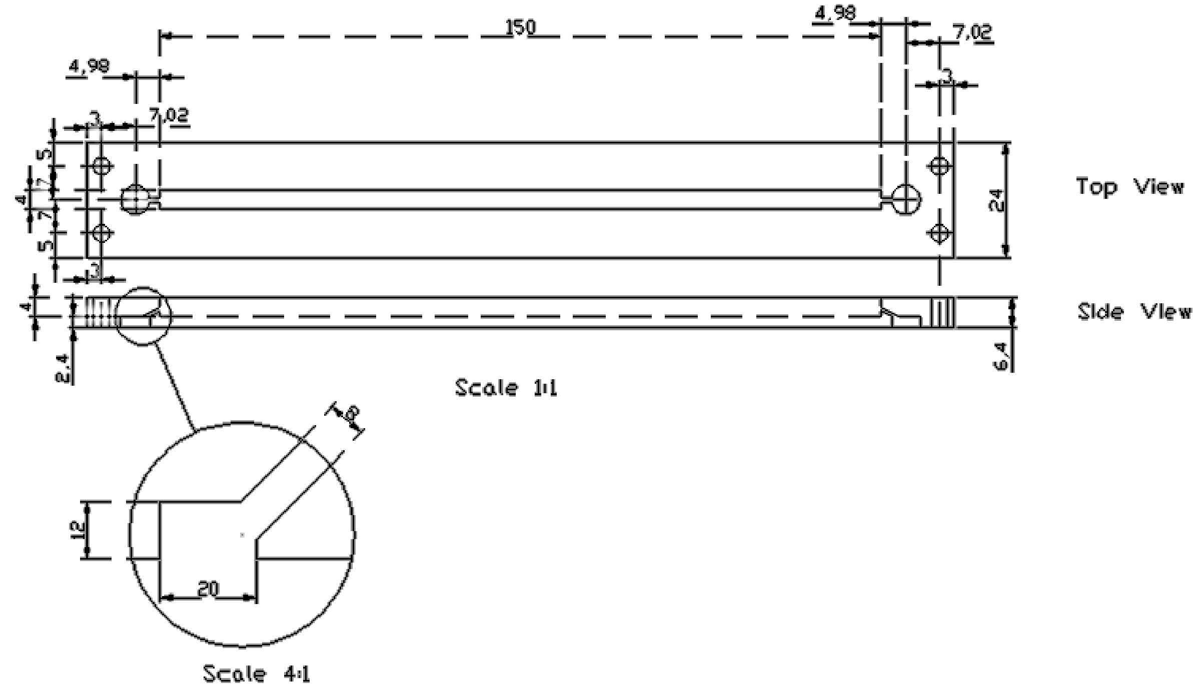

Figure 3.2: Side and top views of the designed graphite channel showing the side and top views.

Figure 3.3: Graphite channel stacked between two plexiglass s plates.

The stacked graphite channel is horizontally positioned and connected to the experimental apparatus to visualize the two-phase flow as illustrated in Figure 3.4.

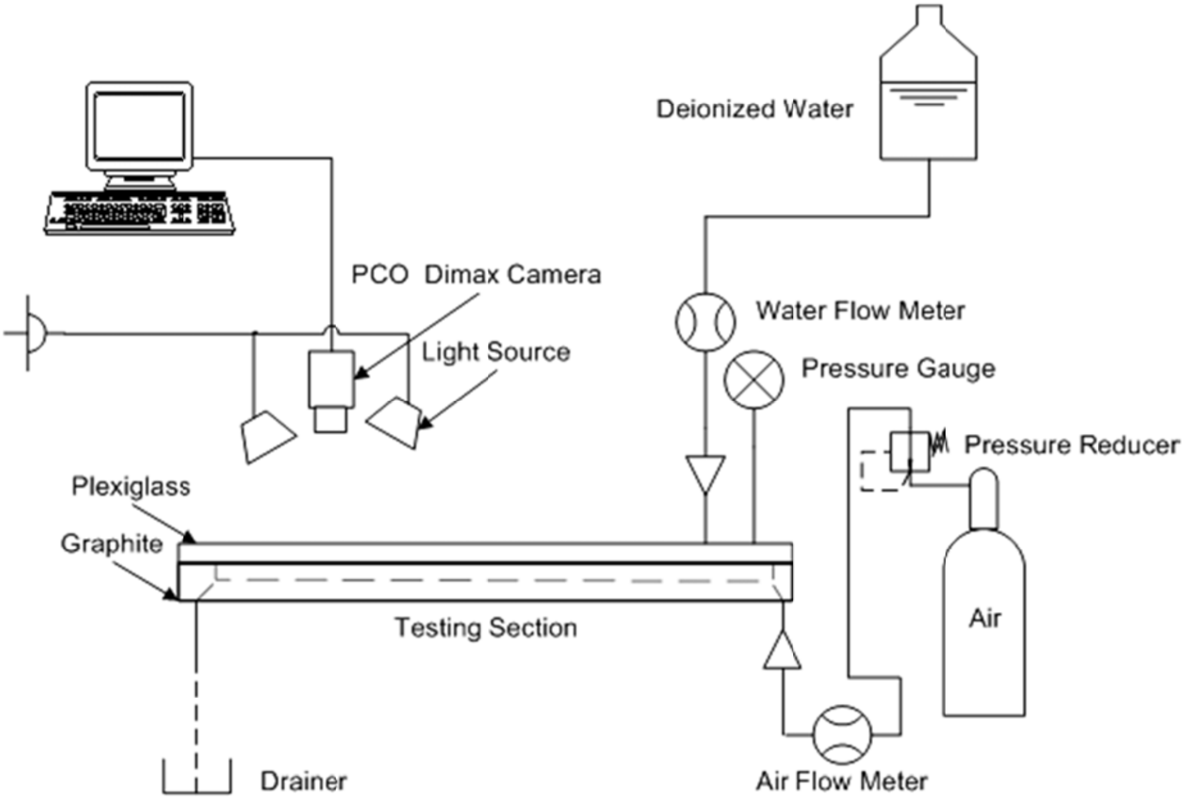

Figure 3.4: Two-phase flow graphite channel testing experimental set-up.

Air is introduced into the channel through the channel inlet, and water is introduced into the channel from the top surface of the channel, positioned 30 mm away from the channel inlet. Pressure transducer is installed with 10 mm distance from the channel inlet. The working fluids are air and DI water for gas and liquid phase, respectively. The flow rates of the air and DI water are controlled and adjusted to the prescribed value using the flow meters.

Pressure meter (VWR International LLC, Model No. 61161-390) is accurate to ± 1% plus 1 digit for pressure readings and operating in the range of (0 – 2) kPa, used to measure the pressure at the channel inlet and the pressure at the channel exit is kept at atmospheric pressure as shown in Figure 3.4. The two-phase flow is confirmed with visualization of the flow patterns, which monitored and recorded by high speed 12 bit complementary metal–oxide–semiconductor (CMOS) camera system (PCO.DIMAX, 12bit, image rates of 1279 frames per second (fps) at full resolution of 2016 x 2016 pixel). CMOS technology has a unique advantage over other available visualization techniques which is high noise immunity. Two halogen lights sources (600W) are used to illuminate the testing section, while an electric fan is installed on each light to reduce the temperature of the light source.

3.3.2 Leak Test

Before start testing, Leak test is carried out for the stack and for the set-up pipe lines. The stacked channel is pressurized with nitrogen at the air inlet after blocking the channel exit and the DI water inlet. If the gage pressure shows a constant/no change in pressure value during in a period of 5 min, this indicates that the stack is sealed properly. However, in case the set-up shows a decrease in pressure value, then the stack is leaking. Thus, the stack needs to be placed in a DI water container to dedicate the leaking spots, which has to be fixed accordingly. This process is repeated until the accumulated pressure inside the stack stops decreasing to ensure proper experiment procedure.

The leak of air and DI water lines in the set-up are tested separately following the same procedures, after that the set-up will be tested with the installed stack. After pressurizing the whole set-up with the stack, in case the pressure inside the set-up is decreased, this indicates that the system is leaking. To determine the leaking spots, a soap solution is sprayed on the pipe lines and connections. Thus, bubbles formation can be used as an indication for the occurrence of the leakage at certain locations. The leakage has to be fixed, and this process is repeated until the leak stops.

3.3.3 Test Loop

Experiments are carried out in the test loop that is schematically shown in Figure 3.4;

1- DI water pumped from a water tank, passed through a flow meter with a valve to control the flow rate, (Omega-High Accuracy Shielded Rota meters FL-113) with ± 2% of reading accuracy and ± 1% of reading repeatability, to the channel test section and to the drainer,

2- Once the desired flow rate of DI water is reached, Air is supplied through a laboratory compressed air system passing through a flow meter with a valve to control the flow rate (Cole-Parmer 150mm Correlated Flow meter with High-Resolution Valves R-032 series) ± 2% of full scale reading and ± 0.25% of reading repeatability , to channel testing section, and to the drainer,

3- The flow images of the two-phase flow are recorded after the flow reaches a steady state. The required time for the flow to reach steady state is about 15-20 min. The steady state of the flow can be distinguished from the stability of the flow meters readings and the repeatability of the flow pattern which captured through the CMOS camera on the computer screen, and

4- The frequency of imaging is 2000 fps depends on the air flow rate. All the images are recorded and analyzed accordingly.

3.3.4 Pressure Measurements

The stacked channel has three graphite surfaces and the fourth one is plexiglass s as shown in Figure 3.3. The plexiglass s is slightly hydrophilic which might affect the pressure readings. Thus, the channel is covered with hydrophobic GDL to eliminate the plexiglass effect on the pressure measurements and to simulate the channel in the real PEM fuel cell as shown in Figure 3.5.

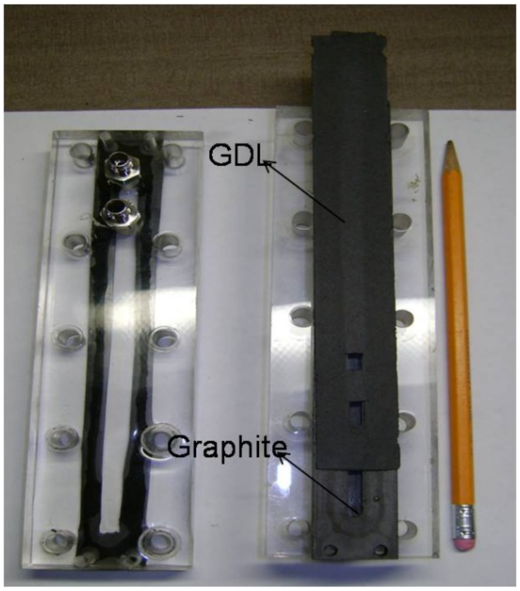

Figure 3.5: Graphite channel covered with hydrophobic GDL for pressure measurements.

After installing the stacked channel covered with hydrophobic GDL in the apparatus, the test loop is carried out again and the pressure is measured at the channel inlet and the pressure at the outlet is atmospheric. The pressure readings are recorded and averaged by Jumbo-size digits RS-232 at 1 Hz for 5 minutes after reaching the steady state.

3.3.5 Experimental Conditions

All experimental investigations are carried out at room temperature and atmospheric pressure as shown in Table 3.2.

Table 3:2: Experimental conditions for two-phase flow investigation in graphite channels with different surface wettability

Parameter	Type	Condition
Gas	Dry Air	Laminar flow regime ($Re_{air} \leq 2000$)
Liquid	DI Water	Laminar flow regime ($Re_{water} \leq 2000$)
Temperature	--	Room temperature
Pressure	--	Atmospheric pressure

The flow velocities of air and water supply correspond to laminar flow regime. Hence, the current experimental purpose is to simulate the typical PEM fuel cell operating conditions, yielding the anode and cathode gas flow in the laminar flow regime. Furthermore, the typical laminar flow is more than sufficient to provide the mass transport of the reactant gases into the electrode for fuel cell electrochemical reactions under the most extreme fuel cell operating conditions (high current densities) [78, 79]. The experimental work is conducted with a laminar-laminar air-DI water two-phase flow in horizontal mini channels at atmospheric pressure and room temperature.

The two-phase flows in different channels are characterized by the air volumetric flux, J_G (m/s) and the DI water volumetric flux J_L (m/s), defined respectively as;

$$J_G = \frac{Q_G}{A_i} \tag{3.2}$$

$$J_L = \frac{Q_L}{A_i} \tag{3.3}$$

Where Q_G and Q_L (m^3/s) are the volumetric flow rate of air and DI water which controlled by flow meters; A_i is the cross-sectional area of the channel at the air and DI water inlet.

All experiments are conducted when the channel is in a horizontal orientation to ensure that the water is in touch with the graphite channel. Hence, in vertical orientation water tends/prefers to travel through the plexiglass s surface since it is more hydrophilic than graphite surface. This may negatively impact the measurement uncertainties which can lead to a considerable misleading in the two-phase flow results inside the graphite channel. Experiments are conducted by keeping the volumetric flux of water at J_L = 0.02, 0.12, 0.65, and 1.03 m/s, respectively, while varying the volumetric flux of air J_G = 3.63, 4.84, 6.19, 7.37, and 8.68 m/s.

Five different channels with different surface wettability for each are employed in this test as shown in Table 3.3.

Table 3:3: Surface conditions of the tested channels

No.	Surface Condition	Coating Material
1	Superhydrophobic	Silica/PDMS
2	Hydrophobic	PTFE
3	Slightly hydrophobic	Non-coated
4	Superhydrophilic	Silica
5	Combined surface wettability	Silica/PDMS –(bottom surface) raw graphite (side walls)

3.4 Gas Diffusion Layer's Porometric Characteristic Measurements

In this work a non-destructive Method of Standard Porosimetry (MSP) is used to investigate the Porometric characteristics of GDL including; average porosity, integral pore volume, pore size distribution, capillary pressure and wetting angle distribution. This method is used to study all GDL samples used in this work in order to understand the effects of different coating materials on GDL porometric characteristics.

3.4.1 Principle of Operation of Method of Standard Porosimetry (MSP)

The automated standard porosimetry machine is a manipulation robot that realizes method of standard porosimetry in automated mode. It is provided by Porotech Ltd., Toronto, ON, Canada. Standard Porosimeter 3.1 consists of the following parts as shown in Figure 3.6:

1. Drying station,

   Drying station realizes several functions: tight contact of standard and the sample (hereinafter kit) with required compression, heating of the kit to the fixed temperature, vacuum drying, equalizing the kit to reach the capillary equilibrium.

2. Weighing station,

   Weighing station includes digital analytical balance with accuracy ±0, 0001 g. It gives opportunity to work with comparatively low weight samples.

3. Manipulation robot,

   Manipulation robot intends to move holder kits with standards and samples from drying station to weighing station.

4. Vacuum system,

   Vacuum system consists of mechanical lubricated rotary vane vacuum pump Dekker.

5. Protective box,

   Made from Aluminum and It serves to protect analytical balance and precision mechanisms from the environment (particularly dust).

6. Block of electronic control and personal computer (PC),

   Block of electronic controls the functions of Porosimeter utilising programmable logic controller (PLC) with drivers for electric step motors.

7. Holder kit,

   Holder kit intends to carry standards and samples. It consists of three Aluminium alloy cups that can be put one to another.

8. Peripheral equipment for standards and samples pre-treatment,

   This equipment is used to dry the sample and saturate it with the working liquid.

9. Molding cups, standards, test sample and working liquid like octane or DI water.

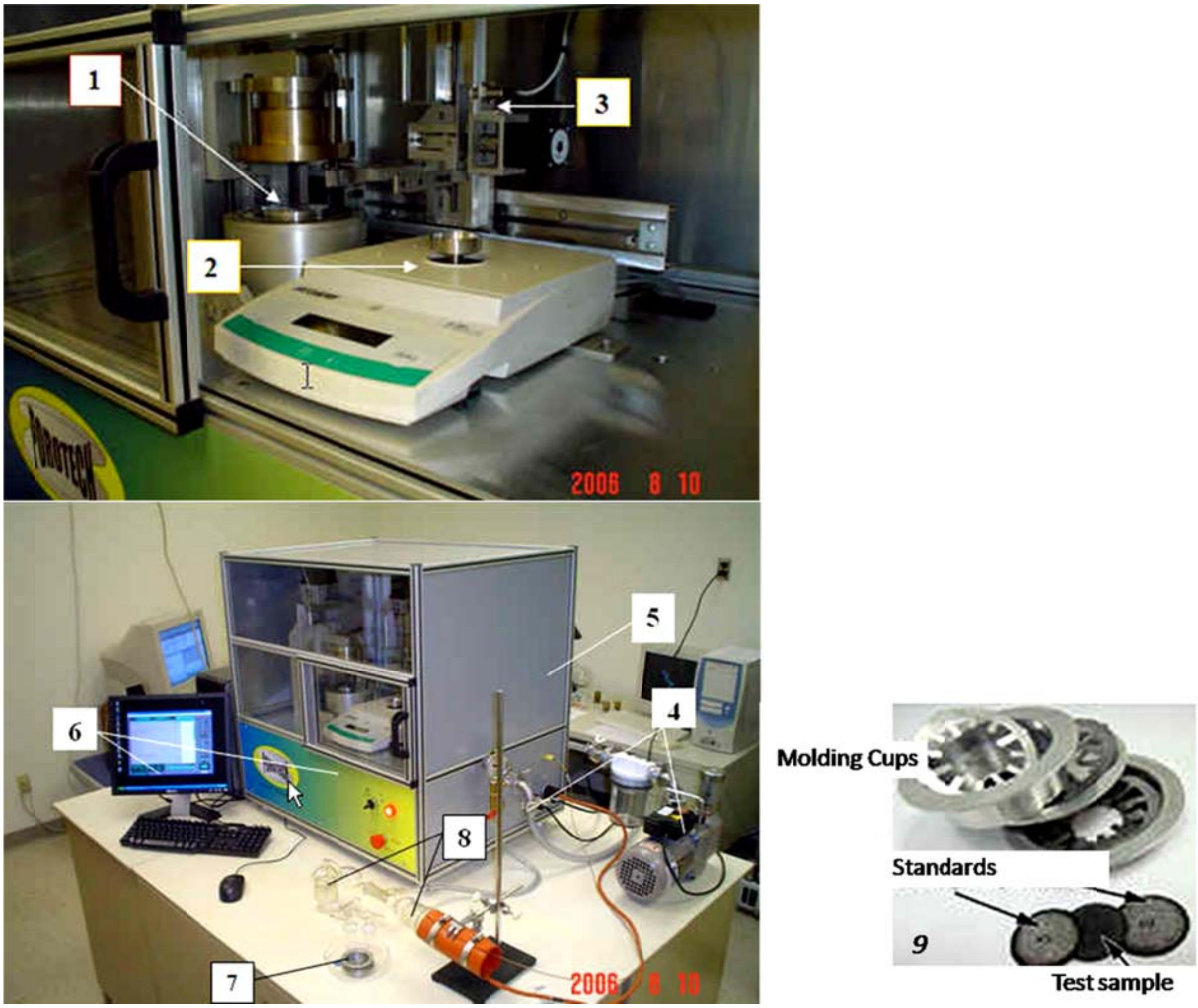

Figure 3.6: Main parts of the Standard Porosimeter 3.1.

This method uses the principle of capillary equilibrium, where two partially saturated porous materials in contact and possess the same capillary pressure.

1- The standards, which are porous disks with known capillary pressure curves. These disks are designed to be completely wetting to most fluids, such as water and organics.

2- The samples are prepared by evacuating the standards and the sample to be tested, then flooding them with the wetting fluid (i.e. octane), to ensure no air is trapped in the porous materials when liquid enters.

3- The samples are then stacked so they are in capillary contact and exposed to air as shown in Figure 3.7a.

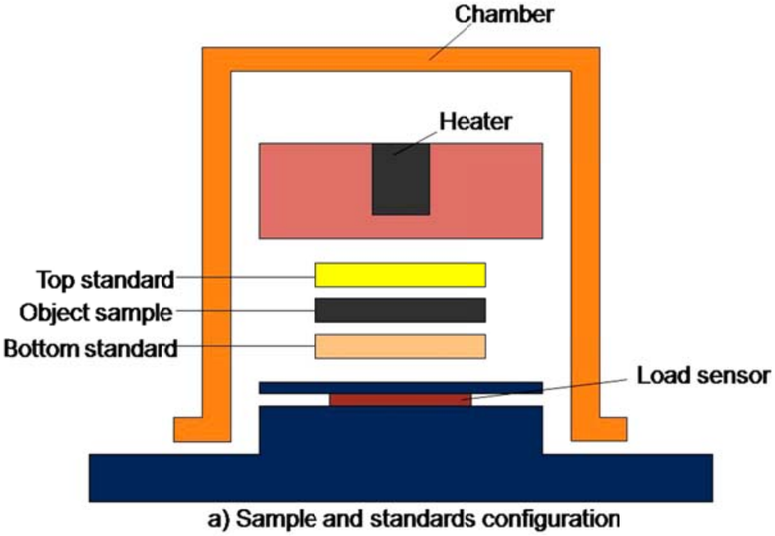

a) Sample and standards configuration

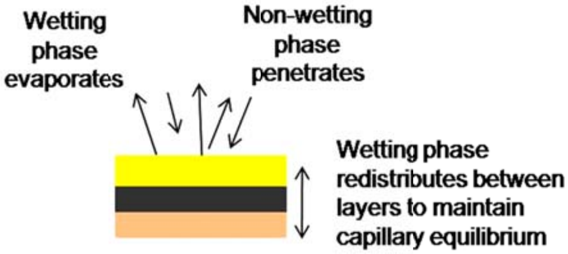

b) Capillary equilibrium process

Figure 3.7 : Method of standard porosimetry (MSP) configuration showing; a) sample and standards layout, and b) fluid movement occurring during capillary equilibrium.

4- The wetting fluid evaporates from both the sample and the standards, and the non-wetting fluid which is air will penetrate into the sample and the standards, resulting in decreasing the saturation with the wetting phase as shown in Figure 3.7b.

5- The capillary pressure curve will be generated from this process is shown in Figure 3.8. Periodically, the sample and standards are separated and weighed to determine their individual saturations (step1). Since the standards have known capillary pressure curves, their capillary pressure can be found from knowledge of their saturation (step2). Since the sample and standards are assumed to be in capillary equilibrium, this value also corresponds to the capillary pressure of the sample being tested, so the sample saturation can be related to the standards capillary pressure (Step 3) [80].

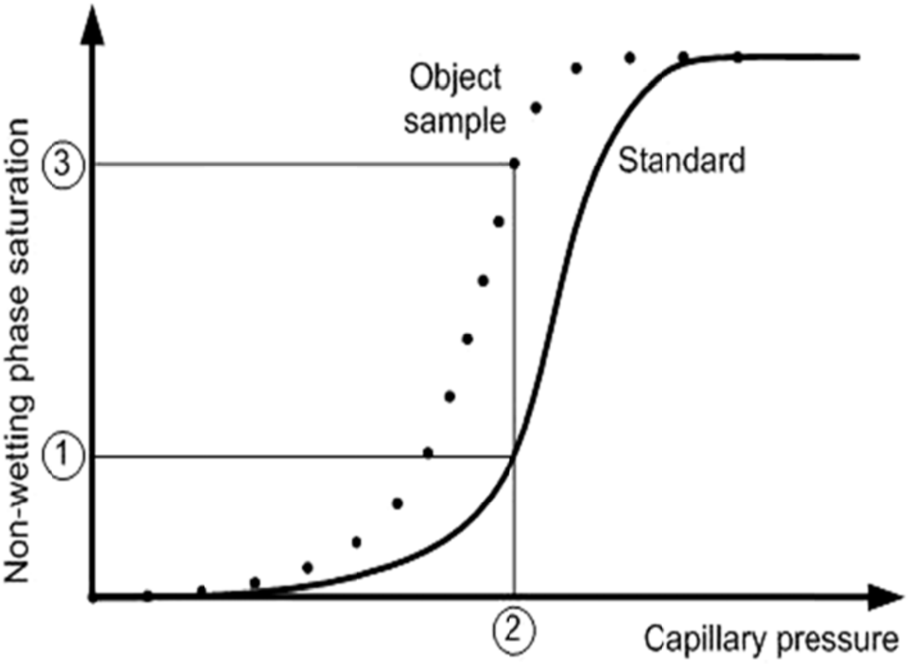

Figure 3.8: Schematic explaining the capillary pressure measurements for the sample with respect to the standard

6- The relationship between capillary pressure and the radius of pore can be represented by the Young-Laplace equation;

$$p_c = \frac{2\gamma \cos\theta}{r} \qquad \mathbf{3.4}$$

where γ is interfacial tension of the liquid, θ is the static contact angle of the liquid droplet on the solid, and r is the maximum radius of pore filled with liquid. As equilibrium of capillary pressure between the standard body (sb) and the object body (ob) is reached during MSP testing, it is possible to rearrange as;

$$p_{c,sb} = p_{c,ob} = \frac{2\gamma \cos\theta_{sb}}{r_{sb}} = \frac{2\gamma \cos\theta_{ob}}{r_{ob}} \qquad \mathbf{3.5}$$

$$\frac{r_{ob}}{r_{sb}} = \frac{\cos\theta_{ob}}{\cos\theta_{sb}} \qquad \mathbf{3.6}$$

when a highly wettable liquid such as octane is used as a wetting liquid, the contact angle for the both bodies can be regarded as 0°. Consequently, r_{sb} at the given saturation and capillary pressure is determined in terms of r_{ob}.

3.4.2 Experimental Procedures

1- GDL sample is cut using the cutting mould with diameter (D = 23 mm),

2- The cut GDL sample and the standards are dried and saturated under vacuum with octane or DI water,

3- The cut GDL sample and the standards are placed in the aluminum cups, the sample should be held between the standards,

4- The stack is transferred into the chamber where the standards and the sample are brought into contact. The stack undergoes drying and preset conditions of vacuum, temperature and compression as shown in Figure3.9,

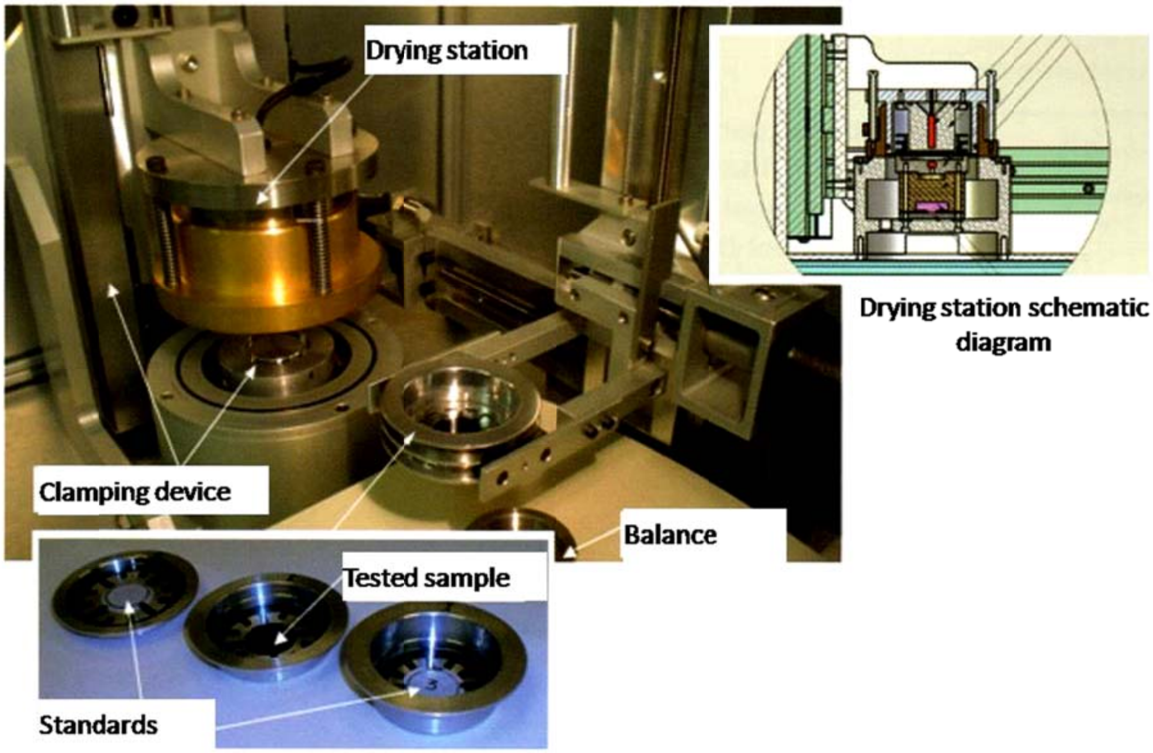

Figure 3.9: Shows the sample and the standards stack during running the automatic measurements.

5- After a period of time the stack is removed from the chamber, disassembled and weighted individually,
6- The process continues until the stack is completely dry,
7- All the data is gathered automatically using the machine software,

3.4.3 Experimental Conditions

All the GDL samples are dried at 160 °C for one hour to guarantee that there is no any water vapor inside the GDL pores. Two liquids are used for saturating the GDL samples; octane and DI water. The saturation with octane is carried out under vacuum for 30 min. Hence, octane is very wettable ($\theta \approx 0°$) liquid to most of the surfaces, it is used to investigate the hydrophobic and hydrophilic GDL pores since it penetrates both pores easily. Meanwhile, DI water is neither highly wettable to most of surfaces like octane nor highly non-wettable like mercury, so it is used to investigate the hydrophilic pores only. The GDL sample is boiled for 30 min in DI water and kept for 24 hours saturation time in a hot DI water bath at 70 °C, to obtain porometric results for the water in identical environments to the real operational PEM fuel cell.

The saturation temperature and the chamber are maintained at 70 °C. Meanwhile, for octane the temperature is reduced to 50 °C to obtain more representative data, since octane is more volatile than water. The compression pressure of the stack is kept at 200 kPa to guarantee that GDL sample is in touch with the standards during capillary pressure equilibrium. Excessive compression force may change both overall porosity, and pores size distribution. Thus, it may cause permanent deformation of pore structure of GDL. On the contrary, insufficient compression may yield to limited contact between the samples, which hinders in equilibrium of capillary pressure.

Five different GDL samples with different wettability are investigated in these experiments as illustrated in Table 3.4.

Table 3:4: Tested GDL samples using MSP

No.	Surface Condition	Coating Material
1	Superhydrophobic (Sandwich wettability GDL)	262 nm Silica particles/PDMS
2	Superhydrophilic	262 nm Silica particles
3	Slightly hydrophobic	Non-coated sample
4	Type A with MPL	Both sides PTFE coated
5	One side hydrophobic GDL	One side PTFE coated GDL

3.5 Water Removal Rate Measurements & Droplets Imaging

Water removal and visualization tests are applied on the one side hydrophobic, raw, and commercial GDL samples to measure the amount of transferred DI water through GDL sample in a certain period of time. Further, the droplets emerged on the GDL surface are imaged using high speed camera. This test is designed to investigate the effect of wettability gradient of one side hydrophobic GDL.

3.5.1 Experimental Set-up

Water removal rate is measured using a 20 ml syringe barrel. A 13 mm GDL token is capped to the barrel at the finger flange side and the DI water is supplied into the barrel from the needle hub side. The barrel is fixed in vertical orientation as shown in Figure 3.10. Once the water starts to discharge from the GDL out of the barrel under the gravity effect, the time and the amount of water are recorded by timer and digital balance with ± 0.001g accuracy (Denver Instrument TP 303), respectively.

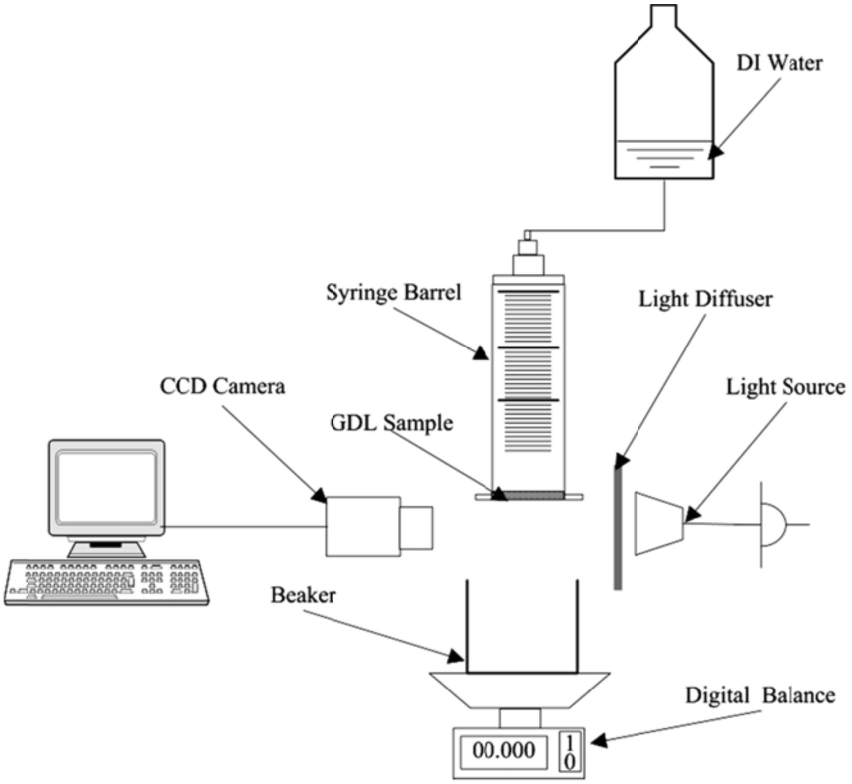

Figure 3.10: Experimental set-up for measuring water removal rate and droplets visualization on GDL surface.

A high performance cooled digital 12 bit charge-coupled device (CCD) camera system (SensiCam) is used to image the droplets on the GDL surface at 30 fps. All images are captured and saved automatically using the CAMWARE software.

3.5.2 Experimental Procedures

1- GDL token is cut and glued on the syringe barrel; each tested sample is glued on different syringe,

2- Leakage is tested for each glued sample; the barrel is filled with water and left in vertical orientation to ensure a proper sealing for the glued area,

3- The GDL sample is saturated with water for 24 hours in warm water about 40 °C, 4- The GDL sample with barrel is installed in the experimental set-up in a vertical orientation as shown in Figure 3.10,

5- Water supplied to the barrel, and as soon as the water come out from the GDL the time and weight of the discharged water are recorded,

6- Sensicam camera is used to image the droplets drain out of GDL at 30 fps.

3.5.3 Experimental Conditions

The test for each GDL sample is conducted under the room temperature and atmospheric pressure. This test is designed to study the effect of wettability gradient through GDL plane. Thus, four different GDL samples are tested; one side hydrophobic GDL where the coated side facing water in the syringe barrel; and one side hydrophobic GDL where the non-coated side facing water inside the syringe barrel, commercial, and raw GDL. Each sample is tested for five times. The average and the standard deviation are estimated for each sample.

3.6 PEM Fuel Cell Design and Experimental Testing

The PEM fuel cell is designed, fabricated, and assembled in-house; the design and fabrication steps of the flow fields plates, end plates, and current collectors are discussed in this section. The assembly procedures, sealing materials, and leak testing procedures are also explained. Further, the operating principles of testing apparatuses such as a Fuel Cell Automated Test Station (FCATS-S800) and other experimental set-ups are also discussed in this section. Finally, the experimental procedures and conditions as well as the accuracy of the experimental data are discussed in the following subsections.

3.6.1 PEM Fuel Cell Components and Design

In this work two different PEM fuel cells are used. The first one is with 100 cm^2 active area and with single serpentine flow field plate and the second one is with 40 cm^2 active area with three parallel serpentine flow field plate. The size of the cell is selected based on the availability of the other PEM fuel cell components, which are provided by SolviCore GmbH & Co. KG. Three components are designed in house; flow field plate, collector plate, and end plate. The rest of the components are provided by other companies and they are ready for assembly.

3.6.1.1 Flow Field Plates

A resin impregnated graphite sheets, (grade FU 4369 HT) bought from Schunk Group, Heuchelheim, Germany, is used for fabricating the flow field plates. Being brittle, graphite requires extra care during handling. Initially, the channels and the peripheral area are machined to be at the same level on plate surface to guarantee better conductivity of the channel rips with the GDL as shown in Figure 3.11.

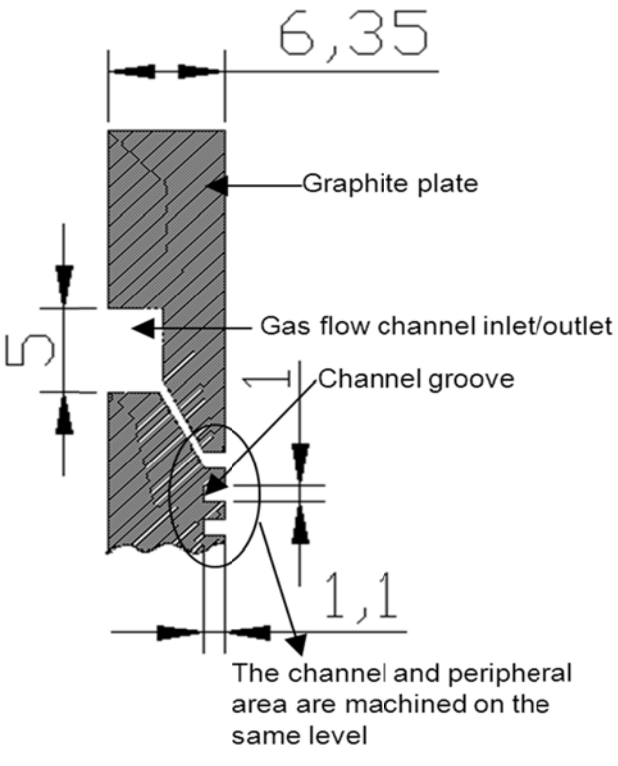

Figure 3.11: Sectional side view of flow field plate with 100 cm^2 active area, (all dimension in mm and length are not to scale).

3.6.1.2 Channels Layout Design

The appropriate design of flow channels built on the flow field plates is critical for water management. Serpentine flow channel layout [5] is the most widely used one, often regarded as “industry standard”, since under the same operating and design conditions, PEM fuel cells with serpentine flow channels tend to have the best performance and durability.

In this work, serpentine flow field layout is designed for all cells, in which reactants enter from one side and leave through the other, traversing in a single pass over the active area as shown in Figure 3.12. In this layout, due to the existence of only one path for the reactants flow, any liquid water accumulating in the channels is quickly pushed out of the cell.

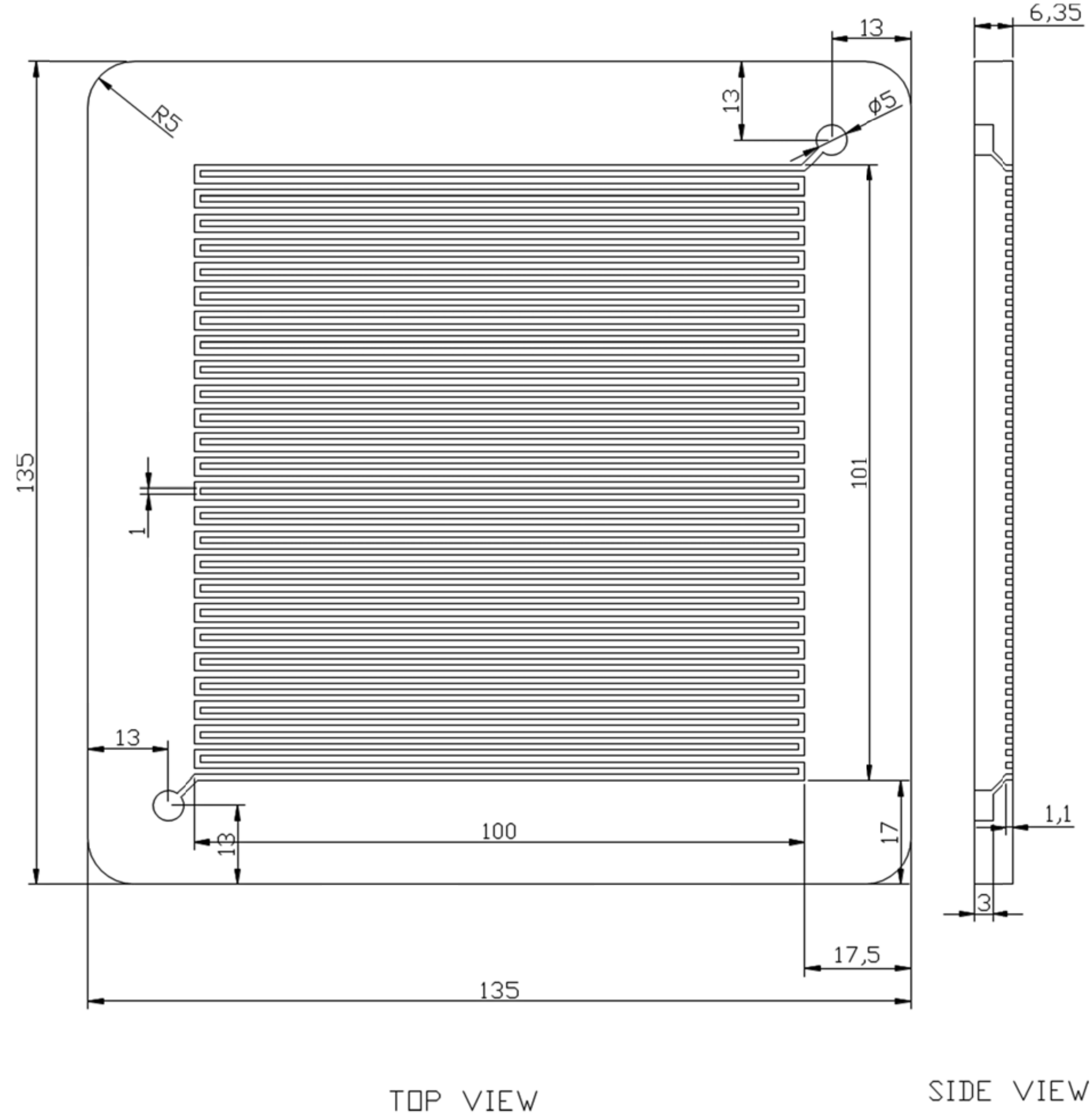

Figure 3.12: Top and side views for single serpentine flow field plate design for 100 cm^2 active area PEM fuel cell (all dimension are in mm and the lengths are not to scale).

As shown in Figure 3.12 the flow field plate has almost a 100 cm^2 active area. It is used for anode and cathode gas flow field plates for PEM fuel cell. In addition to the 100 cm^2 cell, A

40 cm^2 active area flow field plate is used in this work. The flow field plate size is chosen based on the supplied MEAs sizes from SolviCore GmbH & Co. KG. According to the active area the channel width for the 40 cm^2 should be 0.8 mm. However, to ease the machining process and to avoid inlet pressure build up. The channel width is chosen to be 1 mm with three parallel serpentine flow field layout as shown in Figure 3.13. This design allows more air/fuel utilization over the cell active area.

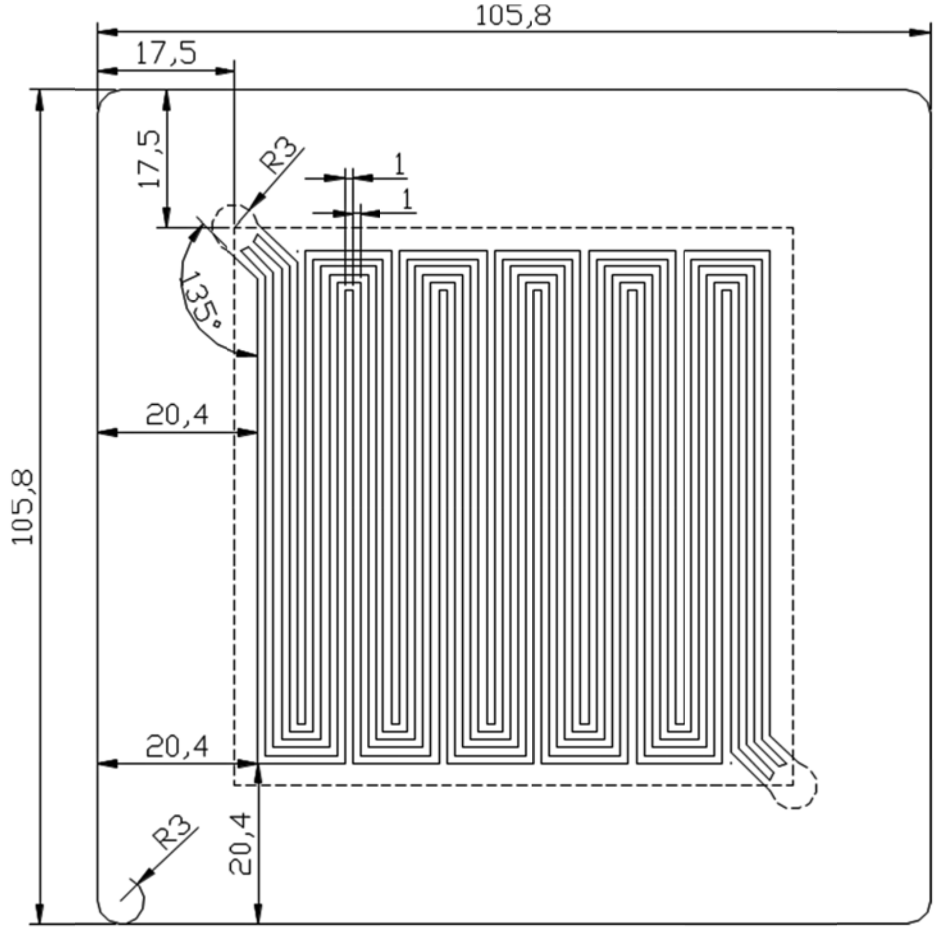

Figure 3.13: Top view for three parallel serpentine flow field plate design for 40 cm^2 active area PEM fuel cell (all dimension are in mm and the lengths are not to scale).

3.6.1.3 Channel Cross-Section Shape

A flow channel cross section shape is determined by the manufacturability of this shape and the cost of manufacturing. Many choices of the cross-sectional shape are proposed, from the simple rectangular or square shape, to triangular, trapezoidal, semi-circular shape or any other shape that might be applied on the flow channel. However, since graphite material is the typical material used in the conventional flow field plate. This will narrow our choices for the cross-section shape. Graphite material is hard and brittle. Hence, it is difficult to machine the flow channels on it. Consequently, fabricating the flow channels on the flow field plate is time-consuming and expensive process, which contributes significantly to the total cost of a PEM fuel cell stack [81].

To reduce the cost, the channel fabrication process should be simplified. The geometrical shape of the cross section has to be categorized as simple geometry. Rectangle and square cross section shapes have traditionally been chosen for the flow channel design and fabrication because of their geometrical simplicity.

3.6.1.4 Channel Dimensions Calculations

The channel dimension can be categorized into small dimensions and large dimensions. Small dimensions are: channel width (a), channel depth (b), and the land area width (channel rip, w). The length of the channel (l) is the only large dimension as illustrated in Figure 3.14.

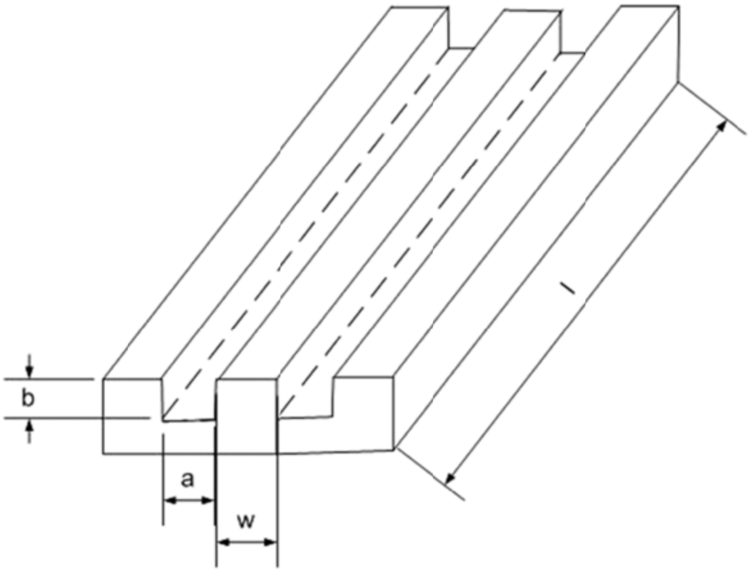

Figure 3.14: Schematic diagram shows the channel dimensions in details [79].

The channel width, *a*, is often chosen based on the need for distributing the reactant gas over the active cell surface. The distance between the channels, *w*, is decided based on the need for current collection. The channel depth, *b*, is determined based on the consideration of the flow regime. Therefore, the design or selection of the flow channel dimensions should consider the cell operating conditions as well as the cell structural parameters. Typically, the GDL and flow field plate materials are highly conductive electronically, while the reactant gas transport is relatively slower, hence the ratio of the land width to the channel width is typically in the range of 0.8–1.0 [79]. The typical values for Reynolds numbers in PEM fuel cells are within the laminar flow regime [82].

In the flow channels, Reynolds number is conventionally defined as:

$$R_{eD_h} = \frac{inerial\ force}{Viscosity} = \frac{\rho U D_h}{\mu} \qquad \textbf{3.7}$$

where ρ is the density, μ is the viscosity of the gas flowing in the flow channels, and U is the flow stream velocity in the channels, which can be determined as:

$$U = \frac{\dot{m}}{\rho A_C} \tag{3.8}$$

where $\dot{m}$ is the mass flow rate in the flow channels, and D_h is the hydrulic diamter of the flow channle. The D_h for rectangular channels is calculated as:

$$D_h = \frac{4A_C}{\mathrm{W_P}} \tag{3.9}$$

where A_C is the cross section area of flow channel, which is determined as:

$$A_C = a \times b \tag{3.10}$$

where a and b are the width and hight of the flow channel, respectively.
Wetted perimeter is defend as:

$$W_P = 2 \times (a + b) \tag{3.11}$$

For laminar flow regime inside the channel, the maximum permissible Reynolds number should be maintained at 2000. However, the minimum Reynolds number to provide sufficient flow convection should be in the order of 100 or higher. In this case, the hydrodynamic entrance length is defined as:

$$l_e \approx 0.06 \times R_e \tag{3.12}$$

Since the cross-sectional area of the flow channel is typically small compared to the length, the entrance region can be neglected. The pressure drop of flow along the flow channel length is expressed as:

$$\Delta p = f \frac{l}{D_h} \frac{\rho U^2}{2} \tag{3.13}$$

where f is the friction factor for fully developed laminar flow in squared flow channel is given as [83]

$$f = \frac{56.91}{R_{eD_h}} \tag{3.14}$$

Assuming that $a = b$ (width = height) and substituting the equation (3.12) into equation (3.11). The pressure drop can be expressed again as:

$$\Delta p = 28.455\left(\frac{\mu\dot{m}}{\rho}\right)\left(\frac{l}{b^4}\right) \tag{3.15}$$

Thus, the flow channel length can be determined for square cross-sectional as:

$$l = \frac{\rho \Delta p b^4}{28.455\mu\dot{m}} \tag{3.16}$$

3.6.1.5 Membrane Electrode Assembly (MEA)

MEA consists of membrane layer, two catalyst layers, and two GDLs layer. Two types of MEAs are available; three layers MEA, and five layers MEA. The recent one comes with the GDL all assembled as one piece. However, three layers MEA do not have GDL layers.

The membrane fabricated by SolviCore GmbH & Co. KG, offered with two sizes to our labs; a 100 cm^2 and 40 cm^2. It consists from three layers; a membrane layer and two catalyst layers. The three layer assembly required external gas diffusion layers to be placed on the MEA during the cell assembly process. The MEA used in the present experiment consisted of a Nafion 112 membrane, a total platinum loading of 0.5 $mg.cm^{-2}$ for both cathode and anode.

Two types of gas diffusion layers are used; first one supplied by SolviCore GmbH & Co. KG and the second one is provided by SpectraCarb. The SolviCore GmbH & Co. KG GDLs are manufactured using carbon fiber which is bound using a carbon based adhesive and is coated with a 30 wt. % PTFE to make the porous layer hydrophobic. The surface in contact with the catalyst layer is coated with a micro-porous layer (MPL). The MPL consists of carbon black powder and approximately 10 wt. % PTFE, which acts as a hydrophobic agent and to bind the powder. This GDL is mostly used for the anode side in PEM fuel cell in the current study.

SpectraCarb GDL is made from carbon fiber with 0% PTFE content. In this work SpectraCarb GDL is used in cathode side of PEM fuel cell. The GDL wettability is modified using different materials as mentioned earlier in section 3.1.2.

3.6.1.6 Electrical Collector and End Plate Design

End plate is made from aluminum alloy, 6061. This material satisfies the functional requirements of the end plate, high strength (125 MPa tensile strength) and high thermal conductivity (180 W/m-K) [84]. Aluminum 6061 is easy to machine and it is relatively cheap compared to other aluminum alloys. The aluminum end plates used for the PEM fuel cells are designed and fabricated in two different sizes; one for the 100 and 40 cm^2 active areas PEM fuel cells as shown in Figure 3.15.

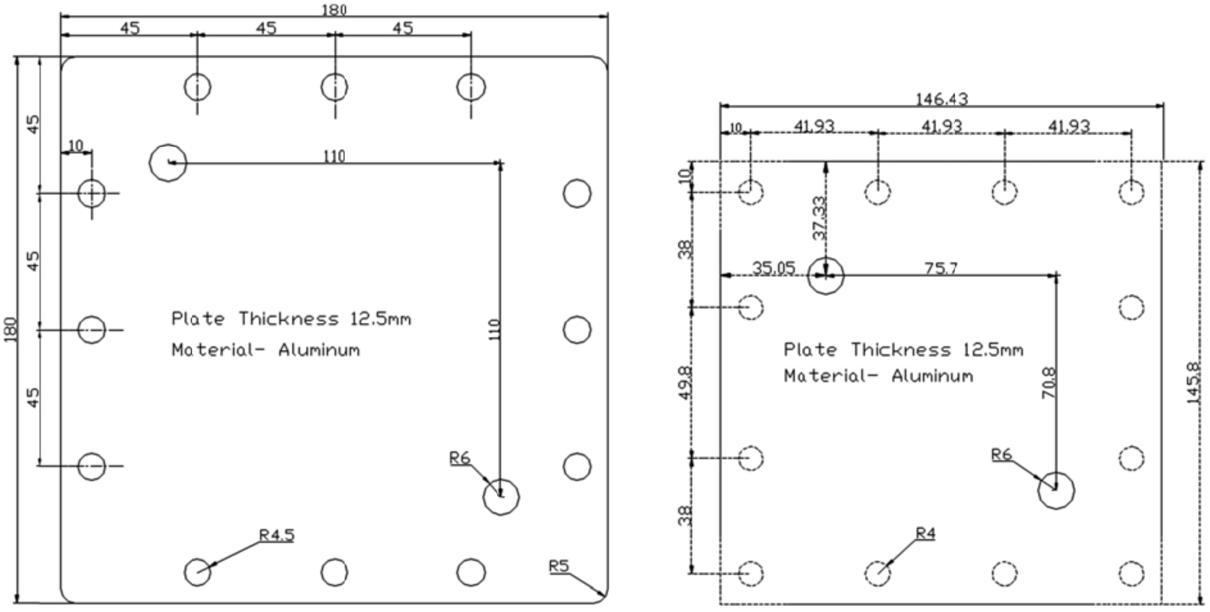

END PLATE FOR 100cm^2

END PLATE FOR 40cm^2

Figure 3.15: Top view of end plate design for 100 cm^2 and 40 cm^2 active area PEM fuel cells (all dimension are in mm and the lengths are not to scale).

Current collectors are fabricated from copper material. The copper composition used for these current collectors is C15720, which contains Cu > 99%. This copper grade had a low electrical resistivity of 1.94 W/m·K at 20 °C, high thermal conductivity of 353 W/m·K at 20 °C and it is relatively cheap compared with other materials. The design of the current collector allows connecting the electrical load box through a drilled hole on the extended terminal of the plate as shown in Figure 3.16.

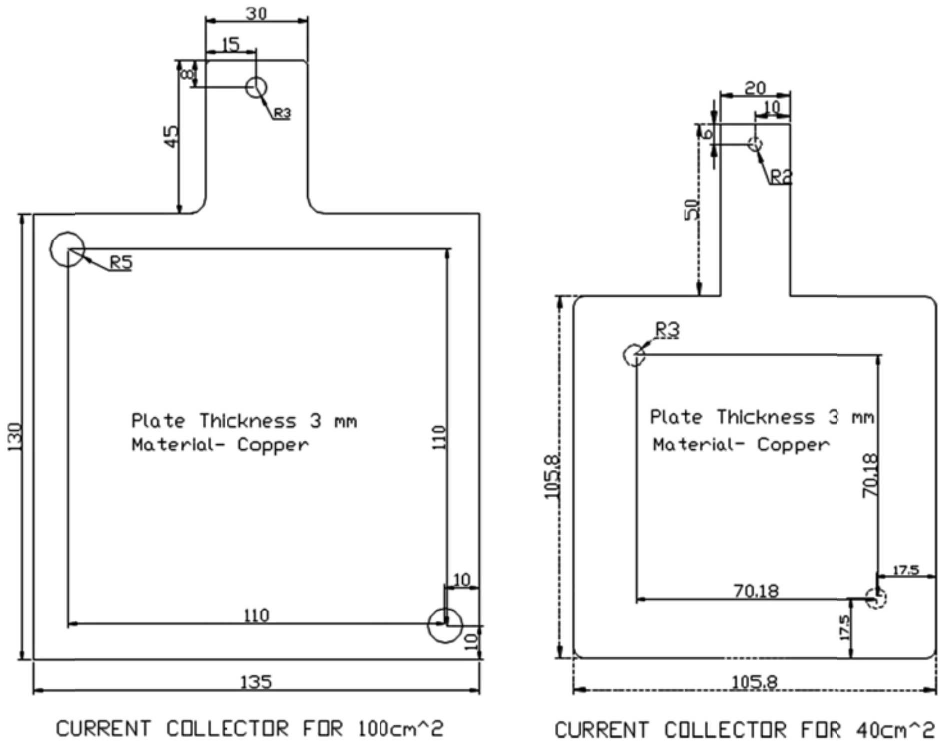

Figure 3.16: Top view of collector plate design for 100 cm^2 and 40 cm^2 active area PEM fuel cells (all dimension are in mm and the lengths are not to scale).

3.6.2 Assembly Procedures

After designing and fabricating all the aforementioned PEM fuel cell components, a single fuel cell components include; two flow field plates, two current collectors, two end plates, two silicon gasket plates, three layer MEA, two GDL layers, and the cut gaskets for the anode and cathode side as shown in Figure 3.17, are assembled together to form a single PEM fuel cell.

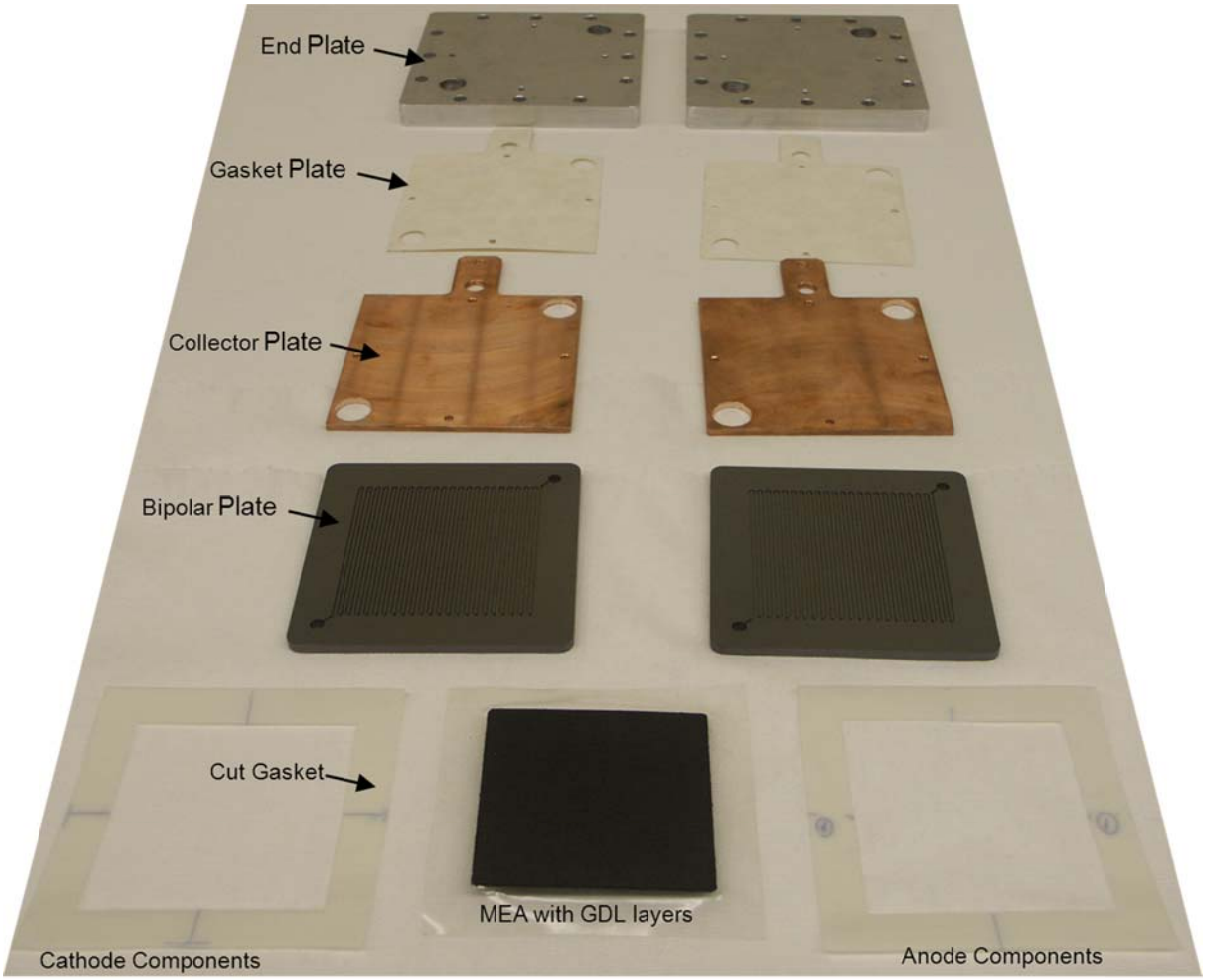

Figure 3.17: A sample of cathode and anode components for single PEM fuel cell.

The flow field plate and current collector is isolated from the aluminum end plate by silicon gasket plate. Each anode and cathode flow field plate has one inlet and one outlet. In this work, the inlets and outlets are on the same side, which is known as a co-flow arrangement. The fuel cell assembly is sealed using twelve ¼″ SAE 12 bolts. Each bolt is subjected to uniform pressure controlled by an adjustable torque wrench, which are 65 in-lbs. for each bolt. The cut silicon gasket is the primary sealing material for preventing leakage from the fuel cell and it is placed between the MEA and the bipolar plate as shown in Figure 3.18.

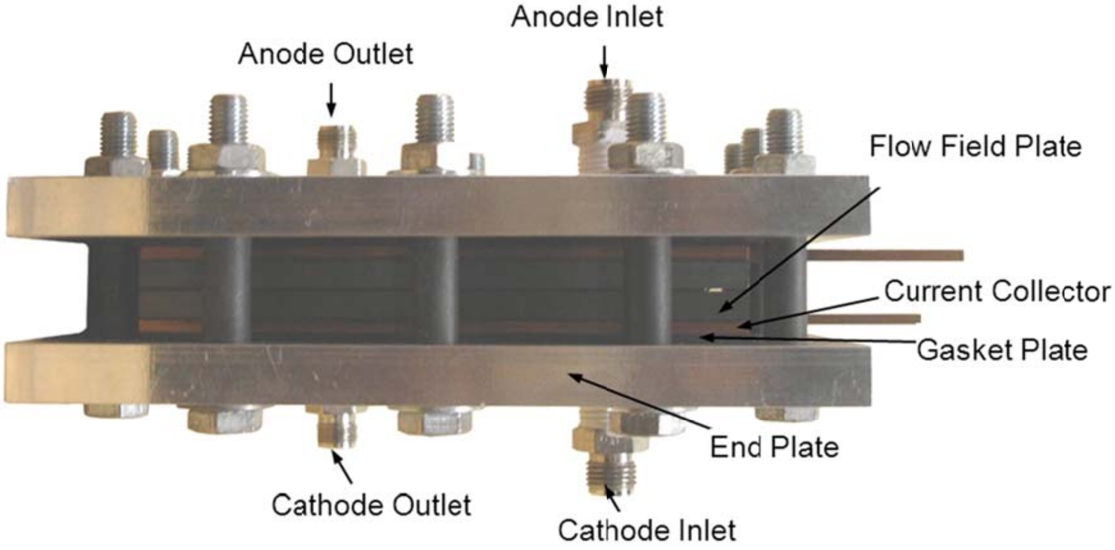

Figure 3.18: Single assembled PEM fuel cell showing the cell components and the co-flow arrangement.

3.6.3 Testing Station

The PEM fuel cell experimental investigations are carried out using the Fuel Cell Automated Test Station (FCATS-S800), manufactured by Hydrogenics Inc. The FCATS is designed to control fuel cell operating conditions. It can control the fuel cell's temperature, pressure, relative humidity, and the stoichiometry of the reactant gases on both the anode and cathode sides [85]. The FCATS is also equipped with a computer-based control and data acquisition system, and its operating parameters are controlled and monitored through special software developed for this purpose. The reactants are supplied from compressed cylinder tanks of hydrogen, air, and pure nitrogen as shown in Figure 3.19.

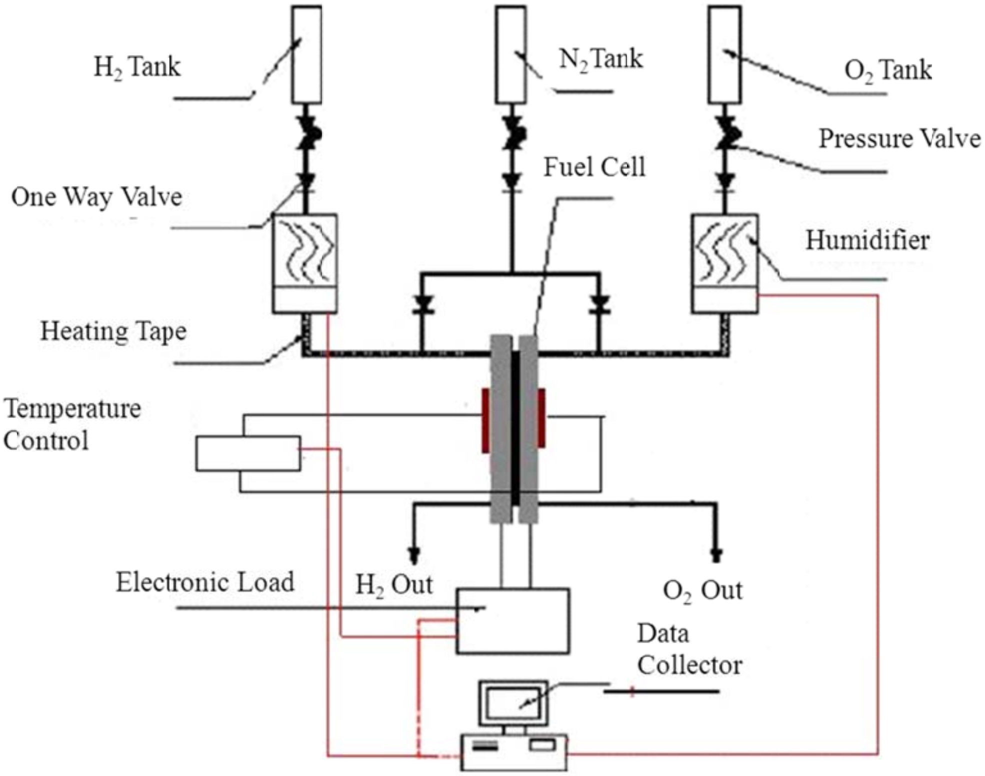

Figure 3.19: Simplified schematic diagram of Fuel Cell Automated Testing Systems (FCATS –S800).

Pure nitrogen is used in this experiment to purge the reactant gases from the fuel cell and to clean up from the products of the electrochemical reaction (water) during the startup and shutdown processes. DI water is supplied to generate steam for humidifying the reactants. Regulating the dew point temperature with respect to inlet temperatures controls the degree of humidification of the reactant gases. The load box is an integral part of the FCATS for measuring voltage and current.

3.6.4 Leak Test

Before testing the assembled cell, it is important to make sure that the cell is assembled correctly, and the cell is ready for testing in safe manner, since the hydrogen gas is used at the anode side. This is done through the leakage test. A variety of techniques can be used to identify the location and source of leaks in PEM fuel cell. The cell should be tested for crossover of reactants from anode to cathode and vice versa, and peripheral leakage. Compressed N_2 gas is used for the leak test. Hence, N_2 is an inert gas, it will not react with the cell components, and it will not react with the supplied reactant H_2 and O_2 when the cell test is started. The leakage test set-up is simply shown in Figure 3.20.

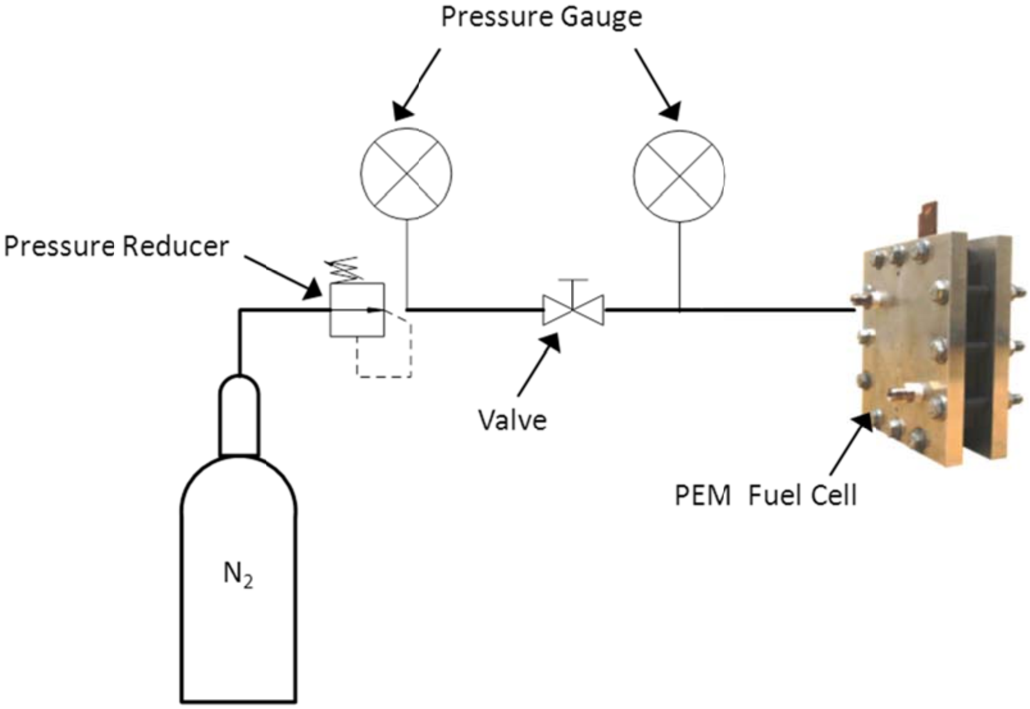

Figure 3.20: Leakage test set-up for PEM fuel cell.

Initially, the nitrogen supply is connected to the inlet of anode side and outlet is plugged. On the cathode side, the inlet is plugged and a tube is connected to the outlet and dipped in a glass container of water. 25 kPa pressure is applied which is within the safe limit of pressurizing single side of the MEA. Any bubbles in the water indicated crossover (pin-holes in membrane) of the reactants.

For the peripheral leakage test, the anode/cathode side is connected to the nitrogen supply at the inlet, while the outlet of is plugged. When the pressure reaches to 25 KPa on the pressure gauges, the valve is shut off simultaneously. The pressure gauge, between the valve and the cell, sensed any pressure loss due to leakage. If the pressure is retained for about 15 min, the cell is safe to operate with a hydrogen and air stream. This process is performed for both; anode and cathode sides.

3.6.5 Performance Test

If the assembled cell is not leaking, this means that the cell is ready and safe for performance test. In this work, the performance test is designed to allow for the inspection of cell potential and power density response, as a function of current density, to changes in cell cathode's GDL and gas flow channel wettability. Each test cell is run at varying current load settings, increases incrementally, while cell potential is monitored and recorded, along with several other controlled parameters.

Figure 3.19 shows the schematic diagram for PEM fuel cell connected with FCATS-S800 testing station. The anode and cathode inlets of the fuel cell are connected to the hydrogen and air supplies of the FCATS-S800, respectively. The oxidant and fuel gauges are heated and humidified before they enter into the channels where they are consumed in the electrochemical reaction. The cell is heated to 65 °C using heating pads. In the meantime the cell is operated at 25mA/cm^2. This will generate heat and allow the cell to reach operational temperature sooner. The warm-up process typically takes between 60 to 90 minutes. The current and voltage of a PEM fuel cell can be measured by the load box through two power cables. The fuel cell requires about 90 minutes reaching the steady state condition, defined as reaching all the required operating conditions as illustrated in Table 3.5. Then, each reading is recorded after at least 200 sec of the current loading change.

Table 3:5: List of PEM fuel cell operating conditions

Description	Value
Cell temperature (°C)	65
Anode Inlet temperature (°C)	65
Cathode Inlet temperature (°C)	65
Anode and Cathode back pressure (gauge) (kPag)	25
Anode stoichiometry (St.)	1.2
Cathode stoichiometry (St.)	2
Relative humidity at the cathode and anode inlet (%)	100

When the cell is operated for the first time, the cell has to be activated. The activation process requires running the cell after it reaches the steady state between 0.5-0.7 volts at least for 20 hours. This process is repeated at least three times. In this work the time between the successive activation tests, is at least 24 hours. The activation process increases catalyst utilization by activating many ‘‘dead’’ regions in the catalyst layer. Further, Nafion is mixed into the catalyst layer to make it proton conducting in three dimensions, many of the catalyst sites are not available for reaction due to various possible reasons: (1) reactants may not reach the catalyst sites because they are blocked, (2) Nafion near these catalyst sites might not be easily hydrated, or (3) an ionic or electronic continuity might not established to these sites. Activation process might open some of these dead areas and become active. The activation process is stopped when the cell performance becomes steady and do not increase compared with the last activation test [86].

3.6.6 Uncertainty Analysis

As mentioned earlier, the FCATS testing station consists of different control and measuring instruments. These instruments and controls are calibrated by the manufacturer according to procedure and standards established by the National Institute of Standards and Technology (NIST). The accuracy of the measuring and control instruments are provided by the manufacturer, as illustrated in Table 3.6.

Table 3:6: Summary of parameter uncertainty for FCATS-S800 [85]

Parameter		Units	Range	Uncertainty
Flow	Anode	nmlpm	0 - 4000	± 1%
	Cathode	nmlpm	0 - 16000	± 1%
Temperature		˚C	-20 - 100	± 2 ˚C
Pressure		kPa	0 - 350	± 3 kPa
Load	Voltage (high range)	V	10 - 50	± 0.25%
	Voltage (low range)		0 - 10	± 0.5%
	Current (high range)	A	5 - 400	± 0.25%
	Current (low range)		0 - 5	± 0.5%

The fuel cell performance measurement involves many processes that occur inside the cell at the same time. These processes include electro chemical reaction, mass and heat transfer, electron and proton conduction, and water management. Thus, the cell performance has no standard error analysis can be fully applied to all of these processes at the same time. However, the performance curves can be easily compared with confidence. Further, the error analysis of the performance test measurements is obtained by repeating each test at least 5 times, especially for the 40 cm^2 PEM fuel cell. And then the coefficient of variation (CV) is estimated. Thus, every test is repeated five times (N) for each operating condition and each voltage reading (x) is recorded by the data acquisition system at frequency of 1 Hz (1 reading per second) over sufficient period of time. The average and standard deviation can be computed as follows:

$$\bar{X} = \frac{1}{N}\sum_{i=1}^{N} x_i \qquad \textbf{3.17}$$

Therefore, the standard deviation (σ) of the set of reading for the voltage at certain current density can be estimated as follows:

$$\sigma = \sqrt{\frac{1}{N-1}\sum_{i=1}^{N}(x-\bar{X})^2} \qquad \textbf{3.18}$$

Since the average value represents the average of the measured voltages at the same current at different tests, the standard deviation of the average value can be estimated as follows [87]:

$$\sigma_E = \frac{\sigma}{\sqrt{N}} \qquad \textbf{3.19}$$

The coefficient of variation (CV) is defined as the ratio of the standard deviation to the mean $\bar{X}$:

$$CV = \frac{\sigma_E}{\bar{X}} \qquad \textbf{3.20}$$

Chapter 4

Results and Discussion

The discussion of the results is divided into three main parts; in the first part, silica/ Polydimethylsiloxane (PDMS), Polytetrafluoroethylene (PTFE), silica coated graphite and the none-coated graphite surface characterization results, and the impact of each type of surface coating on the surface wettability characteristics, two-phase flow in macro-channel, and PEM fuel cell performance is discussed. In the second part, silica/PDMS and silica, which are considered as new coating materials for GDL is studied along the non-coated GDL and the commercial GDL (30 wt. % PTFE coated GDL with MPL). Further, their effect on the GDL characteristics, wettability, and on the PEM fuel cell performance is also investigated. Meanwhile, the third part covers the effect wettability gradient through GDL plane by coating one side of GDL with 15 wt. % PTFE on GDL characteristics, water removal capabilities and PEM fuel cell performance are investigated along with the commercial and non-coated GDL. Since the second part of this chapter discusses the effect of the new coating materials along with the commonly used materials. Further, the third part discusses the effect of a new technique of coating using a conventional coating material (PTFE) which results in a wettability gradient through the GDL plane.

4.1 The Effect of Gas Flow Channels Composite Coatings on the Surface Characteristics, Wettability, Two-Phase Flow, and PEM Fuel Cell Performance

4.1.1 Effect of Composite Coatings on Surface Wettability

Coating graphite surface with different materials results in different surface wettability associated with different characteristics. The surface wettability is determined by measuring the static contact angle (θ) as illustrated in Table 4.1. However, when the water droplet is moving on the solid surface, the higher static contact angle does not always correlate with smaller sliding angle (α). This would mean that hydrophobicity has to be distinguished from the true repellency of water droplets. Surface roughness also contributes to static contact angle as the drop is pinned on the surface. The contact line of a droplet can have a complex shape according to the surface geometry, resulting in increasing repellency of water droplet on solid surface, hence roughness increases the amount of air entrapped between the water droplet and the solid surface [88-90]. Furthermore, as the amount of air increases beneath the droplet, water repellency increases; hence the static contact angle between water and air phases is 180°. This reduces the droplet sliding angle as illustrated in Table 4.1.

Table 4:1: Measured static contact angle (θ) and sliding angle (α) for different channels with different surface wettability.

No.	Coating Material	Surface Condition	θ	α
1	262 nm Silica particles/PDMS	Superhydrophobic	155±2°	19±1°
2	PTFE	Hydrophobic	145±5°	67±1°
3	Non-coated	Slightly hydrophobic	95±2°	>90°
4	72 nm Silica Particles	Superhydrophilic	15±2°	Thin Film

It is clear that superhydrophobic surface have the best water repellency among the other three tested surfaces. This because of the low surface energy of the silica/PDMS coating and its complex structure formed on the graphite surface. On the other hand, the hydrophobic surface has less water repellency due to high sliding angle ($\alpha = 67 \pm 1°$). In spite of low surface energy ($\theta = 145 \pm 5°$) of PTFE coating surface structure of the PTFE coating resulted in higher sliding angle.

It is seen that the slightly hydrophobic surface has higher surface energy ($\theta = 95 \pm 2°$). The droplets and slugs can form on the slightly hydrophobic surface; however, they hardly slide on the surface ($\alpha \geq 90°$). This relates to the structure of the non-coated graphite unlike the superhydrophobic surface. On the other hand, the droplets do not form on the superhydrophilic surface. This can be due to the nature of silica particles, which is typically hydrophilic (high surface energy) with the surface hydroxyl groups [91]. Unlike the rest of the surface conditions, the water completely spreads on the superhydrophilic surface forming a thin film instead of droplets or slugs.

The effect of temperature on the contact angle of the superhydrophobic coating is not significant as shown in Figure 4.1. This might be attributed to the stability of the structure of composite coating on the graphite surface. Further, in the running fuel cell the effect of temperature on the contact angle of the superhydrophobic surface might be negligible, thus all contact angle measurements in this study are considered at room temperature.

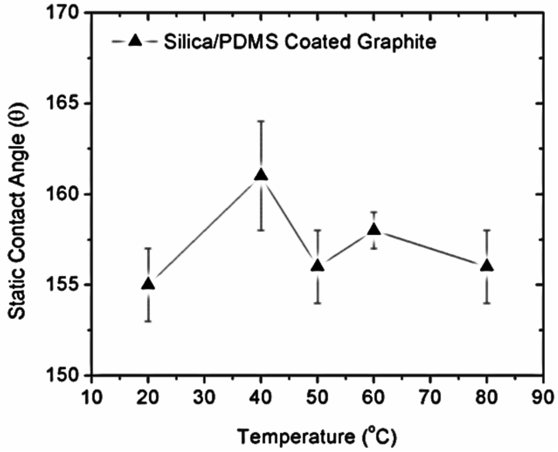

Figure 4.1: Silica/PDMS coated graphite static contact angle at different temperature.

4.1.2 Effect of Composite Coatings on Graphite Surface Topography and Roughness

Surface structure and roughness have a significant impact on the surface wettability as explained in the previous section [92]. Non-coated graphite surface is irregular with peaks and valleys [4] structure as shown in Figure 4.2a.

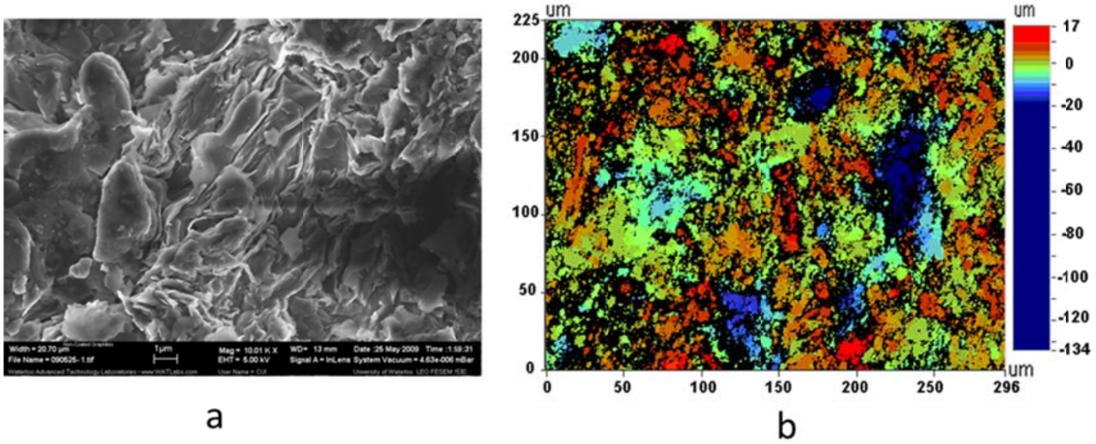

Figure 4.2: Non-coated graphite surface characteristics imaged by a) SEM image showing surface topography, and b) Profilometry image showing the surface roughness (Ra 4.23 µm; Rt 150.64 µm).

The peaks and valleys structure is confirmed by measuring average surface roughness (Ra) which is about 4.23 µm, and the height-to-valley distance (Rt) as approximately 150.64 µm. Unlike the non-coated graphite, the 262 nm silica particles/PDMS coated graphite (superhydrophobic) shows the silica particles are aggregated together like a caviar structure on the surface as shown in Figure 4.3a. Further, it shows lower average roughness (Ra = 2.85 µm) and less height-to valley distance (Rt = 33.23 µm) as seen in Figure 4.3b.

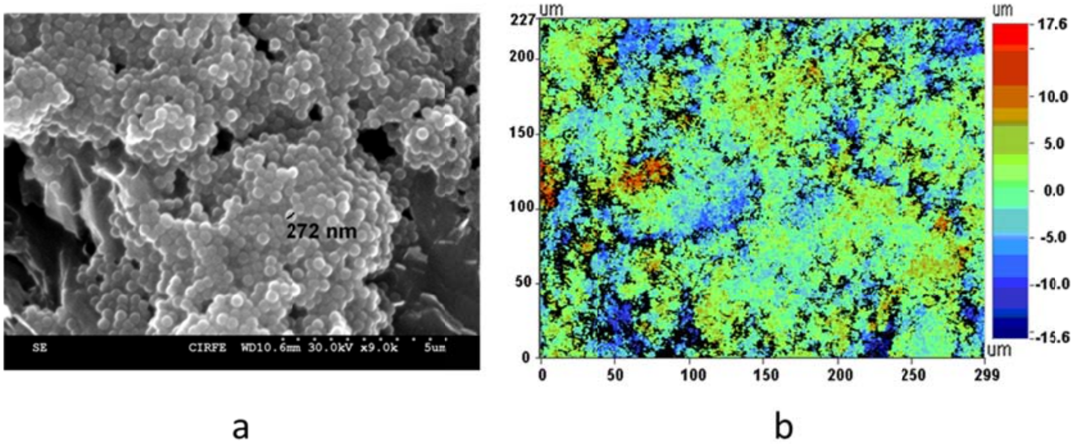

Figure 4.3: 262 nm silica particles/PDMS (superhydrophobic) coated graphite surface characteristics imaged by a) SEM image showing surface topography, and b) Profilometry image showing the surface roughness (Ra 2.85 μm; Rt 33.23 μm).

The caviar-like structure is formed due to the fast curing of PDMS in the composite coating. PDMS is cured not only on the top of the silica particles, but also in between the silica particles and connects them together. Further, it is observed that the surface configuration reduces the value of both the Ra and Rt significantly between the 262 nm silica particles/PDMS composite coating and non-coated graphite. As graphite coated with the 262 nm silica particle/PDMS composite, the Ra is 2.85 μm while the Rt is 33.23 μm, where the Ra value is almost doubled in the non-coated graphite (4.23 μm) and the Rt is roughly increased 4.5 times (150.64 μm). Recent experimental studies show that the surface roughness reflects only the average parameter of surface. Further, the surface configuration, like multi-scale or hierarchical structures also strongly influence the surface hydrophobicity, particularly sliding angle (α) on the surface. It is reported that two-tiered structures, made up of superposition of two scale (micro- and nano-) roughness patterns, may lead to the superhydrophobic characteristics [93-95]. The combination of micro- and nano-scaled structures can help to distort the gas-liquid-solid contact line, resulting in water droplet rolling on the surface. As to the coating of 262 nm silica particles/PDMS composite, the silica particles adjust the surface roughness, resulting in high contact angel (θ). Meanwhile, the nano-scaled silica particles aggregate together and form micro-scaled caviar-like structure on the graphite surface, and these two tiered micro-/nano-structures further decreases the contact angle hysteresis, resulting in lower α on the surface [96].

Based on the aforementioned results, the superhydrophobic property of 262 nm silica particles/PDMS composite coatings is obtained for three combined reasons: 1) the graphite surface energy reduction because of PDMS coating, 2) the surface roughness and structure of graphite are adjusted by silica particles, and 3) the quick curing of PDMS in the composite coating caused silica particles to form in a caviar like structure. These reasons formed a complex homogenous structure with low surface energy, resulted in superhydrophobic properties with low α. However, the non-coated graphite surface is full of irregular peaks and valleys. This heterogeneity causes a large contact angle hysteresis on the surface [97, 98], thus the water droplet is hard to slide on the surface.

PTFE can help to prepare a hydrophobic surface as a low surface energy material. The measured value of θ on PTFE-coated graphite surface is $145 \pm 5°$, and value of α is $67 \pm 1°$. It is noticed that θ value is larger than θ value on a flat pure PTFE surface ($\theta = 120°$) [99]. The improved surface hydrophobicity may be caused by the surface roughness of the original graphite. As it is shown in Figure 4.2a, the surface of non-coated graphite considerably has irregular features, and its Ra is 4.23 μm. PTFE coating on the graphite surface reduces the surface energy of the graphite surface; however, the structure of the PTFE coated graphite does not have a big difference to the non-coated graphite. Hence, the values of both Ra and Rt for the PTFE coated graphite are found to be 3.95 μm and 148.76 μm, respectively as illustrated in Figure 4.4. Thus, the value of α is kept high as $67 \pm 1°$, even though the PTFE material has low surface energy.

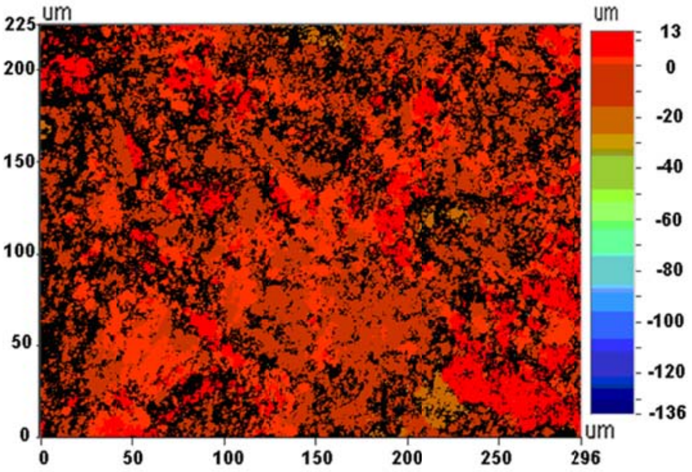

Figure 4.4: Profilometry image showing the surface roughness of PTFE coated graphite (Ra 3.95 μm**; Rt 148.76** μm**).**

Unlike the superhydrophobic, hydrophobic, and slightly hydrophobic surface properties, the superhydrophilic surface properties are obtained while the graphite is coated with 262 nm silica particles. Silica particles are hydrophilic materials due to existence of hydroxyl groups on their surfaces [91, 100]. Water droplets are generally spread on the coated surface and cannot be moved off even if the surface is tilted over 90°. Further, θ is sharply deceased to 15 ± 2° compared with non-coated graphite (θ = 95 ± 2°) as illustrated in Table 4.1. The superhydrophilic properties of silica coated graphite surface, is obtained from the combined two reasons: 1) the hydrophilic nature of the silica particles which is more dominant than 2) the structure and roughness of the coated surface which reinforce the hydrophilic properties [101]. Silica particles are randomly distributed over the graphite surface as shown in Figure 4.5a. In addition they reduce both values the Ra and Rt of the non-coated graphite to 2.8 μm and 39.33 μm, respectively as illustrated in Figure 4.5b.

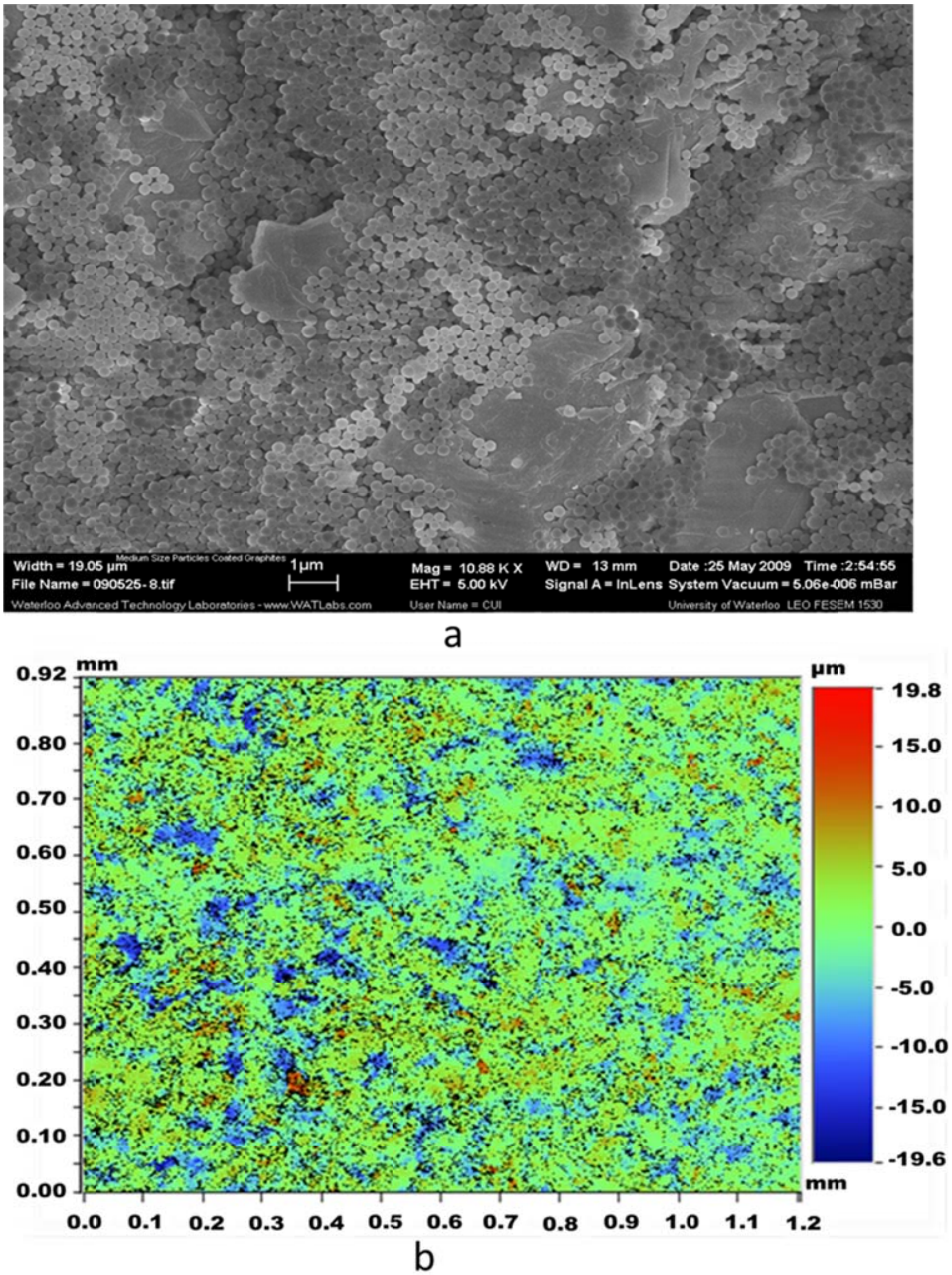

Figure 4.5: Silica coated (superhydrophilic) graphite surface characteristics imaged by a) SEM image showing surface topography, and b) Profilometry image showing the surface roughness (Ra 2.8 μm; Rt 39.33 μm).

4.1.3 Stability of Composite Coating on Graphite

It is well known that the PEM fuel cell components especially those inside the cell are exposed to harsh environment inside the cell while it is running. This environment includes: vibration, high temperature up to 80 °C, humidity, and byproducts of the reactions. Thus, the composite material coatings on the cell components are important to be stable and durable. In order to test the stability of the 262 nm silica particles/PDMS composite coating, the coated graphite squares pieces (2 cm × 2 cm) are immersed in DI water and put into a shaker. Next, the shaking rate is set at 40 rpm and temperature is controlled at 80 °C. The samples are picked up periodically, upon the water contact angle measurements as shown in Figure 4.6.

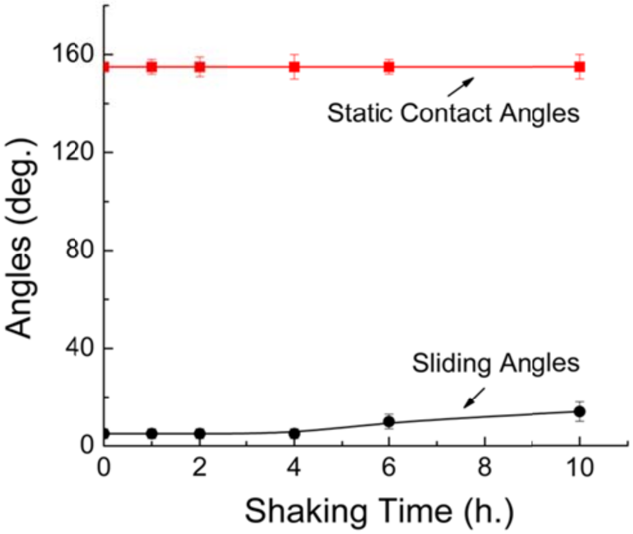

Figure 4.6: Durability of the graphite surface coated with 262 nm-sized silica particles/ PDMS composite through a shaking test. Shaking rate: 40 rpm; temperature: 80 °C.

As it can be seen in Figure 4.6, contact angel (θ) shows almost no changes, around 155° after 10 hours shaking. However, sliding angel (α) on the coated graphite square sample is stable for the first 6 hours at 10°, but it increases to 15° in 10 hours. At this stage water droplets could still easily move on the graphite surface. This is relevant to the nature of the PDMS material softness and flexibility, which allow part of silica particles to move. Hence, long time shaking may lead to moving of the silica particles in the composite coating and result in changes of surface roughness.

4.1.4 Channel Wettability Effect on Two-Phase Flow Characteristics

4.1.4.1 Two-phase Flow in Slightly Hydrophobic and Superhydrophilic Channels

Figure 4.7 shows a typical flow pattern for the superhydrophilic channel and slightly hydrophobic channel. The static contact angle (θ) is measured between the channel walls and the water film profile as presented in Figure 4.7 c. Although the non-coated graphite channel is slightly hydrophobic, water can still stick/attached to its surface as in Figure 4.7 a. The contact angle profile is around ($\theta = 96 \pm 4°$).

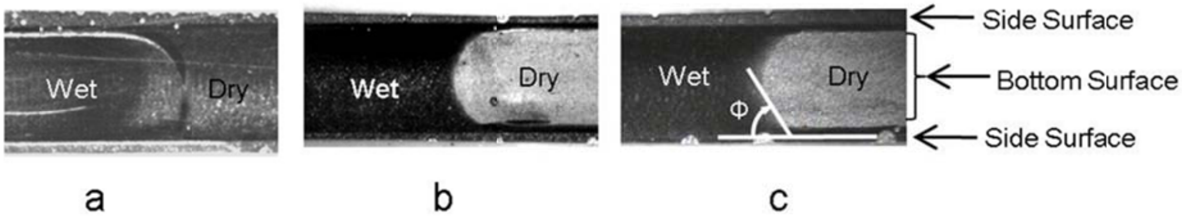

Figure 4.7: Top view of the two-phase flow in: a) slightly hydrophobic b) superhydrophilic channel at J_L= 0.015 m/s and J_G = 4.81 m/s and c) shows channel walls and the measured contact angle profile.

When water is moving forward along the channel, due to the strong interaction between water and the graphite surface, a long tail is left behind the water slug. This is attributed to the high surface tension ($\theta = 96 \pm 4°$). With regard to superhydrophilic channel ($\theta = 66 \pm 1°$), it is found that water quickly spreads as a thin film over the bottom of channel. This is attributed to the hydrophilic nature of silica particles, which attracts the water droplet because of higher surface tension compared with the slightly hydrophobic channel. Furthermore, water moves faster at the corners than through the bottom, which is probably caused by the stronger capillary force at the corners. It appears two wings dragging the water film forward as illustrated in Figure 4.6 b.

After thin film is formed in the channel, the air travels above the thin film. Due to the shear stress between water and air, the air drives the thin film out of the channel. The required shear stress to drive the thin film out of the superhydrophilic channel is higher than the non-coated graphite one as a result of higher surface tension. This will be explained in the pressure measurement section.

4.1.4.2 Two-Phase Flow in Hydrophobic and Superhydrophobic Channels

In this section two different channels are tested. First channel is coated with PTFE where water static contact angle is 145 ± 5° on its surface and the second one is coated with 262 nm-sized silica particles /PDMS with water static angle of 155 ± 2° on its surface. Although the difference in static contact angle is about 10° between these two channels, but the variation in the sliding angle is around 48° as shown in table 4.1. As a result, the water droplet in the superhydrophobic channel has more uniform spherical shape, and the droplet tends to roll on the surface without any distortion or irregularities in shape. Figure 4.8 c and d illustrates these descriptions. In contrary, the droplets in the hydrophobic channel is distorted and it has a non-uniform shape as depicted in Figure 4.8 a, and b.

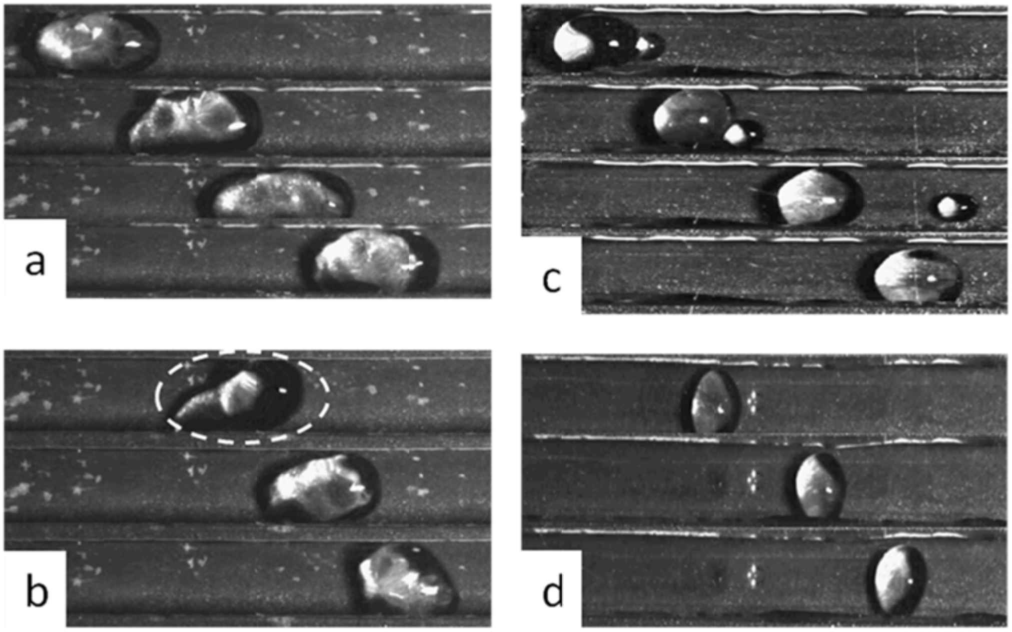

Figure 4.8: Two-phase flow images in different channels at different $J_L \times J_G$ (*m/s*); a) Hydrophobic (0.015 × 3.63) b) Hydrophobic (0.015 × 6.17) C) Superhydrophobic ((0.015 × 3.63) and d) Superhydrophobic channel (0.015 × 6.17).

A tail shape is attached to the right side of droplet as circled in Figure 4.8 b. This indicates that the droplet is slipping on the surface and not completely rolling. In other words, the droplet is sticking on the surface but at the same time the drag force due to the air flow is enough to slip the droplet on the surface and move it through the channel.

The sliding angle effect can be significant in blocking the channel as illustrated in Figure 4.9. The small droplet (D1) sticks on the hydrophobic graphite channel surface till another droplet (D2) approaches closely to D1 and collide with it. As a result the channel blockage occurs. After a certain time of bouncing forward and backward between D1 and D2 the pressure will start to build up at the channel inlet until both droplets will be discharged from the channel as described in Figure 4.9 a. Meanwhile, even a small droplet on the superhydrophobic coated channel does not stick and moves with shorter time at similar J_G as can be noticed in Figure 4.9 b. This can be attributed to the less attraction of the water droplet on the superhydrophobic channel than the hydrophobic one.

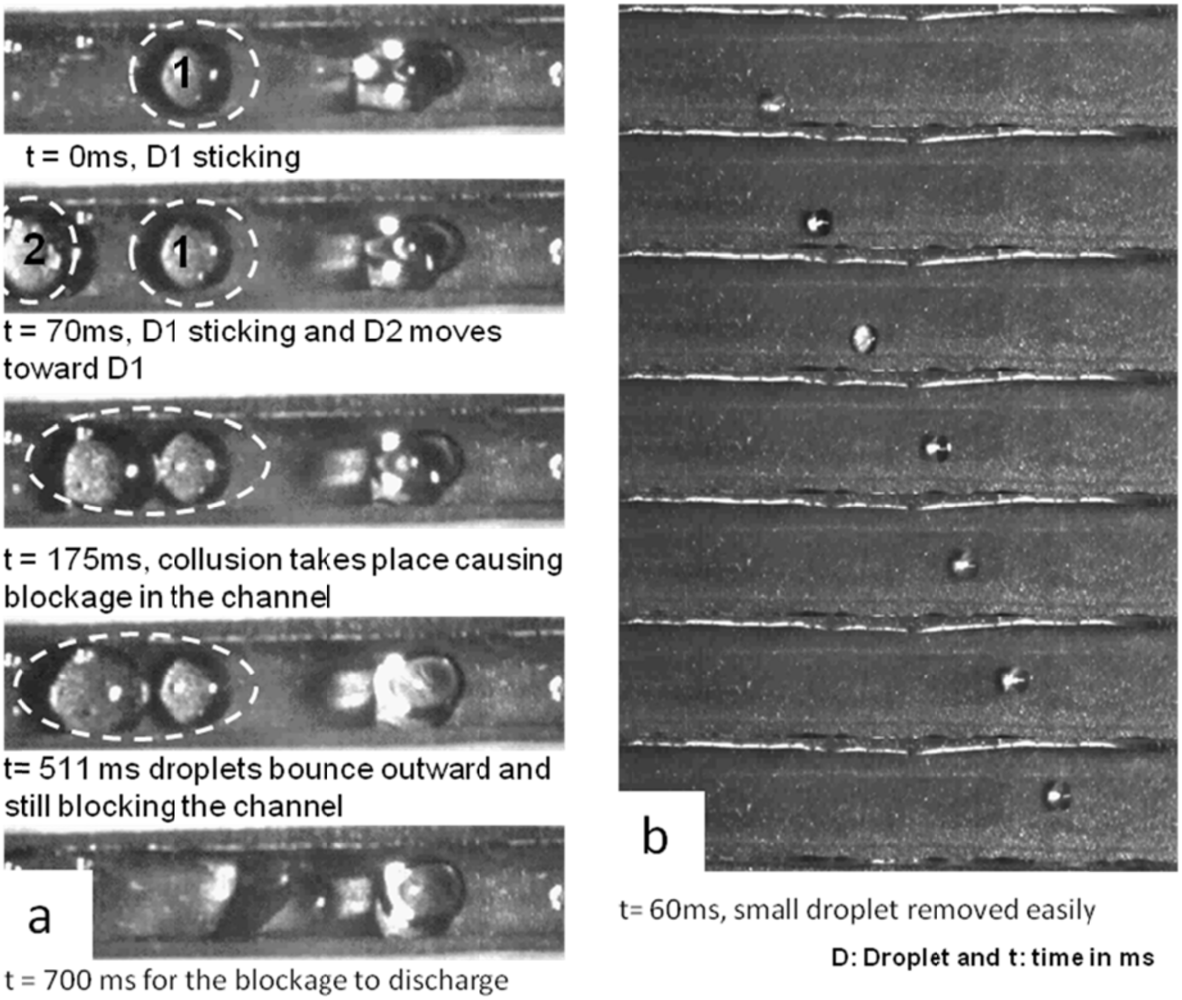

Figure 4.9: Effect of sliding angle on water removal a) channel blocking takes place ($\alpha = 67 \pm 1°$) b) small droplet removed easily ($\alpha = 19 \pm 1°$).

The sliding angle depends on the surface roughness and surface homogeneity, which allows high air ratio interface between solid and water as discussed earlier. This results in lower sliding angle and lower surface interaction with the water droplet. Wang *et al.* [96]

found that the 262 nm-sized silica particles/PDMS coated with graphite channel revealed that silica particle are aggregated like caviar structure on the macro-level which allows more air ratio to be trapped between the solid and water. On the contrary, the hydrophobic coated channel showed an inhomogeneous surface with peaks and valleys.

4.1.4.3 Two-Phase Flow in Combined Surface Wettability Graphite Channel

The bottom surface of the combined surface wettability channel is coated with 262 nm-sized silica particles/PDMS (superhydrophobic) and side walls, are non-coated graphite (slightly hydrophobic). The sliding angle for the slightly hydrophobic surface is over 90° and 19 ± 1° for the superhydrophobic surface. It is noticed that the droplet sticks on the side walls of the channel while it is travelling through the channel, even at higher air flow rate the droplet sticks on the side surfaces. This can be attributed to the high surface tension and high sliding angle of the side walls as shown in Figure 4.10 a, and b.

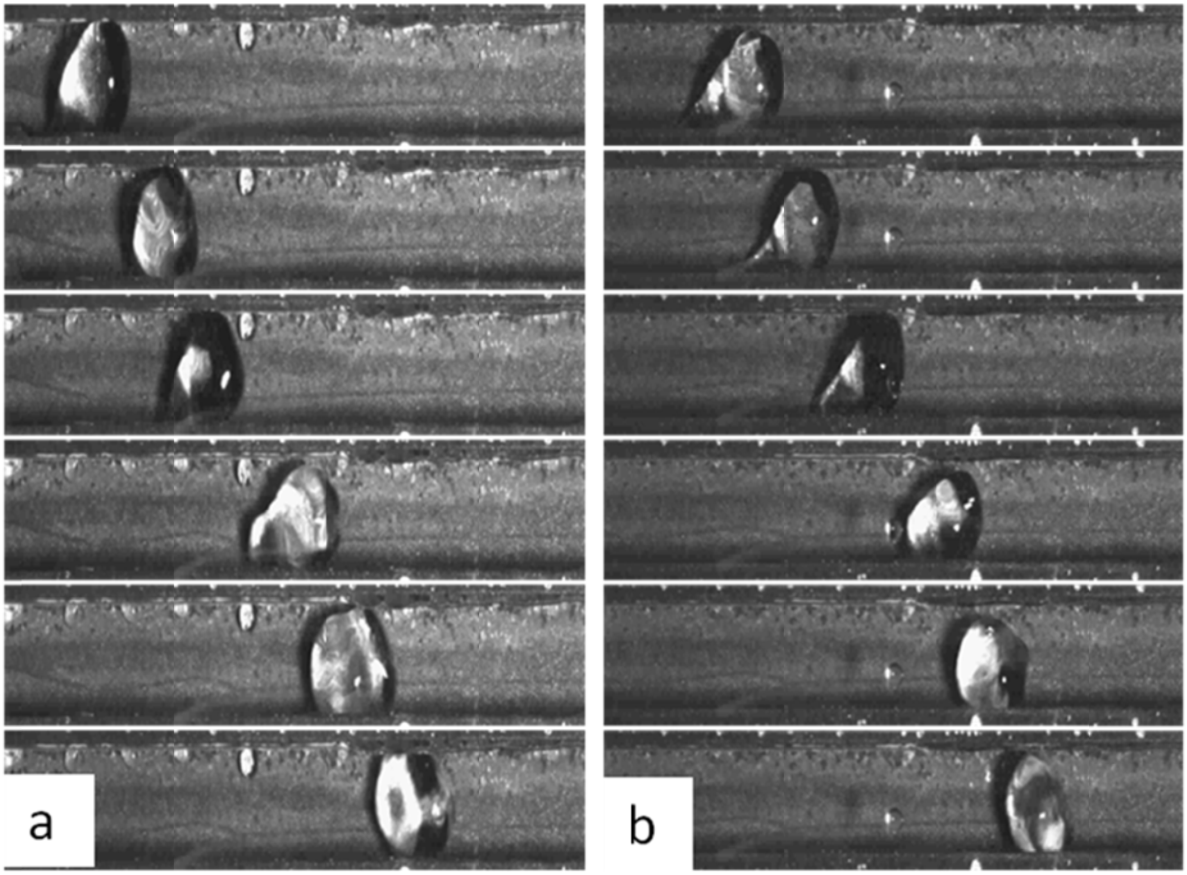

t = 180 ms for the droplet to travel through the channel

t = 125 ms for the droplet to travel through the channel

Figure 4.10: Two-phase flow images in the combined surface wettability channel at J_L = 0.015 m/s and different air superficial velocities; a) J_G = 4.81 m/s and b) J_G = 8.61m/s.

As depicted in Figure 4.11, the required time for the droplet to travel through the channel at 0.0146 × 4.81 m/s for water and air superficial velocities ($J_L \times J_G$) respectively, is 180 ms. Meanwhile, at similar superficial velocities, the time needed for almost the same droplet size to travel through a superhydrophobic channel is about 90 ms.

4.1.5 Relationship between the Two-Phase Flow Resistance and. Surface Wettability

The slow movement of the water slug allows more water to accumulate in the channel. This accumulation leads to two slugs travelling at different levels. The hydrophobic slug travels inside the channel (bottom surface of the channel), whereas the hydrophilic one travels on the plexiglass s surface (top of the channel); as shown in Figure 4.11. In order to reduce the influence of the plexiglass s surface on pressure measurements, the channel is covered with hydrophobic GDL as can be seen in Figure 3.4/ section 3.3.4.

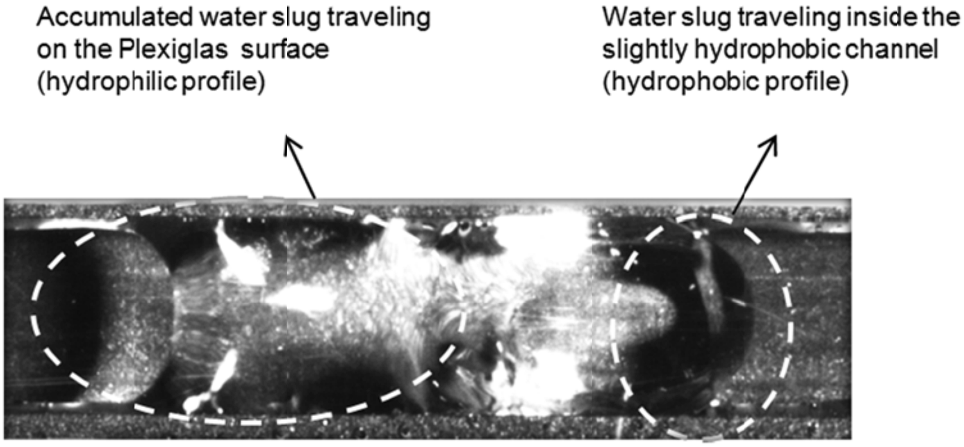

Figure 4.11: Two-phase flow image in slightly hydrophobic channel at J_L = 0.015 m/s J_G = 1.01 m/s.

Pressure values are measured by fixing J_L and changing J_G as it is illustrated in Figure 4.12. It is clear that the superhydrophobic surface results in lowest pressure values at low and high J_L compared to the rest of the channels. This can be attributed to the low sliding angle ($\alpha = 19 \pm 1°$) of the superhydrophobic channel compared with the slightly hydrophobic and the hydrophobic channels. In addition, the hydrophobic surface shows the highest pressure values at J_L = 0.015 m/s. This is due to the high sliding angle ($\alpha = 67 \pm 1°$), which causes small droplets to stick on the surface and block the channel, resulting an increase in the pressure as shown in Figure 4.12 a, b, and c. However, the slug and the thin film in the slightly hydrophobic and superhydrophilic channel, keep the channel unblocked, resulting in lowering the pressure values than in the hydrophobic channel whereas higher pressure values are obtained at higher J_L values in the superhydrophilic channel. This is caused by high interaction between the channel walls and the liquid water film, which might require a higher air flow to move the water through the channel in order to discharge it out of the channel as illustrated in Figure 4.12d.

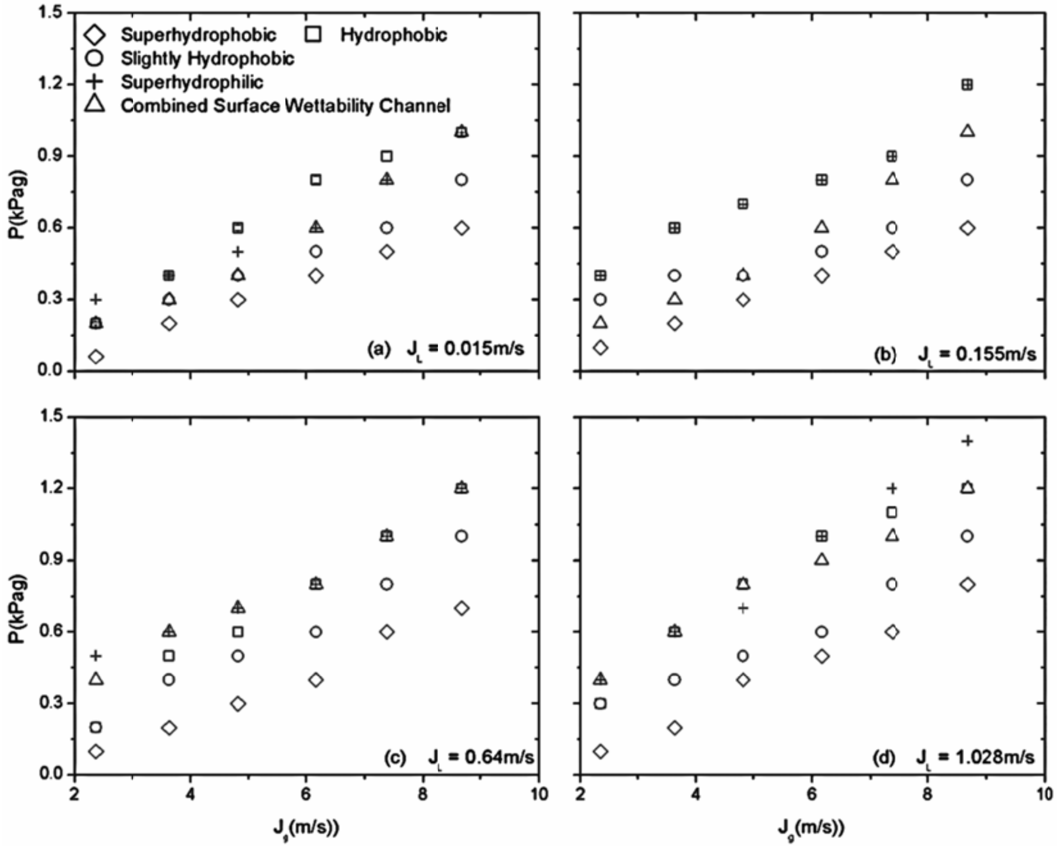

Figure 4.12: The comparison of pressure drop Vs. J_G at fixed J_L of five different channels with different surface wettability; (◇) superhydrophobic, (□) hydrophobic, (○) slightly hydrophobic, (+) superhydrophilic, and combined surface wettability and at J_L a) 0.015, b) 0.155, c) 0.64, and d) 1.028 m/s.

The channel with combined surface wettability shows higher pressure value compared with the slightly hydrophobic surface. Also in some regions the same value as the superhydrophilic channel especially at J_L = 0.015, and 0.64 m/s as shown in figure 4.12 a, and c. This might be elucidated to the droplets sticking on the side walls of the channel, resulting in narrowing the air passage and causing pressure to rise at the channel inlet as illustrated in Figure 4.10. Nevertheless, the slightly hydrophobic and superhydrophilic channel water slug, and thin film keep the air passage open, resulting in lower pressure or equal pressure values with other channels at J_L = 0.015, and 0.64 m/s .

As shown in Figure 4.12, the pressure difference needed to drive the flow for the superhydrophobic channel is very small, close to zero, for the superficial air velocity close to 2 m/s. This is because the pressure meter used in the experiment has a limited sensitivity and accuracy, and the nearly zero reading for the pressure difference represents the pressure drop is so small that the pressure meter is not giving a noticeable reading.

4.1.6 Relationship between the Two-Phase Flow Resistance and Sliding Angle

From the previous results, the sliding angle effect on the two-phase flow resistance can be summarized in Figure 4.13. The sliding angle has a significant effect on the pressure drop through the channel. The pressure drop along the flow channel increases as the sliding angle value rises, even at the same J_L and J_G values. The pressure drop also increases when the J_L is fixed and J_G is increased with sliding angle increment as seen in Figure 4.13 a, b, c and d. Increasing J_L with the sliding angle leads to significant increments in pressure drop as clearly noticed in Figure 4.13 c, and d. This is attributed to the increment of the adhesion force due to high sliding angle. Increasing the adhesion force raises the drag force required to move the droplet inside the channel, thus the pressure drop increases accordingly.

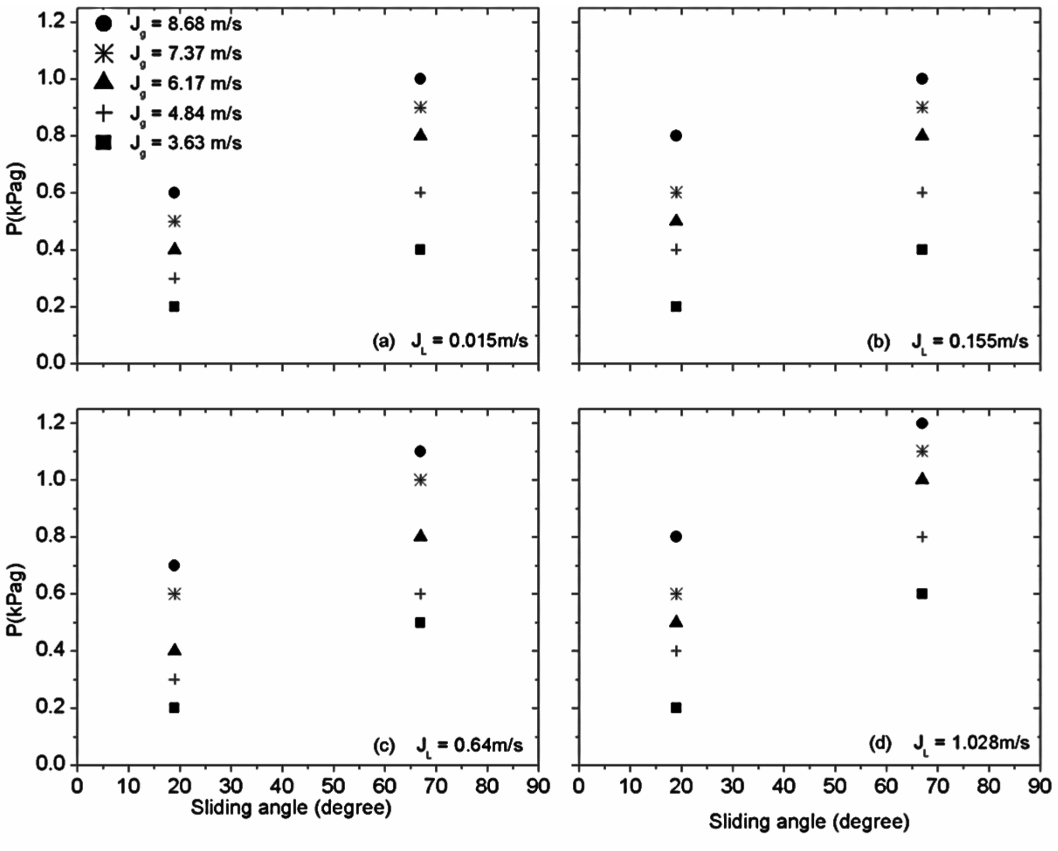

Figure 4.13: The comparison of pressure drop vs. sliding angle at J_G; (■) 3.63, (+) 4.84, (▲)6.17, (*) 7.73, and (●) 8.68 m/s and at J_L a) 0.015, b) 0.155, c) 0.64, and d) 1.028 m/s.

From the previous results, it was shown that when the sliding angle was 19° the contact angle estimated to be 155 ± 2° for the superhydrophobic surface, and when the sliding was 67° the contact angle was 145 ± 5°. In other words, when the sliding angle of a droplet on a rough surface is increased, the contact angle on the same surface is decreased. This indicates that the rough surface becomes more wettable and attracts the water droplet with higher surface tension due to lower amount of entrapped air beneath the water droplet. Thus, the adhesion force increases and higher drag force is required to move the droplet on the rough surface, consequently the pressure drop through the channel is increased.

4.1.7 Relationship between the Two-Phase Flow Resistance and Static Contact Angle

In the hydrophilic region (0° - 95°) as static contact angle decreases, the pressure drop along the flow channel increases. This is depicted in Figure 4.14. The pressure values are significantly increased at 15° when J_L is raised compared with the pressure values at 95° at the same J_G. This is attributed to the high surface tension between the channel surface and water, which spreads as a thin film on the surface. This suggests that for contact angle of 95° the amount of pressure decreases due to the lower surface tension between the water slug and the channel surface.

In the hydrophobic region, even though the difference between the two angle is only 10°, but the pressure drop at 145° is much higher than 155° as shown in Figure 4.14 a, b, c and d. This is projected by the higher sliding angle at 145° than 155°; which are 67° and 19°, respectively and shown in Figure 4.13. According to earlier discussion, on the hydrophobic surfaces, when the droplet is formed on the surface; lower sliding angle results in lower adhesion force between the channel surface and the droplet. This lowers the drag force required to move the droplet to the channel exit which reduces the amount of pressure drop and vice versa.

As illustrated in Figure 4.13 and Figure 4.14, static contact angle is more dominant in affecting the pressure drop through the channel in the hydrophilic region, and sliding angle is more dominant in affecting the pressure drop in the hydrophobic region. In the hydrophilic region pressure drop increases with decreasing the static contact angle and in the hydrophobic region the pressure drop increases with increasing the sliding angle.

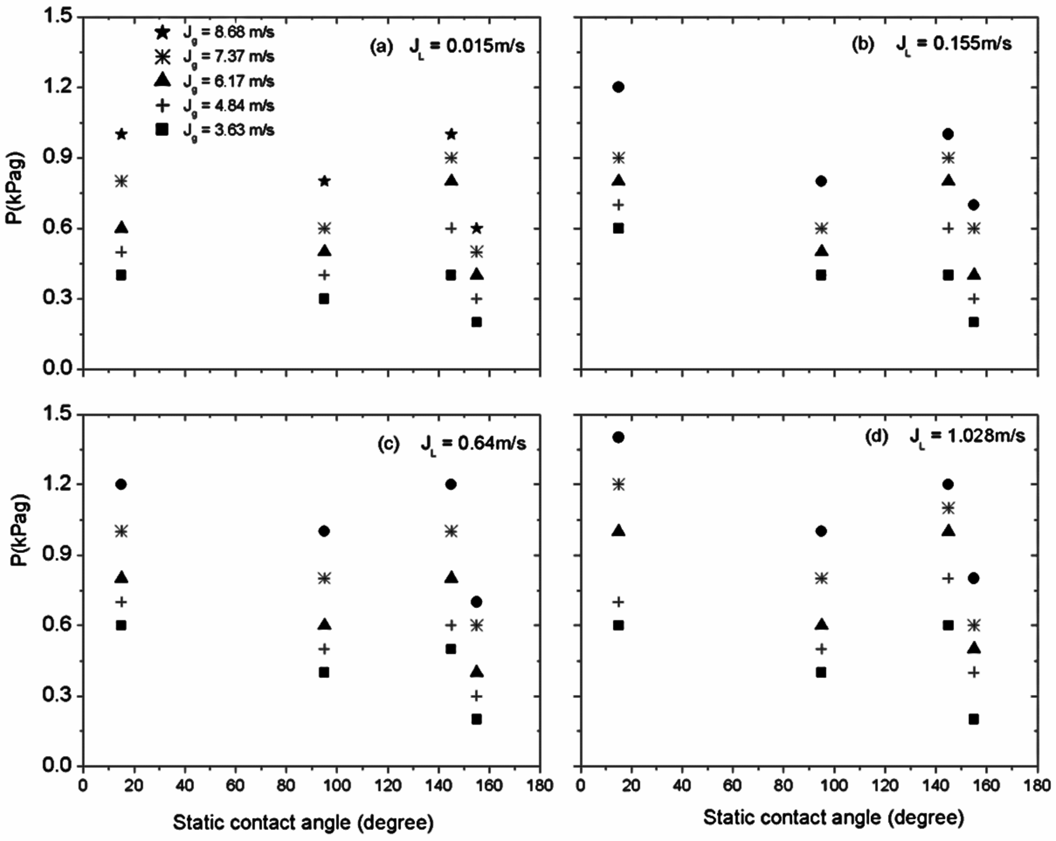

Figure 4.14: The comparison of pressure drop vs. different static contact angles; 15°, 95°, 145°, and 155° at J_g; (■) 3.63, (+) 4.84, (▲) 6.17, (*) 7.73, and (●) 8.68 m/s and at J_L a) 0.015, b) 0.155, c) 0.64, and d) 1.028 m/s.

The highest values of the pressure drop are noticed at 15° static contact angle at the highest J_L value. This indicates that, the superhydrophilic surface requires higher amount of air flow to push the water out of the channel as shown in Figure 4.14 d.

4.1.8 The Effect of Different Surface Wettability Channels on PEM Fuel Cell Performance

Since the superhydrophobic and superhydrophilic channel surfaces present the lowest and the highest resistance of the air-water flow respectively, as shown in Figure 4.12, PEM fuel cells performance tests with the cathode superhydrophobic and superhydrophilic coated and slightly hydrophobic (commercial use) gas flow channels are conducted as described in Figure 4.15. It can be seen that the coated cells shows lower performance especially at low current density values. This signifies the effect of the nonconductive 262 nm-silica particles and 262 nm-silica particles/PDMS composite coating used in present work compared with non-coated gas flow channels. On the other hand, superhydrophobic cathode gas flow channels have a positive impact on the fuel cell overall performance especially at high current density. This may be attributed to the concentration over potential at the reaction sites (electrode). This suggests that a ‘flooding’ condition, which may be caused by the trapping water inside slightly hydrophobic and superhydrophilic gas channels, is due to high interfacial tension and high sliding angle. These phenomena will lead to blockage of both the gas flow channels and GDL pores by generated/accumulated water, respectively. Hence, the cell performance is improved at high current density using the superhydrophobic coating with high water repellency. Furthermore, the condensed water product tends to accumulate water drops in gas flow channels. These droplets can be swept away more easily by gas stream in the superhydrophobic gas channels than that of the slightly hydrophobic and superhydrophilic ones.

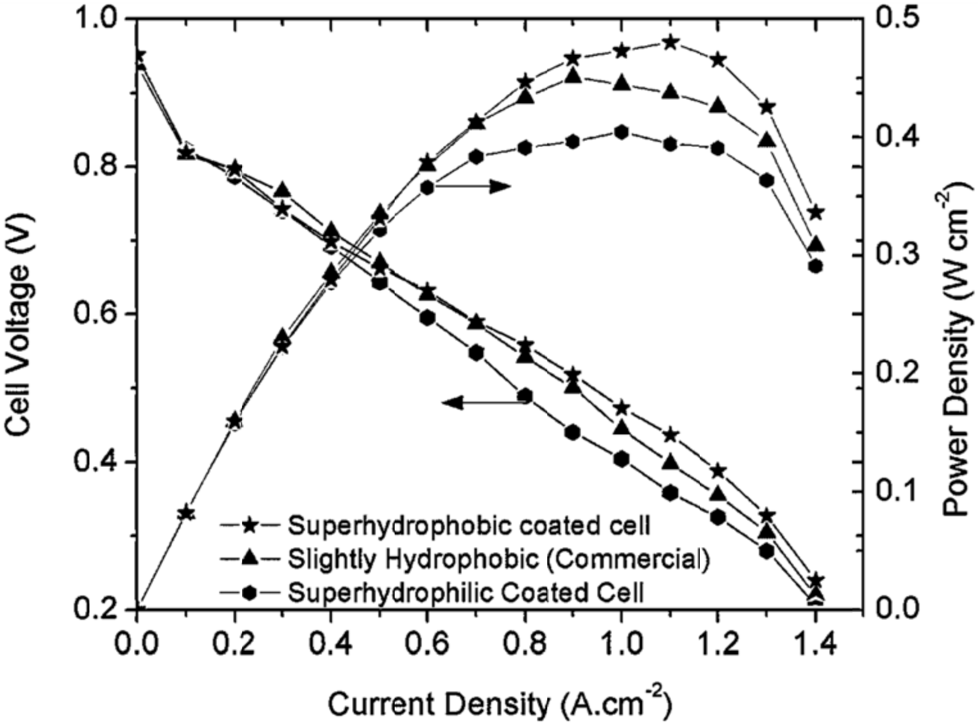

Figure 4.15: Experimentally measured PEM fuel cells performances curves comparisons; (★) superhydrophobic coated cell, (▲) slightly hydrophobic cell and (●) superhydrophilic coated cell at the following operating conditions: anode and cathode back pressure 25kpag, cell temperature of 65 °C, stoichiometric ratio 2 for the cathode air stream and 1.2 for the anode hydrogen stream, fully humidified for both cathode and anode gas streams.

As noticed in Figure 4.15 the difference in cell performance curves is more noticeable in the ohmic and concentration over potential regions due to the water generated at the cathode side in those regions. Meanwhile, the difference is very small at the activation over polarization region due to the low water content and generation at the cathode side compared with the other regions. Further, the difference in the cell performances is in the range of 10-30 mv. This refers to the small active area of the cell 40 cm^2, resulting in lower amount of generated water at the cathode side compared with larger cell. Scaling up to larger cell increases the active area of the cell and the amount of generated water at the cathode side, resulting in more water accumulation inside the cathode gas flow field channels which have the same cross section area of the small cell gas flow field channel (1 mm × 1mm). This leads to lower cell performance significantly of the large cell compared with the small one under the same running conditions [102, 103]. Thus, the improvement in cell performance using superhydrophobic surface might be more significant in the large cell than the small one.

Even though the difference in the cell performances curve shows a small difference, but these data shows at least 95% confidence limit in the measured data. This limit is based on the uncertainty associated with the standard deviations of the measured voltage values at a fixed current density as shown in Figure 4.16a.

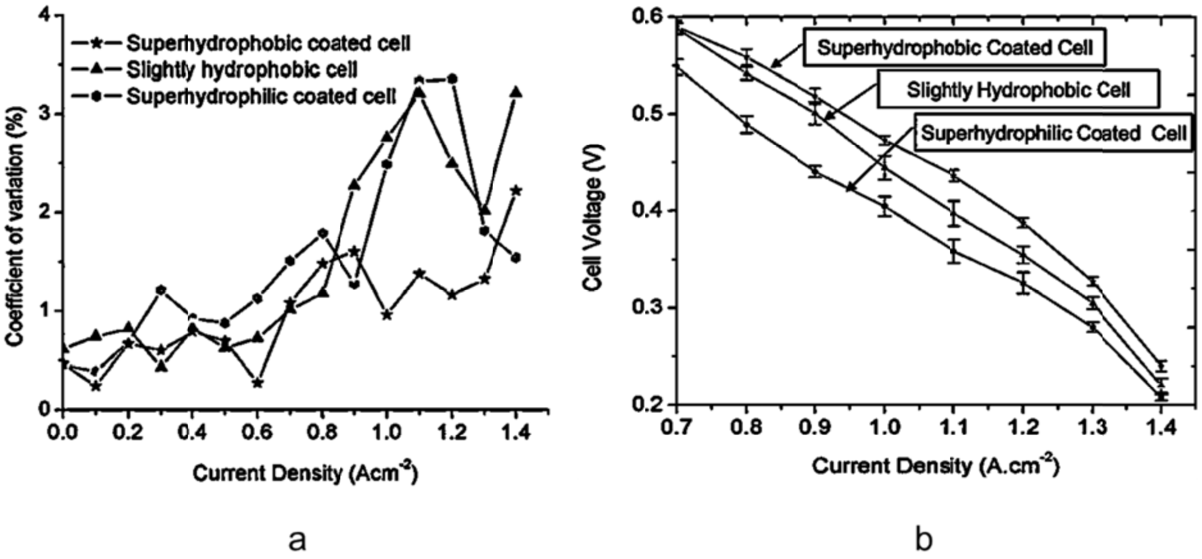

Figure 4.16: Uncertainty of the measured voltage; a) Coefficient of variation of the measured voltage for the three different coated fuel cells (★) Superhydrophobic coated cell, (▲) slightly hydrophobic cell and (●) Superhydrophilic coated cell, and b) PEM fuel cell performances from 0.7 A.cm^{-2} to 1.4 A.cm^{-2} showing the error bars at each measured voltage (the symbol size of the measured voltage is minimized to show error bars clearly)

Superhydrophobic coated cell shows smaller fluctuations and error bars in the measured voltage values as shown in Figure 15 a, and b, respectively. This refers to less water accumulations in cathode gas flow field channels and less flooding in the cathode gas diffusion layer compared with the slightly hydrophobic and superhydrophilic coated cells.

4.2 Effect of Composite Coatings on Gas Diffusion Layer (GDL) Characteristics, Wettability, and Overall PEM Fuel Cell Performance

In this section, the new coating materials; silica particles, PDMS, and silica particles /PDMS composite will be discussed and compared with the non-coated GDL and commercial GDL (30 wt. %PTFE coated GDL with MPL).

4.2.1 Influence of Composite Coatings on Surface Wettability

4.2.1.1 Hydrophilic Coating of GDL with Silica Particles

As mentioned earlier silica particles used in this study have hydrophilic properties because of the existence of hydroxyl groups on their surfaces. A GDL coated with such particles also shows a strong surface hydrophilic property. The static contact angle (θ) on the surface of non-coated GDL is 107 ± 2° as illustrated in Table 4.2. However, once the GDL is coated with 3.5 wt. % of 262 nm silica particles, it sharply decreases to almost 0° Further, it is found that water droplet (10 µl) does not only spread over the surface, but also is drawn through the GDL plane at the same time. This phenomenon is probably due to the hydrophilic nature of silica particles and the capillary forces driving through the pores located between these silica particles. Both of these features are beneficial to the distribution of liquid water within the GDL.

Table 4:2: Water static contact angle and sliding angle on the surfaces of different coated GDL samples.

No.	Coating Material	Wettable Property	θ	α
1	262 nm Silica/PDMS	Superhydrophobic (Sandwich wettability GDL)	162 ± 2°	5 ± 1°
2	PDMS	Hydrophobic	138± 3°	≥ 90°
3	Raw	Slightly Hydrophobic	107± 2°	≥ 90°
4	262 nm Silica	Superhydrophilic	0°	Thin Film
5	PTFE	Superhydrophobic (commercial GDL)	165 ± 2°	2 ± 0°

4.2.1.2 Hydrophobic Composite Coating on GDL

Other function of silica particles is to assist low surface energy material PDMS to prepare high water repellant GDL. It is found that once a composite of silica particles/PDMS is coated on GDL, water droplets would not spread on the surface any more, instead it can slide on the surface. With reference to previous discussion, the surface hydrophobicity of solid could be enhanced by two factors, low surface energy material (PDMS) and suitable surface configuration (adjusted by silica particles). To evaluate their contributions to surface hydrophobicity, a comparison on the water contact angle is made by controlling their respective loadings on the GDLs, as shown in Figure 4.17. On a GDL coated with 3.50 wt. % of PDMS, θ is138 ± 3°, but water droplets are hard to slide on this surface even when it is tilted over 90°. When the GDL is coated sequentially with 1.97 wt. % of 262 nm-silica particles and 3.14 wt. % of PDMS, θ is increased to 157 ± 2°, and α is about 28°. Additionally, when the GDL is coated sequentially with 3.64 wt. % 262 nm-silica particles and 1.72 wt. % PDMS, θ reached 162 ± 2°, and α decreased to 5°. In this case, water droplets could easily roll on the surface. Such hydrophobic property is comparable with the commercial GDL as illustrated in Table 4.2. The results also suggest that the relatively high ratio of silica particles to PDMS in the composite is helpful to attain superhydrophobic GDL.

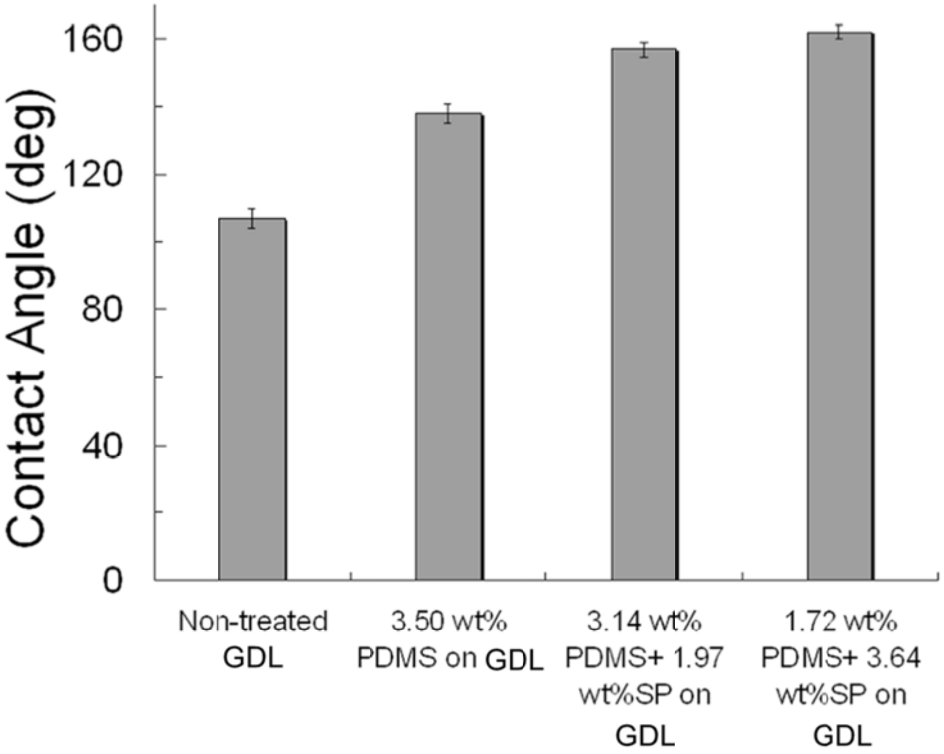

Figure 4.17: Water droplets static contact angles on non-coated GDL and GDLs with different loadings of silica particles (SP) and Polydimethylsiloxane (PDMS).

In this study, a general formulation is made with the composite: 3 wt. % of 262 nm silica particles mixed with 1 wt. % of PDMS in THF, and referred to as 262nm silica particle/PDMS composite.

4.2.2 Effect of Composite Coatings on GDL Surface Topography and Roughness

To understand the effect of composite coatings on surface wettability, the surface topography of GDLs samples are characterized using SEM and surfaces' roughness are measured using Profilometry. As mentioned earlier, non-coated GDL is manufactured using randomly arranged carbon fibers, between which there are many random pores as shown in Figure 4.18.

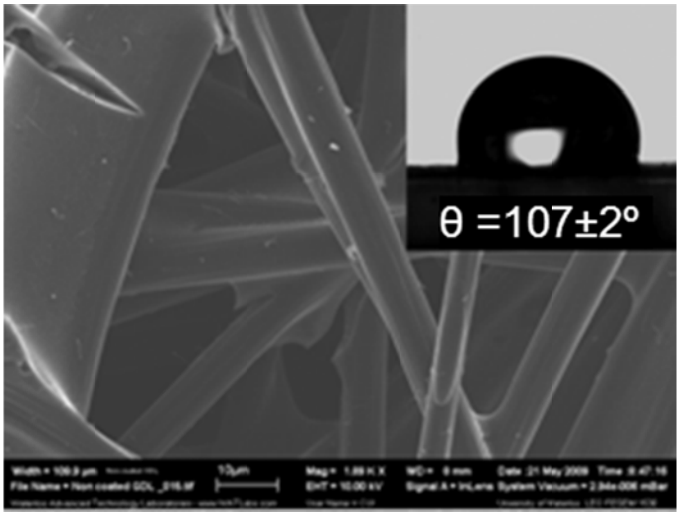

Figure 4.18: SEM image of raw gas diffusion layer; inset shows 10 µl water droplet contact angle on the gas diffusion layer surface.

In the case of commercial GDL, a micro-porous layer (MPL) is added on the carbon paper as depicted in Figure 4.19. The inset of Figure 4.19 shows that large pores have been completely covered by micro powders, which have resulted in formation of many micro-pores between them. Further, cracks are also found in the MPL layer. Nguyen *et al.* [104] observed that cracks in the MPL were much larger than the average pore size of MPL, and allowed liquid water to bypass the pores in MPL, resulted in much lower capillary pressure. Thus, a PEM fuel cell which uses GDL loaded with MPL with cracks will have worse performance.

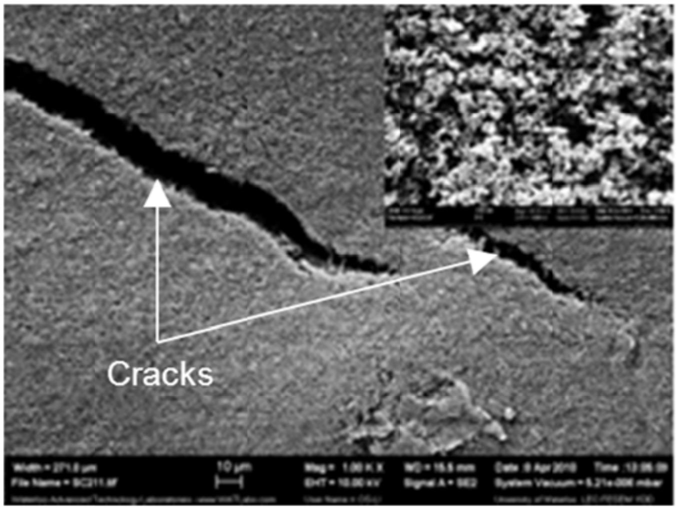

Figure 4.19: SEM image of commercial gas diffusion layer showing some cracks in the micro-porous layer; inset shows the pores of the micro porous layer (MPL).

In this work, silica particles are used to assist the water distribution inside the GDL. Once the GDL is coated with 262 nm silica particles, part of the original pores, especially the micro-pores, are filled with the close-packed particles as shown in Figure 4.20.

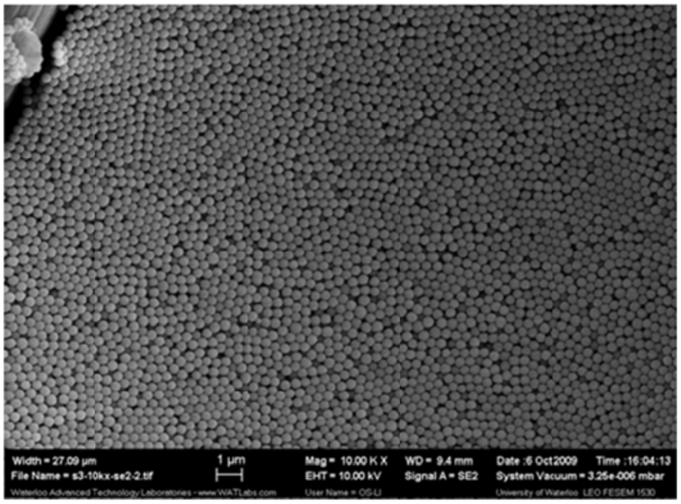

Figure 4.20: SEM image of 262 nm silica particles coated gas diffusion layer (GDL).

The silica particles disperse very well on the surface with small spaces between particles, and can be easily recognized. However, When the GDL is coated with a 262 nm sized silica particles/PDMS composite, the particles are bonded together to form irregular micro-scaled blocks, which are probably due to the PDMS used in the composite as shown in Figure 4.21 a, b, and c.

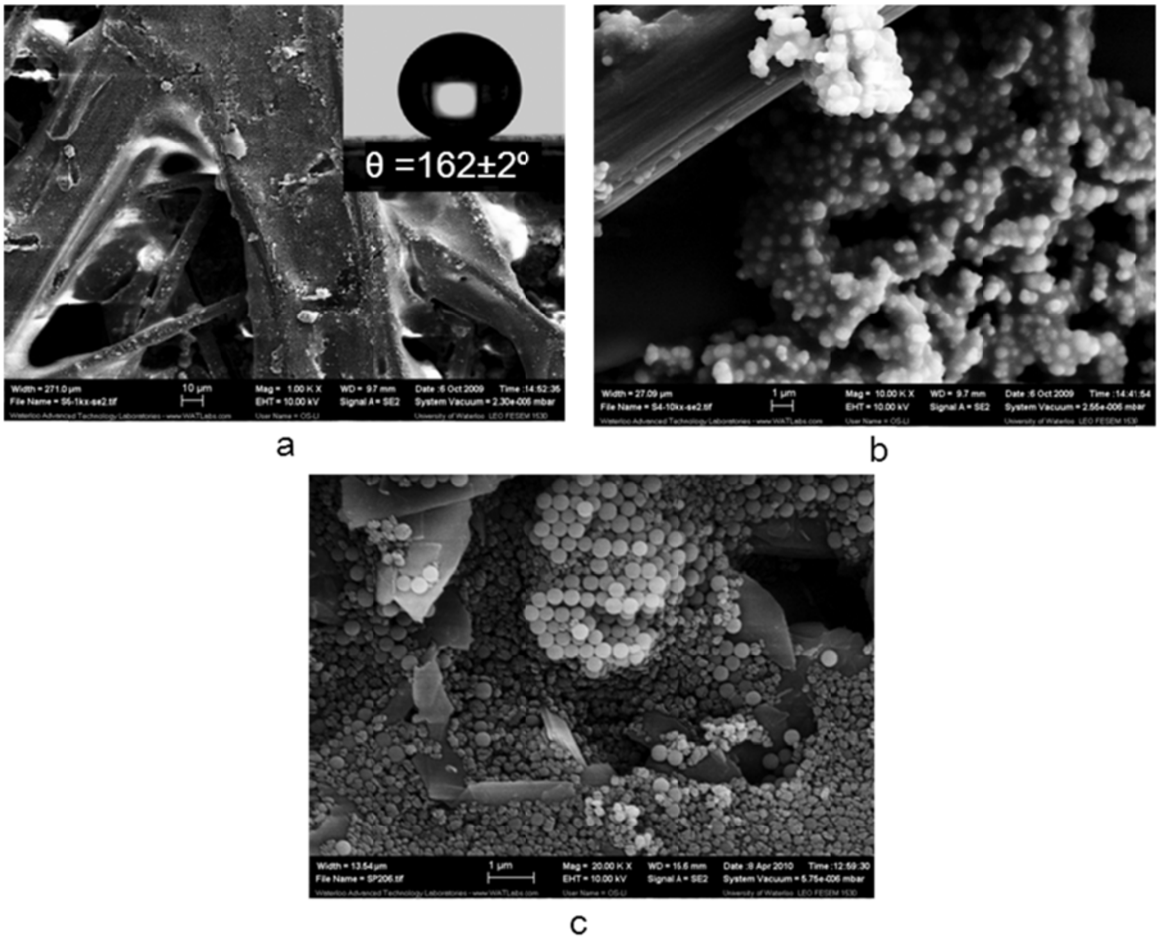

Figure 4.21: SEM image of 262 nm silica particles/ PDMS composite coated gas diffusion layer; (a) and (b) top view; c) inner cross section; and the inset in (a) shows the contact angle of 10 µl water droplet on the gas diffusion layer surface.

As it was discussed, the two-tiered micro-/nano- structure are beneficial in enhancing the surface hydrophobic property. Therefore, the measured water contact angle on this composite coating is around 162 ± 2° as illustrated in Table 4.2. Figure 4.21 c shows the cross section of GDL coated with the composite. The irregular small particles are the binders. Silica particles scattered among the binders or aggregated together, have kept their original appearance. This morphology probably suggests that the PDMS is mainly cured with silica particles on GDL surfaces. In other words, the hydrophilic nature of silica particles should be kept with them inside the GDL.

In addition to surface morphology, the surface roughness of GDL is similarly adjusted with coating of 262 nm silica particles, PDMS, and 262 nm silica particles/PDMS composite as illustrated in Table 4.3. Surface roughness is also another important factor to the surface hydrophobicity.

Table 4:3: Measured surface roughness of GDLs' samples. Ra represents mean surface roughness based on arithmetical mean height; Rq, root mean square height, or standard deviation of the height distribution; and Rp, maximum peak height relative to the mean surface roughness.

Roughness	Non-coated GDL	Coated with 3.5wt % PDMS	Coated with 262 nm-silica Particle/PDMS
Ra (um)	18.336	16.683	17.738
Rq (um)	23.059	22.692	22.559
Rp (um)	76.656	60.529	62.370

In comparison to the non-coated GDL, the mean roughness (Ra) of both the GDLs coated with 3.5 wt. % PDMS and with 262 nm-silica particles/PDMS composite decreases. This perhaps is due to part of the original pores which have been covered by PDMS or by silica particles. The decreased root mean square height (Rq) of coated GDLs suggests that, their surface structures are more uniform than the non-coated ones. The relative higher maximum peak height (Rp) of composite coating than the PDMS coating probably is caused by the use of silica particles. In addition to the SEM results, it can be concluded that the 262 nm-silica particles/PDMS composite adjusts the surface uniformity of the GDL by building new structures, two-tiered micro-/nano-structures, which further assist low surface free energy material PDMS to attain the surface superhydrophobic property.

4.2.3 Stability of Silica Particles Coating on Gas Diffusion Layer

The stability of the silica particles coating on GDL is also investigated in the present work. The GDL coated with 262 nm silica particles is immersed in DI water and then put in a shaker. The shaking rate is set at 40 rpm and the temperature is controlled at 60 °C for 10 hours. The GDL samples are taken out periodically and dried until no weight change is observed. After that, θ is measured and plotted shown in Figure 4.22.

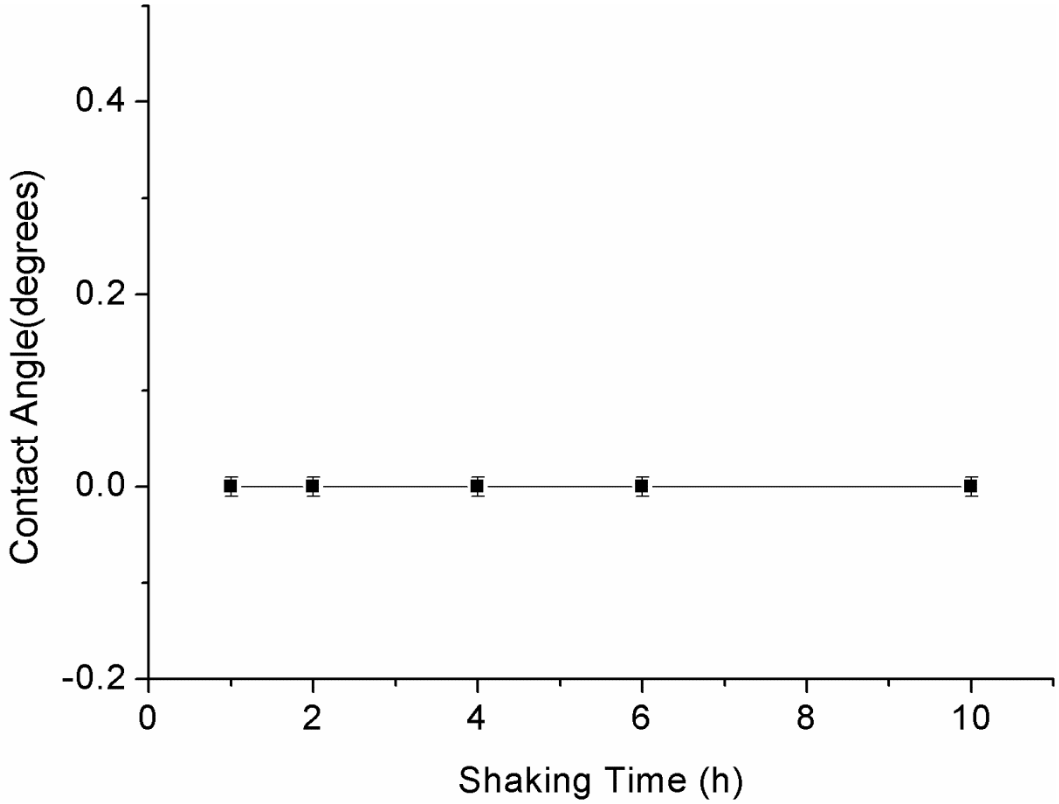

Figure 4.22: Stability tests for the gas diffusion layer coated 262 nm silica particles: shaking rate 40 rpm; temperature 60 °C.

It is seen that the 262 nm-silica particles shows a good stability on the GDLs. In 10 hour of testing, θ remains at 0° on the GDLs coated with 262 nm silica particles. Water can still easily wet the surfaces. The small size of these silica particles enables them to easily occupy the pores of GDLs. Since these silica particles have been heat treated on the GDLs, the dehydration of hydroxyl groups probably links most of the silica particles together. Additionally, water is ready to form a continuous film on these hydrophilic particles. However, the surface tension of water film may restrict the movement of these particles, and prevents them from moving in the real PEM fuel cell environment.

4.2.4 Composite Coated and Non-Coated GDLs Characteristics

4.2.4.1 Pore Size Distribution

The pore size distribution and the wettability of pores control the transport of liquid water and air transport in the GDL [105]. Non-coated GDL shows a relatively wide distribution with average pore radius of around (18 μm) as shown in Figure 4.23.

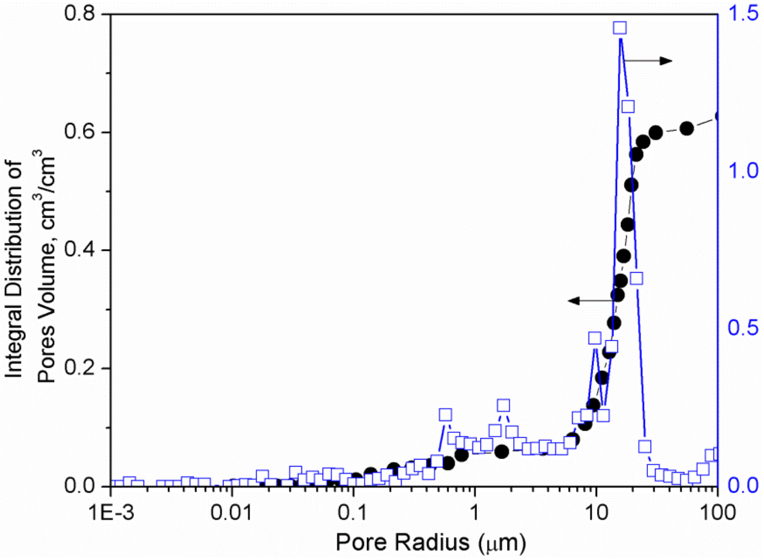

Figure 4.23: Pore size distribution of non-coated gas diffusion layer measured using Method of Standard Porosimetry (MSP).

The wide distribution indicates that the pores' sizes are non-uniform; hence this distribution represents the size of the pores which are formed through connection of randomly carbon fibers together with carbon powder to form the non-coated GDL. Further, the integral distribution shows that most of the of pores volume are above the 10 μm pore radius. While, the commercial GDL with MPL has more uniform pore size which is consist of two main groups: small pores of about 4.5 nm and large pores of about 11 μm as depicted in Figure 4.24. The sharp decrease of the integral pore volume at about 11 μm and at 4.5 nm pore radius indicates that the volume of the pores is distributed around the two radii values.

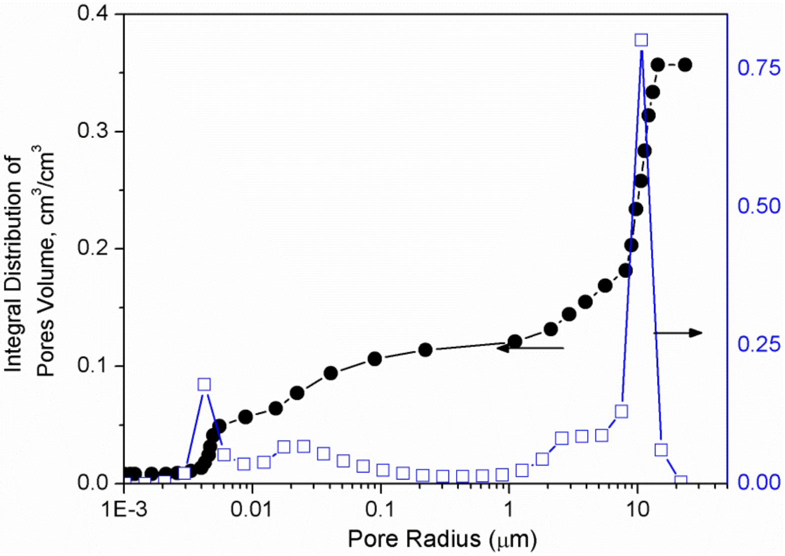

Figure 4.24: Pore size distribution of commercial gas diffusion layer loaded with micro porous layer (MPL) measured using MSP.

Small pores are generally from the MPL and account for the capillary-induced liquid flow, and since they are consist of PTFE and carbon powder mix, they are hydrophobic. Pasaogullari and Wang conducted one dimensional numerical analysis of the two-phase water transport in the cathode GDL with MPL [106]. They suggested that a highly hydrophobic MPL between the catalyst layer and GDL could enhance the liquid water removal. However, it is obvious that the application of MPL reduces the pore volume greatly, which may also reduce the gas transport from the channels to the reaction sites at the catalyst layer (CL).

Unlike the commercial GDL, 262 nm-silica particles coated GDL is a superhydrophilic GDL, hence, hydrophilic silica particles fill the pores of GDL so that liquid water can be easily distributed within the GDL pores. As shown in Figure 4.25. The small pores almost disappear with mainly large pores (about 5 μm). The pore size distribution is reduced significantly compared with the non-coated GDL. This can be attributed to the small size of silica particles, which enters into internal pores of the GDL and reduces their volumes.

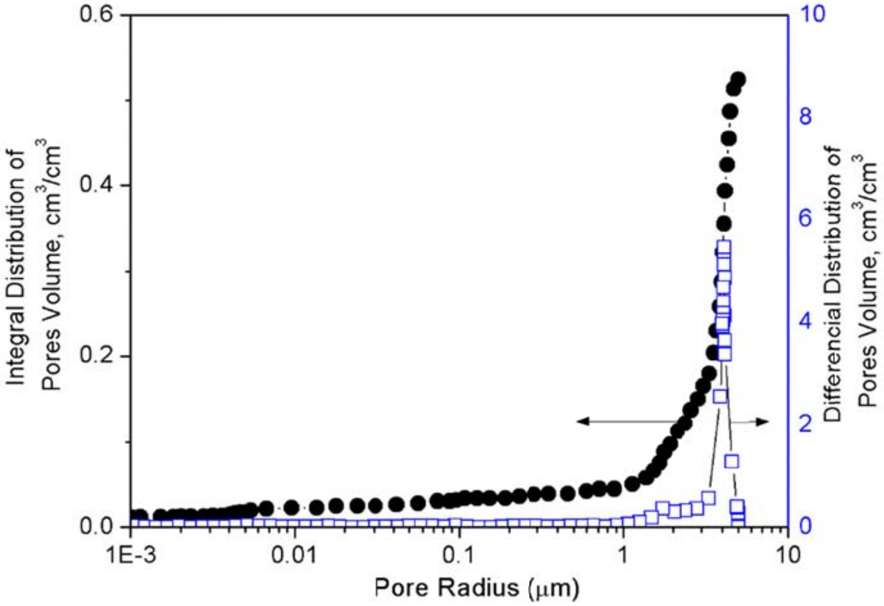

Figure 4.25: Pore size distribution of silica coated GDL measured using MSP.

Further, when the GDL is coated with 262 nm silica particles/PDMS composite, the pore size becomes more uniform and mainly large pores are presented (about 7.1μm). Although the pore volume decreases, but it is still in close range of that of large pore size of commercial GDL as shown in Figure 4.26.

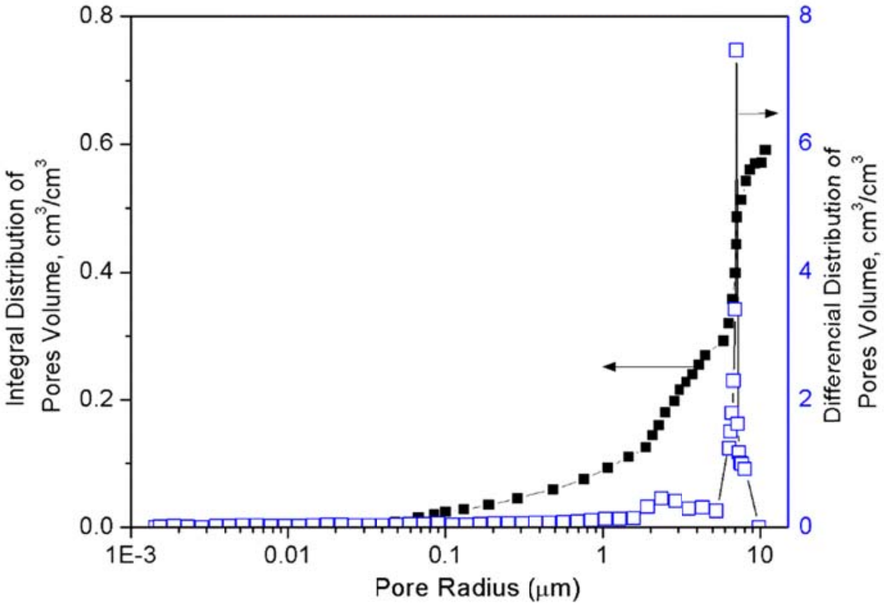

Figure 4.26: Pore size distribution of 262 nm silica particles/ PDMS composite coated GDL measured using MSP.

4.2.4.2 Capillary Pressure Distribution

The relationships between capillary pressure (P_c) and air saturation as a non-wetting phase are presented in Figure 4.27. In this case the non-wetting phase is air and the wetting phase is water.

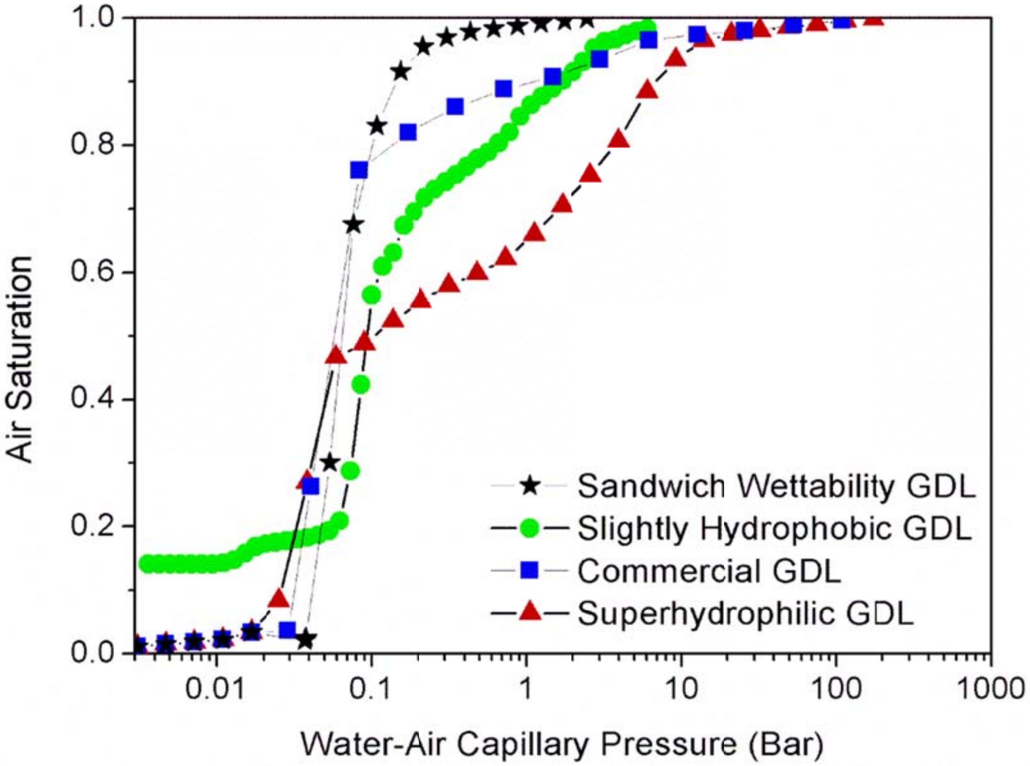

Figure 4.27: Comparison of the capillary pressure curves versus non-wetting phase saturation for; (★) sandwich wettability, (●) slightly hydrophobic, (▲) commercial, and (■) superhydrophilic coated gas diffusion layers.

The superhydrophobic coated GDL shows the lowest capillary pressure which is needed to reach full air saturation. This means that less capillary pressure is required to discharge the water out of the GDL structure. However, the rest of the GDL samples require higher capillary pressure to discharge the water out of the sample. This indicates that less water is entrapped inside the superhydrophobic coated GDL at the same P_c values. This is attributed to wettability of pores of the superhydrophobic GDL which are combined with hydrophilic and hydrophobic pores, which resulted from 262 nm silica particles and PDMS, respectively. Therefore, the surface of the GDL shows a superhydrophobic property (θ = 162 ± 2° and, α = 5 ± 3°) and the internal pores are hydrophilic as will be explained in the next section. This phenomenon helps the water to soak inside the GDL quickly and enhances the water discharge out of the GDL from the other side. Further, the hydrophobic pores on the surface of the GDL allow the water droplets which are generated at the reaction sites to roll down on the GDL fibers at the GDL surface and transport through GDL plane. This allows more air to be transported through the superhydrophobic coated GDL.

The commercial GDL shows a superhydrophobic properties at the surface (θ = 165±2° and, α = 2°). However, the existence of MPL increases the capillary pressure required to discharge water out of the GDL hence the capillary pressure is inversely proportional with pore radius as described in equation 3.3/ section 3.4.1. As the MPL pores' radii reduced to nano-meter size the capillary pressure increases even though the commercial GDL is coated with PTFE.

Non-coated GDL shows a higher capillary pressure required for fully air saturation. Further, the capillary pressure starts to gradually increase after 0.6 air saturation until it reaches to full air saturation. This is related to the water thin film which is formed on the non-coated GDL fibers surface due to high surface tension between the fibers and the water droplets and due to the water accumulation inside the pores. Therefore, the amount of transported air through the non-coated GDL is reduced. Further, since the capillary pressure starts to increase around 0.4 air saturation for superhydrophilic GDL. It shows higher capillary pressure required to discharge the water from the superhydrophilic GDL, This is related to existence of silica particles that increase the hydrophilicity of the GDL surface and pores inside the GDL. Thus, more locations are covered with water film on the GDL surface and more water is entrapped inside the superhydrophilic GDL pores due to the existence of silica particles which increases the surface tension of the superhydrophilic GDL fibers and pores.

4.2.4.3 Wetting Angle Distribution

Static contact angle (θ) measurements are useful for measuring the wettability of a fluid on a solid surface, but this approach can only be used on flat and smooth solid surface. For oil reservoirs it is possible to obtain a single crystal of the reservoir material for measurement that represents the internal pore surfaces in the real media [107]., GDLs are made of round fibers, thus obtaining a flat smooth sample on which that the static contact angle can be measured, is not possible. The contact angle on graphite material similar to the fibers material has been reported as 86° [12], but the water contact angle on carbon surfaces is known to be highly variable [108]. Further, GDLs are impregnated with a PTFE coating, so the internal surfaces of a GDL pores are a mixture of two types of surfaces of unknown wettability proportions. Lacking a solid, flat surface that is a representative of the internal GDL pores makes it hard to measure the contact angle through GDL, However, the only alternative for this is the measure the static contact angle of water droplet on the surface of the GDL as measured in this study. Various studies attempted to use contact angle as a qualitative indicator of GDL wettability and the effect of PTFE, however, they faced limited success [3, 109, 110]. Nevertheless, for the present work, it is necessary to obtain actual wetting angle distribution (θ_w) to compare between different coated samples.

Method of standard porosimetry (MSP) allows measurements of wetting angle distribution within the broad range of θ_w from 0° to 90°. For this purpose the GDL samples are measured with both; DI water whose wetting angle should be determined and the standard liquid whose wetting angle is known (octane $\theta_w \sim 0^o$). However, one drawback of MSP is that, when a porous material with an insufficient rigid structure is soaked with a wetting liquid, a volume increase (swelling) under the influence of the liquid's capillary pressure is possible. If such a material is used in a liquid medium it is important to know its porous structure just in this medium. The process of swelling depends on the nature of the liquid. In absence of a specific interaction between the porous material and the liquid, the capillary pressure is proportional to the surface tension of the liquid. In this study the integral pore volume is increased when the water is used as a wetting liquid due to water swelling by carbon fibers. Thus it is impossible to measure θ_w through a complete radii range distribution, but at least where the majority of the pores' radii are distributed as shown in Figure 4.28.

As illustrated in Figure 4.28 a, the wetting angle distribution of the pores for the non-coated GDL is distributed from 0°-75° for the larger pores. This results in water entrapment and blockage inside the hydrophilic pores, causing reduction in the amount of transported air to the reaction sites from the gas flow channels and the amount of water from the reaction sites to the gas flow channels. This will consequently reduces cell performance. Meanwhile, the commercial GDL which is coated with 30 wt. % PTFE shows that small pores, all have a 90° contact angle which is higher than the non-coated GDL. This helps more air to be transported to the reaction sites and more water to be discharged from the reaction sites as shown in Figure 4.28 b. On the other hand, small pores size of the MPL layer on the commercial GDL plays an opposite effect in reducing the amount of transported air especially at high current density, as discussed earlier.

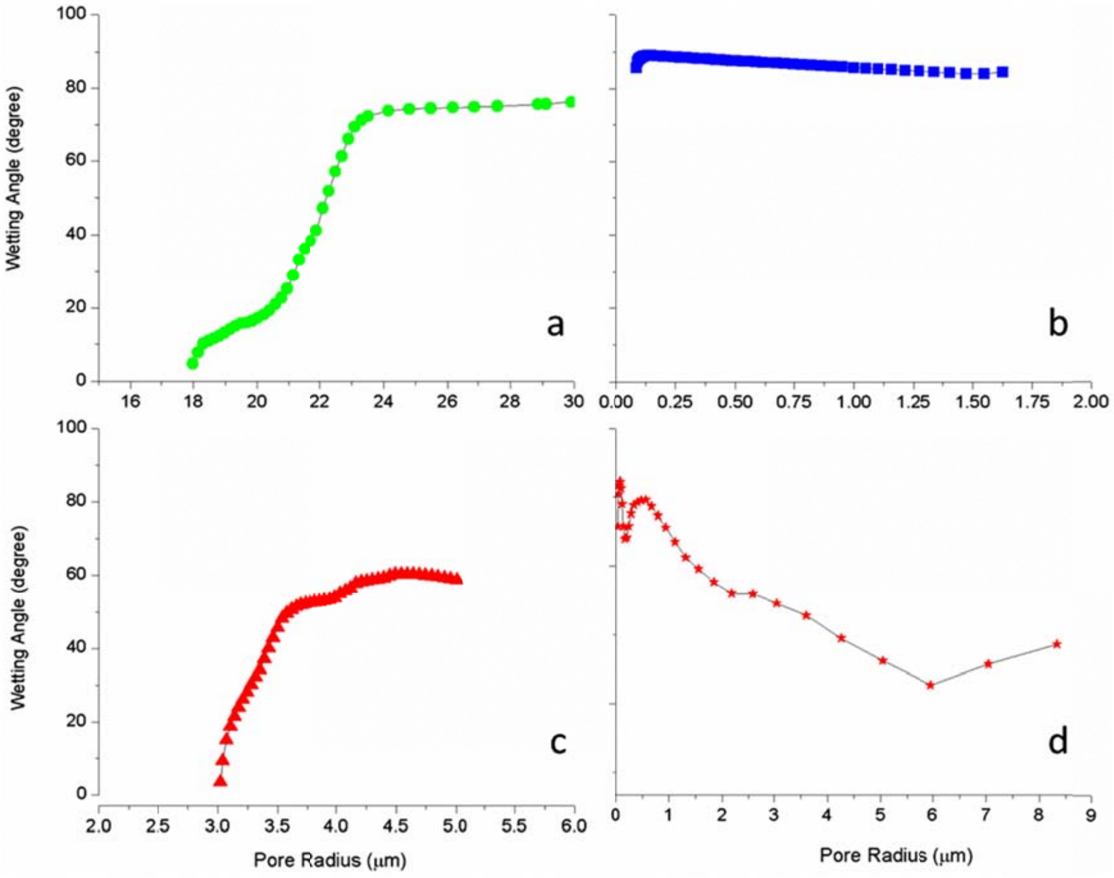

Figure 4.28: Measured wetting angle vs. pore radius using MSP for; a) Non-coated, b) Commercial, c) 262 nm silica particles coated, and d) 262 nm silica particles/PDMS composite coated GDL.

Compared with the non-coated and the commercial GDL, the 262 nm silica coated GDL shows lower wetting angle which are distributed between 0°- 60° for the small and the medium pore size of the 262 nm silica coated GDL (superhydrophilic). This can be seen in Figure 4.28 c. This wetting angle distribution indicates that the silica particles which have a hydrophilic nature, as mentioned earlier, have filled most of the pores and made them more hydrophilic compared to the non-coated GDL. This may lead to more water entrapment inside superhydrophilic GDL, thus can reduce the amount of transported air and water significantly to and from the reaction sites, respectively, resulting a significant degradation of the cell performance.

Unlike the non-coated, commercial, and 262 nm silica particles coated GDLs. The 262 nm silica particles/PDMS composite coated GDL (superhydrophobic) shows a different distribution for the wetting angle of the pores from 20° - 90°. The small pores have high wetting angle which is decreased by increase in the pore radius as shown in the Figure 4.28 d. This ensures the existence of hydrophobic and hydrophilic pores combinations. The hydrophilic pores are resulted from silica particles and the hydrophobic ones are caused from PDMS material. The hydrophilic pores are responsible for distribution of the water inside the GDL and the hydrophobic ones provide a transport media for air and water, to and from the reaction sites, respectively. Further, the high static contact angle on the superhydrophobic surface ($\theta = 162 \pm 2°$) indicates that most of the hydrophobic pores are close to the surface of the GDL and the hydrophilic pores are in the internal region. This combination results in sandwich wettability GDL, which has a superhydrophobic surfaces and hydrophilic internal pores. A water droplet (10 µl) can roll off the tilted surface with the tilted angle of 5°, but it can also be drawn into the plane of the GDL in 10 min due to the internal hydrophilic pores which have high surface tension to attract the water inside the GDL. This kind of structure can help water transport through the GDL. Additionally, the macro pores left in the GDL will probably offer low resistance for the gas transport. This design of GDL is very unique from that of commercial GDL with MPL; the hydrophilic internal pores within the sandwich wettability GDL offer a driving mechanism for the distribution of water; remained macro pores within the GDL also ensure the transport of air. Compared with the PEM fuel cell assembled with commercial cathode GDL, the PEM fuel cell assembled with sandwich wettability cathode GDL shows a better performance as will be discussed in the next section.

4.2.5 Effect of Composite Coated Cathode GDL on Overall PEM Fuel Cell Performance

PEM fuel cell performance measurement (polarization curve, I-V) is one of the most common used experimental presentation techniques in understanding the effect of different surface wettability of the cathode GDL on the nature of water removal in an operating PEM fuel cell with 100 cm^2 active area. In the present work, the performance tests are conducted with four different cathode GDLs of: 1) non-coated GDL (slightly hydrophobic), 2) GDL coated with 262 nm silica particles (superhydrophilic), 3) GDL coated with 262 nm silica particles/PDMS composite (sandwich wettability), and 4) commercial GDL loaded with MPL (superhydrophobic). The polarization curves are generated under identical operating conditions as shown in Figure 4.29.

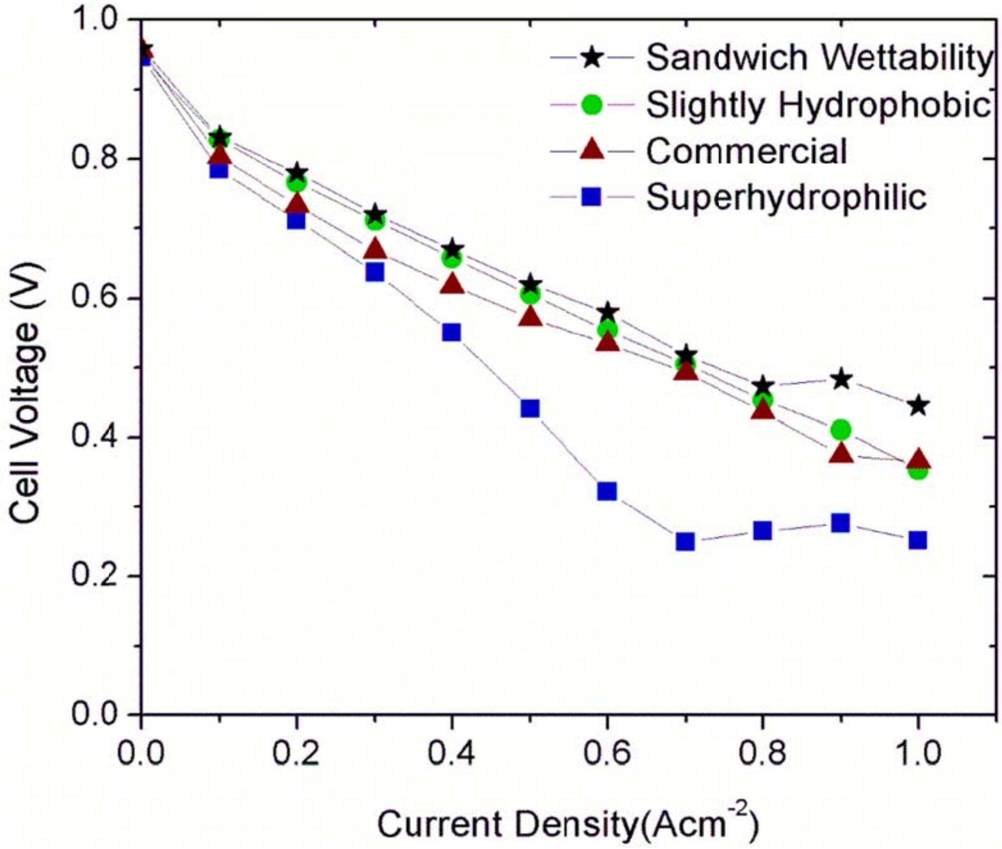

Figure 4.29: Experimentally measured PEM fuel cells performances curves comparisons with different cathode GDLs; (★) sandwich wettability, (●) slightly hydrophobic, (▲) commercial, and (■) superhydrophilic coated GDL. Cell operating conditions: anode and cathode back pressure is 1atm, cell temperature of 65 °C, stoichiometric ratio 2 for the cathode air stream and 1.2 for the anode hydrogen stream, fully humidified for both cathode and anode gas streams.

It is noticed that the sandwich wettability cathode GDL has the best performance, particularly under high current densities of 0.6-1.0A/cm^2. Due to the modified wettability of surface and internal pores, as well as the modified internal pore size, gas/water transport through GDL is improved accordingly. The hydrophilic pores help water to randomly distribute in the GDL, while the superhydrophobic surface facilitates water droplet o detach from the surface. An important observation with composite coated GDL is that on its tilted surface (tilted angle 5°); a 10 μl of water droplet could roll off easily. However, on a horizontal surface this water droplet could also distribute gradually in 10 minutes. This kind of sandwich wettability likely assists the water transport through the GDL. Aside from the wettability, silica particles/PDMS composite coating does not affect the pore size in GDL as compared with the commercial GDL. In other words, the pores size (about 7.1μm) maintains sufficient gas permeability and enhances the cell performance especially at high current densities. In the case of PEM fuel cell with commercial GDL, its performance is even lower than non-coated GDL. It is probably due to the cracks in the MPL, which reduce the capillary force through the micro-pores and weaken the transport of water through the GDL. However, at higher current densities the commercial GDL shows better performance than the non-coated GDL.

The superhydrophilic GDL coated with silica particles lowers the cell performance. Although the produced water could quickly distribute in the GDL, it is noticed that the droplet resists detaching from the GDL surface by air stream due to the high surface tension. In addition to that, a thin water film forms on the hydrophilic GDL surface, requires high shear force to be removed. This blocks the pores in the GDL resulting in reducing the gas permeability. Further, the accumulated water inside the GDL reduces the reaction rate in the catalyst layer, resulting in cell performance degradation. Additionally, the existence of the droplets on the GDL surfaces increases the pressure drop in the gas flow channels, impacting the PEM fuel cell performance negatively.

4.3 Effect of Through Plane GDL Wettability Gradient on Its Characteristics, Water Removal Rate, and Overall PEM Fuel Cell Performance

In this section the effect of employing one side hydrophobic GDL will be investigated. The reason for studying the one side hydrophobic GDL separately from the composite coated GDL is that; the composite coated GDL section discusses new coating materials and compares them with the current commercial ones. However, this section studies the effect of

PTFE coating which was used before as a coating material by other studies as discussed in the literature review in chapter 2, section 2.2. In this study, on the other hand, GDL is coated with PTFE from one side only, and it is not coated uniformly from the two sides by immersing the GDL in PTFE solution as demonstrated in previous studies. Further, coating the GDL with PTFE from one side reduces the amount of PTFE required to coat the GDL which ultimately decreases the cost of coated GDL. Hence, less PTFE material and less time are required to coat one surface of the GDL.

4.3.1 Effect of PTFE Coating on One Side of GDL on its Wettability

As mentioned earlier, the surface wettability of the GDL is determined by measuring the static contact angle (θ) of water droplet on the GDL surface as shown in Table 4.4.

Table 4:4: Static contact angle measurements (θ) of the GDL samples on each side

	Non-coated GDL		Commercial GDL		One Side Hydrophobic GDL	
	Side1	Side2	Side1	Side2	Side1	Side2
wt. %PTFE	0	0	30	30	15	0
θ	107±2°	107±2°	165±2°	165±2°	147±3°	133±3°

The term one side hydrophobic GDL refers to the coating process, since the GDL is coated with PTFE on one side of the GDL. The coated surface shows higher static contact angle than the non-coated one and lower than the commercial GDL. However, the non-coated and commercial GDLs show the same static contact angle on both sides of each one as illustrated in Table 4.4.

The difference in the static contact angle between the two surfaces indicates that there is a wettability gradient through GDL plane. The nature of carbon fibers which soaks the PTFE solution on the coated surface into GDL plane direction might distributes the amount of PTFE solution through the GDL plane. Whereas the highest amount is close to the coated surface of GDL and the lowest amount is close to the non-coated surface of the same GDL as illustrated in Figure 4.30.

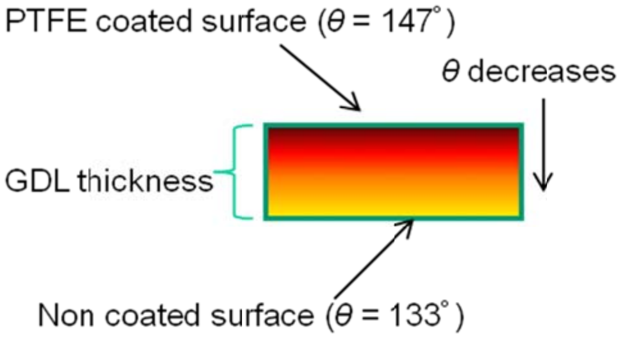

Figure 4.30: Schematic of the one side hydrophobic GDL.

4.3.2 One side Hydrophobic and Non-Coated GDLs Characteristics

4.3.2.1 Pore Size Distribution

In the pore size distribution tests, octane is considered as the wetting fluid and air is considered as the non-wetting fluid. This is because, octane is a highly wetting fluid and its contact angle is close to 0° as discussed earlier. This will guarantee filling of the hydrophobic and hydrophilic pores as illustrated in Figure 4.31.

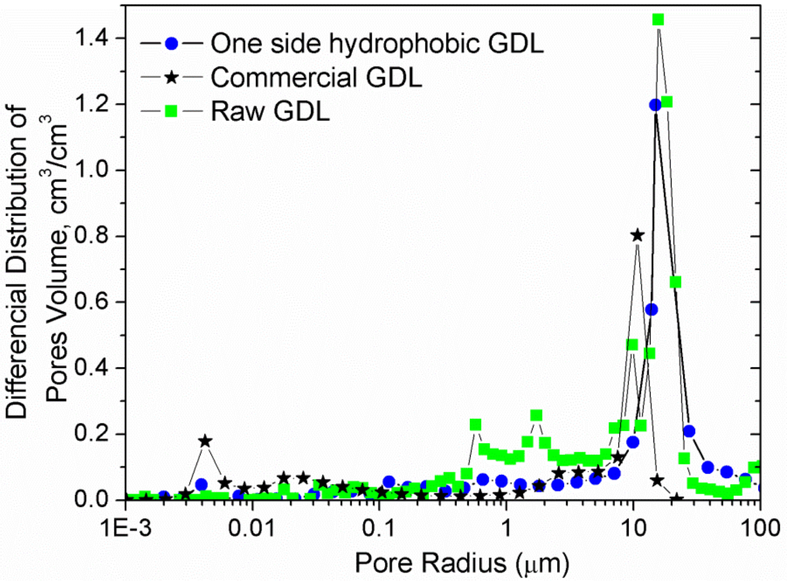

Figure 4.31: Pore radius differential distribution for the (●) one side hydrophobic, (■) raw, and (*) commercial GDLs.

The non-coated GDL shows larger pore radius distribution. The pore radius distribution represents the hydrophilic pores, hence non-coated GDL has 0% PTFE. Meanwhile the one side hydrophobic GDL shows smaller pore radius distribution as shown in Figure 4.31, which represents the hydrophilic and hydrophobic pores. This can be attributed to coating of PTFE emulsion, which reduces the size of the pores on the coated surface. The one side hydrophobic GDL shows a distribution peak of around 15 μm; meanwhile the non-coated GDL shows around 18 μm for its distribution value. Furthermore, non-coated GDL shows higher volumetric porosity than the one side hydrophobic GDL; these values are 0.77 and 0.74, respectively. On the other hand, one side hydrophobic GDL shows larger pores' radii than the commercial GDL which discussed in previous sections.

4.3.2.2 Effect of One Side Hydrophobic GDL on Capillary Pressure Distribution

As noticed in Figure 4.32, air saturation raised by increasing the capillary pressure (P_c) for the non-coated and one side hydrophobic GDL. This can be attributed to the continuous water drainage from the GDL pores, while the air penetration into the GDL pores. The one side hydrophobic GDL shows higher air saturation at the same capillary pressure values, in compare with the non-coated and commercial GDLs. This interprets that, less water is entrapped inside the one side hydrophobic GDL. This agrees with the concept of hydrophobic pore network, which suggests that water is spontaneously ejected out of the hydrophobic pore network and simultaneously, air is entering into the GDL sample.

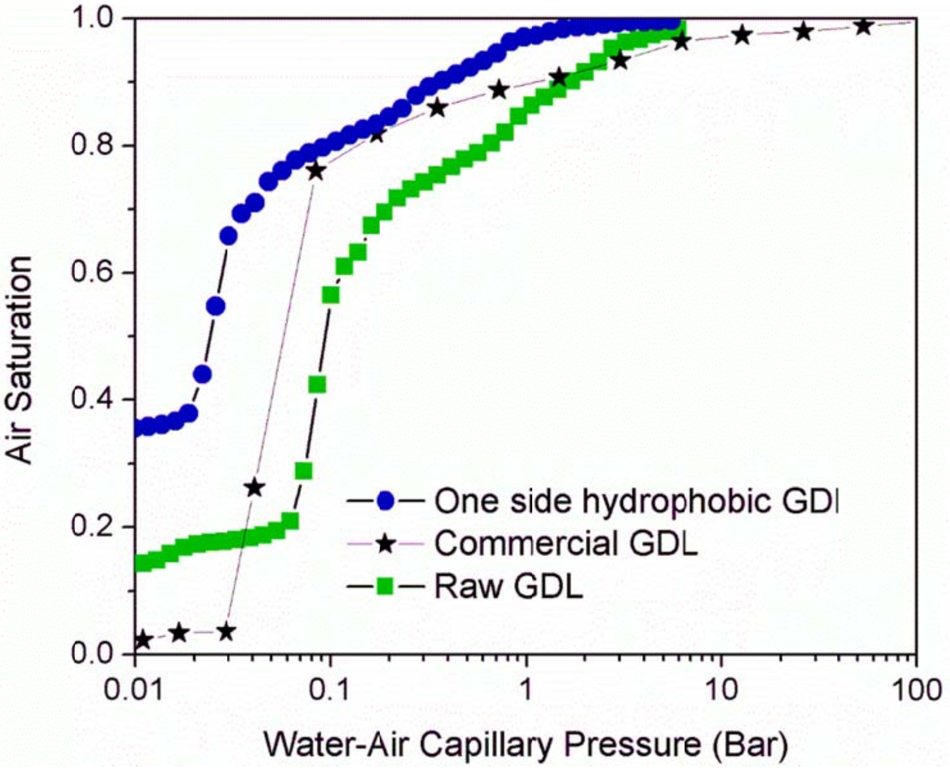

Figure 4.32: Measured capillary pressure vs. non-wetting phase saturation for (●) one side hydrophobic, (*) commercial, and (■) raw GDL.

The one side hydrophobic GDL shows higher amount of air saturation than the non-coated and the commercial GDL at (P_c≈0). This is attributed to the wettability gradient through GDL plane, resulting in forcing the water droplets to migrate to the neighboring pores and then out of GDL. Furthermore, the sharp increment of air saturation in the one side hydrophobic GDL starts around 0.02 bars, meanwhile it starts around 0.08 and 0.04 bars for the non-coated and the commercial GDL, respectively as depicted in Figure 4.32. This means that, the capillary pressure required to start the water drainage out of the GDL, is four times higher in non-coated GDL and two times higher in the commercial GDL. This confirms that the water removal rate for the one side hydrophobic GDL is higher than the non-coated and commercial ones, resulting in superior air penetration rate and consequently better air transportation inside the one side hydrophobic GDL. Further, the wettability gradient through one side hydrophobic GDL plane enhances the transport of the water due to driving capillary force through GDL plane, as wetting phase (W) moves from hydrophobic pores to higher hydrophobic ones. This will reduce the amount of capillary pressure required for the wetting phase (P_W) to transport through GDL, and for the air as a non-wetting phase (NW) to replace the wetting phase. Therefore capillary pressure decreases, hence;

$$P_c = P_{NW} - P_W \tag{4.1}$$

Non-coated GDL shows higher capillary pressure values at the same saturation levels or level. This might be attributed to the high volume of the hydrophilic pore networks inside the GDL. These networks allow the wetting phase (water) to be absorbed by carbon fiber matrix, resulting in blocking the pores on the GDL surface with thin films of water. This will reduce the amount of air penetration into the GDL, leading poor water removal rate and poor air to transport inside the GDL pores. Further, raw GDL has uniform wettability gradient through GDL plane since the contact angle on both sides of the GDL are the same resulting in uniform capillary force distribution through GDL plane and thus slower water transport.

Although the commercial GDL is highly hydrophobic, but the wettability gradient effect might not exist as seen in the one side hydrophobic GDL. This refers to the value of the measured static contact angle on both sides of the commercial GDL (165 ± 2°) as illustrated in Table 4.4. Further, the amount of capillary pressure required to reach to full air saturation for the commercial GDL is around 100 Bars. In contrast, the capillary pressure required for non-coated and the one side hydrophobic GDL to reach full air saturation is almost 7 Bars.

This is attributed to small pores size distribution (nano meter scale) of the MPL of the commercial GDL.

4.3.2.3 Effect of One Side Hydrophobic GDL on Wetting Angle Distribution

As mentioned earlier, the wetting angle distribution is used in this study to compare the wettability of the GDL pores based on cumulative pore volume distribution. The wetting angle distribution of the pores for the non-coated GDL is distributed from 0°-75° for the larger pores as described in Figure 4.33 a. This results in water entrapment and blockage inside the hydrophilic pores. This reduces the amount of the transported air to the reaction sites from the gas flow channels, and the amount of water from the reaction sites to the gas flow channels. Consequently the cell performance will be degraded. However, the one side hydrophobic GDL shows that small pores are more hydrophobic than the larger ones. As seen in Figure 4.33 b, the contact angle decreased from 90° as the pore size increased. This is attributed to coating of one side of the GDL with PTFE. The coated side pores will be filled with PTFE solution as a hydrophobic material, thus the small pores shows higher wetting angle.

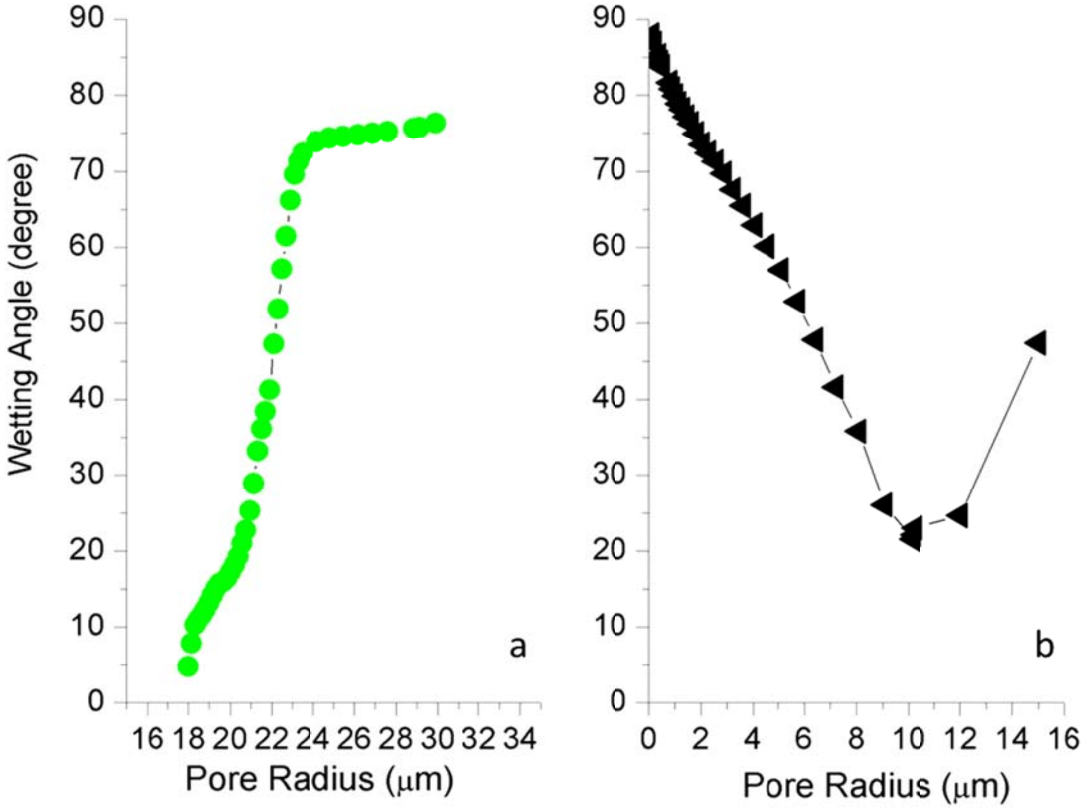

Figure 4.33: Measured wetting angle using MSP for; a) non-coated, and b) one side hydrophobic GDLs.

While moving away from the coated surface through GDL plane direction, the amount of PTFE in the pores is reduced. Due to this, the pores size increases and the wetting angle is decreased until it reaches 20° at 11 μm pore radius as shown in Figure 4.33 b. beyond 11 μm the wetting angle starts to increase. This suggests/confirms that a small amount of PTFE is reached to the other side of the GDL; hence the largest pores exist on the farthest point of the coated surface, which is the non-coated surface for the same GDL. Thus the static contact angle on the non-coated surface (i.e. 133±3°) is higher than the static contact angle on the non-coated GDL (i.e.107±2°). The difference between contact angles on the two sides of the one side hydrophobic GDL as illustrated in Table 4.4, leads to wettability gradient between the two sides of the GDL. This gradient has the lowest surface tension on the coated surface and the highest one on the non-coated surface. In addition, this gradient can create a driving force to move the water droplets from the low surface tension region (coated side) to the higher one (non-coated side) of the one side hydrophobic GDL. Meanwhile, this gradient does not exist in the non-coated and commercial GDLs.

Further, the one side hydrophobic GDL shows the wetting angle distribution in range of 20° to 90°, which is higher than the non-coated GDL (0^{o} to 75^{o}) and lower than the commercial GDL (90°) as shown in Figure 4.28 b. This might reduce the amount of water entrapped inside the one side hydrophobic GDL, thus more air is transported inside the GDL from the channels to the reaction sites and consequently the cell performance is improved; hence, the small pores' radii of the MPL considered as an obstacles for water air transport through GDL at high current density as formerly discussed.

4.3.3 Effect of Wettability Gradient on Water Removal Rate

Water removal rate denotes to the amount of water transports through the GDL plane at a certain time. The amount of water transferred through the commercial GDL is almost (0 ml/s), so this is not included with the other samples as presented in Figure 4.34. This is related to the very small pores of the MPL on the commercial GDL which prevents the discharging of water from the syringe under the same experimental conditions. On the other hand, one side hydrophobic GDL shows the highest water removal rate, when the coated side faces water in the syringe barrel. In contrary, the lowest water removal rate is observed, when the non-coated side of the same GDL faces water in the syringe barrel, as seen in Figure 4.34. This is attributed to the driving capillary force through GDL plane from low wettable side to higher wettable one of the GDL. On the other hand when the GDL's non-coated surface faces the water inside the syringe barrel. The water removal is decreased significantly, since the water moves in the opposite direction of the driving capillary force, resulting in reducing water transport velocity through GDL plane and consequently water removal rate is reduced.

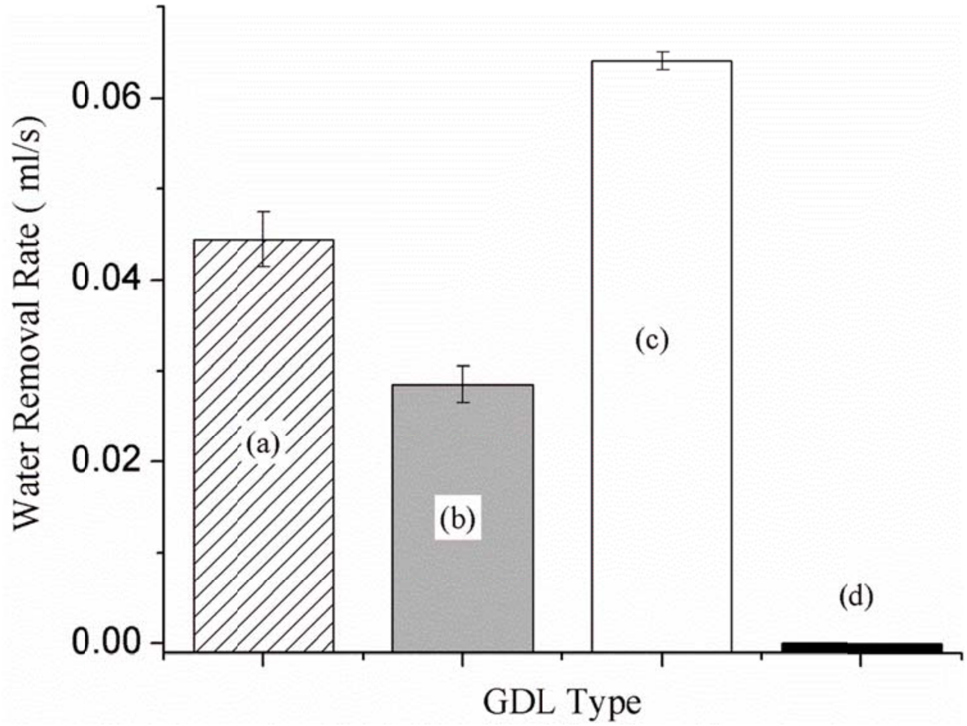

Figure 4.34: Water removal rate for; (a) non-coated GDL, (b) coated side faces water inside the barrel (c) non-coated side faces water inside the barrel, and (d) commercial GDL.

Although non-coated GDL has 0 wt. % PTFE content, but it has higher water removal rate than the one side hydrophobic GDL while the non-coated side faces the water in the syringe barrel. This can be seen in Figure 4.34. This can be attributed to the uniform capillary force gradient through the non-coated GDL plane. Meanwhile, with regard to the one side hydrophobic GDL, while the non-coated side faces water in the syringe barrel, water moves with the gravity direction but opposite to the driving capillary force direction. This results in lowering water removal rate than in the non-coated GDL which has a uniform through plane driving capillary force. Whereas, when the coated side is facing the water in the syringe barrel, the driving capillary force and the gravity are in the same direction, resulting in increasing the speed of water transport through GDL plane, resulting in higher water removal rate than the other two samples.

4.3.4 Effect of Wettability Gradient on Water Droplet Dynamics

The maximum diameter of droplet emerged from the non-coated GDL is about 5.83 ± 0.7 mm as seen in Figure 4.35 a. As to the one side hydrophobic GDL with the coated and non-coated side facing to water, the maximum diameter of water droplet is about 4.5 ± 0.5 mm as depicted in Figure 4.35 b, and c. This is attributed to the pores size of the GDL samples. One side hydrophobic GDL has smaller mean pore size diameter due to coating with PTFE emulsion. Further, smaller size droplet is easy to be detached from the GDL surface since it has a smaller contact area with the GDL surface.

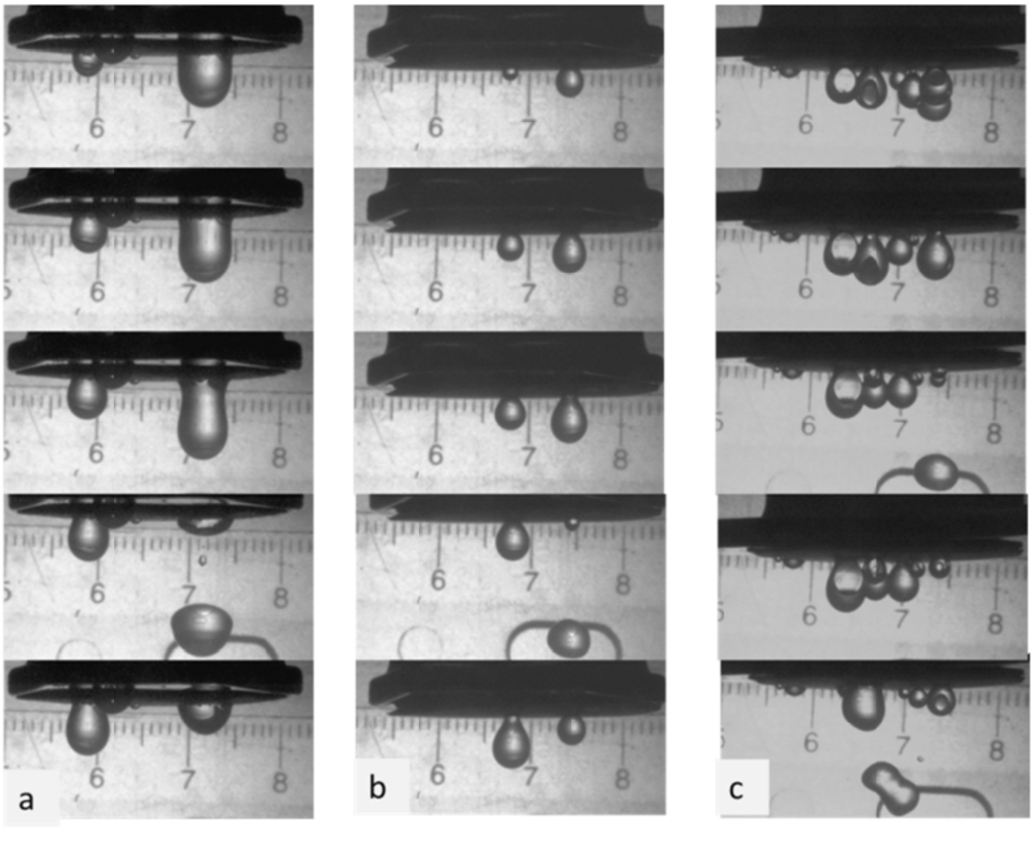

Figure 4.35: Droplet dynamics and size imaged with 200 ms. time interval between each image: a) non-coated GDL, one side hydrophobic GDL whereas; b) non-coated side faces water in the barrel, and c) coated side faces water in the syringe barrel.

As shown in Figure 4.35 a, b, and c, the water emerged from the surface of the non-coated GDL, non-coated side faces water, and coated side faces water for the one side hydrophobic GDL samples in preferential locations corresponds to the lowest resistant paths to water transport [111]. These locations are referred as the break through locations [57, 112]. The number of break through locations of water droplets for the one side hydrophobic GDL surface are increased significantly, when the coated surface faces water in the syringe barrel than the other samples as shown in Figure 4.35 c. This increment is caused by driving capillary force through GDL plane, which increases the number of paths with the lowest resistance of water transport. Hence the droplets move toward the low capillary pressure side to the high capillary pressure side when the coated side faces the water in the syringe barrel. Furthermore, break through locations in the three samples are observed as dynamic processes hence these locations are changed over time. This phenomena is recognized by an ex-situ observation of Lister *et al.* [51] and the recent in-situ measurements of Manke *et al.* [113] who referred this phenomena as an *eruptive transport*.

Droplets emerged from the non-coated GDL surface have an elongated shape and their contact angle with the GDL surface is almost 100° as seen in Figure 4.36 a. This is attributed to the hydrophilic nature of the carbon fibers of the non-coated GDL and to the large pores size.

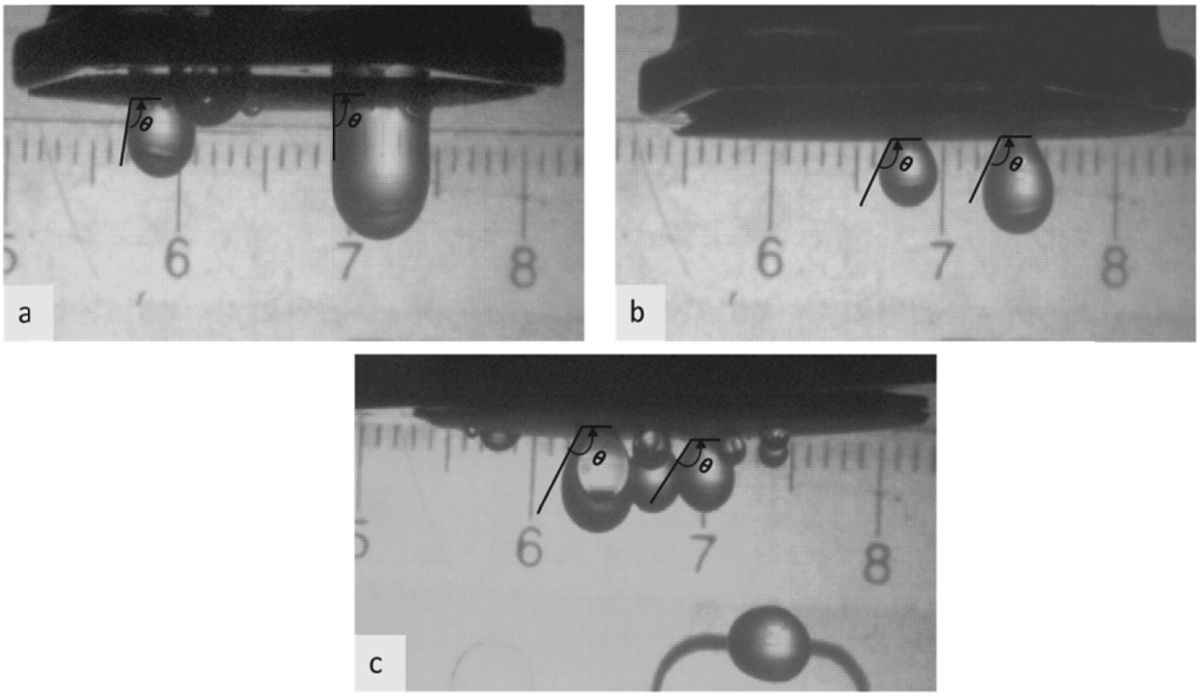

Figure 4.36: Droplet emerged from; a) non-coated GDL, b) non-coated side faces water in the barrel, and c) coated side faces water in the barrel for the one side hydrophobic GDL.

Meanwhile, the one side hydrophobic GDL shows higher contact angle than the non-coated GDL, and droplets have a spherical shape as shown in Figure 4.36 b, and c. This can be attributed to the hydrophobic fibers and to the smaller pore size distribution.

4.3.5 Effect of Wettability Gradient on the Overall PEM Fuel Cell Performance

As seen in Figure 4.36, the one side hydrophobic GDL shows highest cell performance when the coated side faces the catalyst layer (CL). On the other hand, the lowest performance is noticed for the same GDL when the non-coated side faces the CL for the same GDL. Meanwhile, the non-coated and commercial GDLs cell performances are in between the aforementioned two performance curves. This is suggests/implies that the water removal rate of the three samples from the highest to the lowest; when the coated side of the one side hydrophobic GDL faces the water side in the syringe barrel, non-coated, and when the non-coated side faces the water side in the syringe barrel GDL samples, respectively as mentioned earlier. This assures that not only PTFE coating can improve the water and gas transport inside GDL, but also the creation of driving capillary force through GDL plane in specific direction has a significant impact on water removal at high current densities. Further, the upright position of the GDL in the tested PEM fuel cell installed in the FCATS-S800 reduces or eliminates the gravity effects on water removal as shown in Figure 3.19. The differences in performance started clearly at 0.7 Acm^{-2} where the effect of oxygen diffusion limitation is due to water blockage of the GDL pores starts (concentration over potential) [35, 114-119] as depicted in Figure 4.37.

The maximum power density is developed from 0.41 to 0.46 Wcm^{-2} for 40 cm^{2} cell. This is caused by higher rate of water removal from the GDL which increases the value of diffused oxygen from the gas flow channels through GDL to the reaction sites at higher current densities. However, when the non-coated side is facing the CL water transport from the CL through GDL to the channel slowly due to the driving capillary force direction which is opposite to the water transport direction, resulting in GDL flooding and rapid voltage decay as shown in Figure 4.37. Alternatively, the cell loaded with the commercial GDL shows the best performance at low current density region. This is assigned to the low contact resistance of the MPL layer. However, as the amount of water generated increases at high current density, the commercial GDL water removal decreases. This can be explained by MPL pores small size, which leads to the CL and GDL flooding, thus the amount of air transferred to the reaction sites at the CL is reduced and consequently the cell performance is degraded.

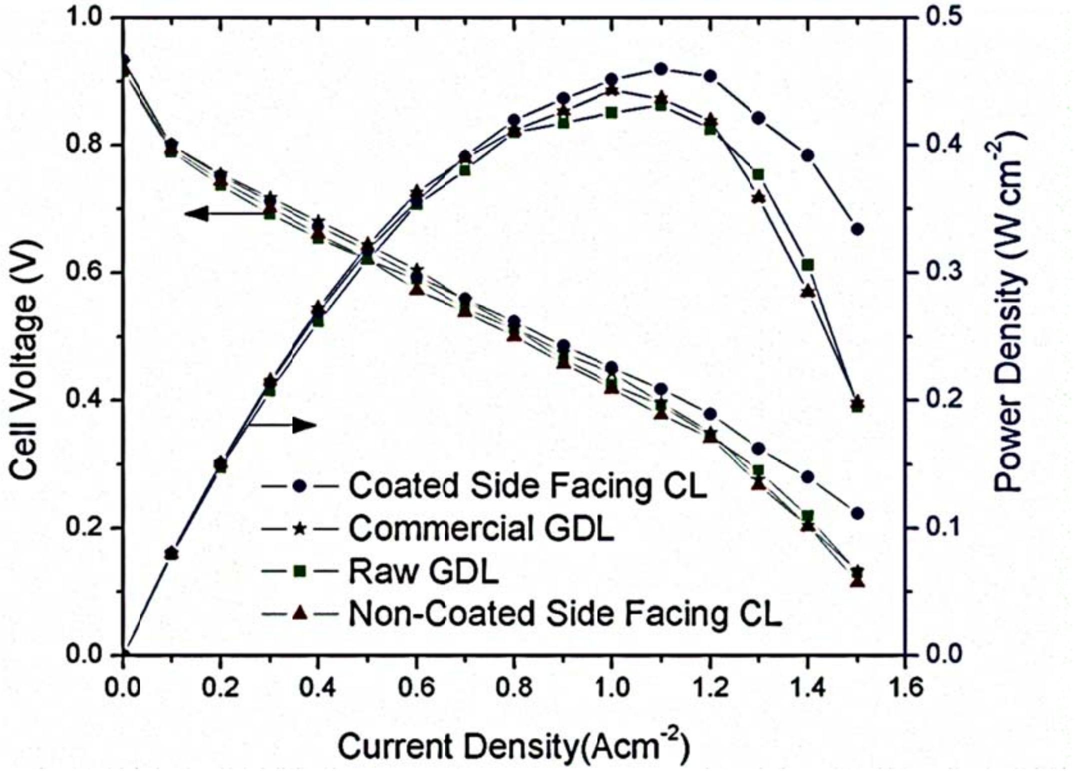

Figure 4.37: Comparison of PEM fuel cells performances for; (●) coated side faces the CL, (*) commercial GDL, (■) raw GDL, and (▲) non-coated side faces the CL for the one side hydrophobic GDL. PEM fuel cell operating conditions: cathode and anode back pressure is atmospheric pressure; cell temperature of 65 °C; stoichiometric ratio 2 for the cathode air stream and 1.2 for the anode hydrogen stream; fully humidified for both cathode and anode gas streams.

It can be said that, non-coated and commercial GDLs show better performance than one side hydrophobic GDL when the non-coated side faces the CL. This is related to the driving capillary force through plane the one side hydrophobic GDL; whereas the non-coated and commercial GDLs might have a uniform capillary force through their planes.

The effect of wettability gradient through GDL plane shows a small improvement in the cell performance compared with the commercial and raw GDL. This is due the small size of the cell (40 cm^2). However, this difference might be more significant in the larger cell size, because of the amount of generated water at the cathode side in the large cell is higher as mentioned earlier.

Even though the difference in the cell performances curves show a small difference, but these data shows at least 95% confidence limit in the measured data. This limit is based on the uncertainty associated with the standard deviations of the measured voltage values at a fixed current density as shown in Figure 4.38a. The measured voltage data has higher fluctuations when the non-coated side of the one side hydrophobic GDL is facing the CL. This refers to the low water removal rate from the cathode GDL to the gas flow channels, because the water moves through GDL plane opposite to the diving capillary force direction.

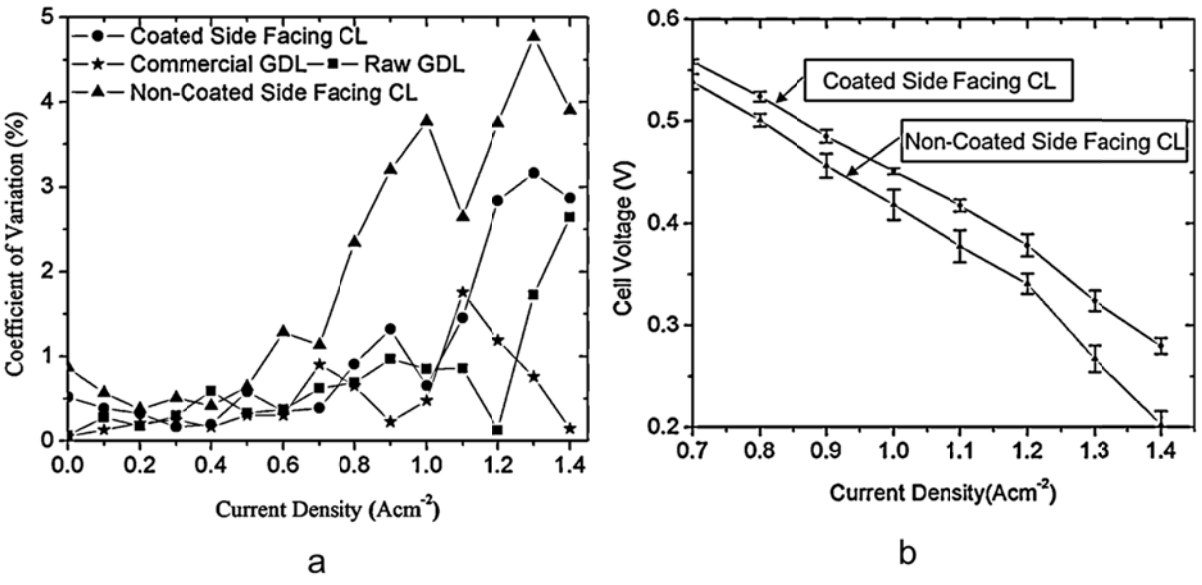

Figure 4.38: Uncertainty of the measured voltage: a) Coefficient of variation of the measured voltage for the three different cathode GDL in PEM fuel cells ;(●) coated side faces the catalyst layer, (*) commercial GDL, (■) Raw GDL, and (▲) non-coated side faces the catalyst layer for the one side hydrophobic GDL, and b) Highest and lowest PEM fuel cell performances from 0.7 A.cm^{-2} to 1.4 A.cm^{-2} showing the error bars at each measured voltage (the symbol size of the measured voltage is minimized to show error bars clearly).

As seen in Figure 4.38 b, the wettability gradient through GDL plan shows significant improvements in the cell performance when the coated side facing CL compared with the non-coated side facing CL cathode GDLs in the PEM fuel cell. This signifies the effect of wettability gradient through GDL plan and its role in better water management when the water moves with the direction of the driving capillary force through GDL plane. Further, the error bars for the non-coated side facing CL cell performance is higher. This refers to higher amount of accumulated water in the cathode GDL which leads in higher fluctuations of the measured voltages. It is worth mentioning that, Figure 4.38 b shows the error bars of the highest and the lowest cell performances. Meanwhile, the cell performances in between are not plotted, because this makes the figure very crowded and it is hard to distinguish between the curves.

Chapter 5

Summary and Future Work

5.1 Summary and Original contribution

The major accomplishments and contributions achieved in the present study can be summarized as follows;

I. Three different surface wettability conditions have been introduced on raw graphite surface (slightly hydrophobic) and characterized using scanning electron microscopy (SEM), Profilometry, sliding angle (α), and static contact angle (θ) measurements; 262 nm silica particles/ Polydimethylsiloxane (PDMS) composite (superhydrophobic), Polytetrafluoroethylene (PTFE) (hydrophobic), and 262 nm silica particles (superhydrophilic) coated graphite.
    i. The superhydrophobic surface has shown the lowest sliding angle (α = 19±1°) and the highest static contact angle (θ = 155±2°), and lowest measured roughness (Ra = 2.85µm).
    ii. Superhydrophobic surface shows a good stability under PEM fuel cell environment

II. An ex-situ experimental study of the effect of superhydrophilic, slightly hydrophobic, hydrophobic, superhydrophobic and combined surface wettability channels on the two-phase flow dynamics and pressure drop have been conducted. Further, the effect of the superhydrophobic, slightly hydrophobic, and superhydrophilic cathode gas flow field channels of PEM fuel cell performance have been explored as below;
    i. The superhydrophobic surface has shown the lowest pressure drop through a single channel, which is required to purge the water droplets out of the channel. This can be attributed to the low α (19±1°). Meanwhile, the hydrophobic coated channel has shown higher pressure drop. This is due to the droplets stickiness on the channel surfaces which can be caused by larger α (67±1°).

    ii. The slightly hydrophobic and superhydrophilic channels have resulted in slug and a thin film, respectively which increases the pressure drop values to purge the water out of the channel. This is caused by the higher interfacial tension between the channel's surface and liquid water ($\theta = 95\pm2°$, and $15\pm2°$, respectively).
    iii. The superhydrophobic coated gas flow channels have shown higher PEM fuel cell performance at high current densities compared to the slightly hydrophobic and superhydrophilic ones. This is attributed to better water removal capabilities from the cathode flow channels and less water accumulation in the cathode gas flow channels, which leads to better water management.

III. A novel design has been developed for the gas diffusion layer (GDL) used in the PEM fuel cell, is referred as sandwich wettability GDL. After it is coated with a silica particle/PDMS composite on both sides. It has been studied experimentally along with; 262 nm silica particles coated GDL (superhydrophilic), commercial GDL (PTFE coated with micro porous layer (MPL)), and non-coated GDL using SEM, Profilometry, method of standard porosimetry (MSP) and sessile drop technique to measure θ and α;
    i. Sandwich wettability GDL has demonstrated better air water transport at the same capillary pressure values and better cell performance, compared with superhydrophilic, commercial, and non-coated GDLs. This is attributed to better water management at higher current densities, which is caused by better water removal at higher current densities.

IV. A wettability gradient through the one side hydrophobic GDL plane has been introduced by coating one side of non-coated GDL with 15 wt. % PTFE solution. It has been experimentally studied using MSP to measure GDL characteristics and sessile drop technique to measure θ on the GDL surfaces. Water removal rate has been measured using syringe barrel with GDL token which is capped to the barrel at the finger flange side. The DI water is supplied into the barrel from the needle hub side.

Droplets dynamics' characteristics on the GDL surface have been studied using CCD camera. Three cells with different cathode GDL have been tested.

i. The wettability gradient through GDL plane has demonstrated significant improvements on air water transport and cell performance compared with the commercial and non-coated GDLs. This attributed to the driving capillary force gradient through GDL plane, which helps in driving the water from hydrophobic side to the more hydrophobic one of the GDL.

5.2 Future Work

I. Studying the effect of uniform surface wettability of gas flow channels from superhydrophilic to superhydrophobic on two-phase flow dynamics, resistance, and on PEM fuel cell performance have been conducted in this thesis. However, it is advisable to evaluate the effect of a gradient surface wettability from superhydrophilic to superhydrophobic along the gas flow channel surface on the two-phase flow dynamics, resistance, and on PEM fuel cell performance.

II. The wettability gradient through the cathode GDL plane has been evaluated in this thesis. It is recommended to study the wettability gradient through and in plane at the anode side and cathode side on water removal and PEM fuel cell performance.

III. In this research effects of gas flow channels surface wettability and cathode GDL wettability on PEM fuel cell performance are analyzed separately. Nevertheless, it is worthwhile to investigate the effect of wettability of both gas flow channels' surface and GDL simultaneously to explore the optimum surface wettability for both components. This will result in highest cell performance.

iv. Finally, the obtained experimental results for the two-phase flow inside the channels with different surface wettability provide a database for further numerical studies for the two-phase flow dynamics in PEM fuel cell industrial applications.

Bibliography

1. Cropper MAJ, Geiger S, Jollie DM. Fuel cells: a survey of current developments. Journal of Power Sources 2004,131:57-61.

2. Cabasso I, Yuan Y, Xu X. Gas diffusion electrodes based on poly (vinylidene fluoride) carbon blends. In: Google Patents; 1998.

3. Lim C, Wang CY. Effects of hydrophobic polymer content in GDL on power performance of a PEM fuel cell. Electrochimica Acta 2004,49:4149-4156.

4. Barbir F, ScienceDirect (Online service). PEM fuel cells theory and practice. In: Sustainable world series. Amsterdam ; London: Elsevier Academic; 2005. pp. xv, 433 p.

5. Quan P, Zhou B, Sobiesiak A, Liu ZS. Water behavior in serpentine micro-channel for proton exchange membrane fuel cell cathode. Journal of Power Sources 2005,152:131-145.

6. Wang Y, Wang CY, Chen KS. Elucidating differences between carbon paper and carbon cloth in polymer electrolyte fuel cells. Electrochimica Acta 2007,52:3965-3975.

7. Miller JD, Veeramasuneni S, Drelich J, Yalamanchili MR, Yamauchi G. Effect of roughness as determined by atomic force microscopy on the wetting properties of PTFE thin films. Polymer Engineering and Science 1996,36:1849-1855.

8. Girifalco LA, Good RJ. A Theory for the Estimation of Surface and Interfacial Energies .1. Derivation and Application to Interfacial Tension. Journal of Physical Chemistry 1957,61:904-909.

9. Nishino T, Meguro M, Nakamae K, Matsushita M, Ueda Y. The lowest surface free energy based on -CF3 alignment. Langmuir 1999,15:4321-4323.

10. NAKAJIMA A, HASHIMOTO K, WATANABE T. Transparent Super-hydrophobic Coating Films with Photocatalytic Activity. Photochemistry 1999,30:199-206.

11. Onda T, Shibuichi S, Satoh N, Tsujii K. Super-water-repellent fractal surfaces. Langmuir 1996,12:2125-2127.

12. Adamson AW, Gast AP, NetLibrary I. Physical chemistry of surfaces. 1997.

13. Wenzel RN. Surface Roughness and Contact Angle. Journal of Physical and Colloid Chemistry 1949,53:1466-1467.

14. Subramanian RS, Moumen N, McLaughlin JB. Motion of a drop on a solid surface due to a wettability gradient. Langmuir 2005,21:11844-11849.

15. Borup RL, Vanderborgh NE. Design and testing criteria for bipolar plate materials for PEM fuel cell applications. In; 1995. pp. 17-21.

16. Hermann A, Chaudhuri T, Spagnol P. Bipolar plates for PEM fuel cells: A review. International Journal of Hydrogen Energy 2005,30:1297-1302.

17. Cunningham N, Guay D, Dodelet JP, Meng Y, Hlil AR, Hay AS. New materials and procedures to protect metallic PEM fuel cell bipolar plates. Journal of the Electrochemical Society 2002,149:A905-A911.

18. Wang HL, Sweikart MA, Turner JA. Stainless steel as bipolar plate material for polymer electrolyte membrane fuel cells. Journal of Power Sources 2003,115:243-251.

19. Davies DP, Adcock PL, Turpin M, Rowen SJ. Bipolar plate materials for solid polymer fuel cells. Journal of Applied Electrochemistry 1999,30:101-105.

20. Wang HL, Turner JA. Ferritic stainless steels as bipolar plate material for polymer electrolyte membrane fuel cells. Journal of Power Sources 2004,128:193-200.

21. Mehta V, Cooper JS. Review and analysis of PEM fuel cell design and manufacturing. Journal of Power Sources 2003,114:32-53.

22. Joseph S, McClure JC, Chianelli R, Pich P, Sebastian PJ. Conducting polymer-coated stainless steel bipolar plates for proton exchange membrane fuel cells (PEMFC). International Journal of Hydrogen Energy 2005,30:1339-1344.

23. Cho E, Jeon US, Hong SA, Oh IH, Kang SG. Performance of a 1 kW-class PEMFC stack using TiN-coated 316 stainless steel bipolar plates. Journal of Power Sources 2005,142:177-183.

24. Hentall PL, Lakeman JB, Mepsted GO, Adcock PL, Moore JM. New materials for polymer electrolyte membrane fuel cell current collectors. Journal of Power Sources 1999,80:235-241.

25. Wind J, Spah R, Kaiser W, Bohm G. Metallic bipolar plates for PEM fuel cells. Journal of Power Sources 2002,105:256-260.

26. Woodman A, Jayne K, Anderson E, Kimble MC. Development of corrosion-resistant coatings for fuel cell bipolar plates. In: AMERICAN ELECTROPLATERS AND SURFACE FINISHERS SOCIETY INC; 1999. pp. 717-726.

27. Hung Y, El-Khatib K, Tawfik H. Testing and evaluation of aluminum coated bipolar plates of PEM fuel cells operating at 70 C. Journal of Power Sources 2006,163:509-513.

28. Hung Y, Tawfik H. Testing and evaluation of aluminum coated bipolar plates of PEM fuel cells operating at 70 degrees C. Proceedings of the 3rd International Conference on Fuel Cell Science, Engineering, and Technology 2005:141-144.

29. Akundy GS, Iroh J. Polypyrrole coatings on aluminum - synthesis and characterization. Polymer 2001,42:9665-9669.

30. Li MC, Luo SZ, Zeng CL, Shen JN, Lin HC, Cao CN. Corrosion behavior of TiN coated type 316 stainless steel in simulated PEMFC environments. Corrosion Science 2004,46:1369-1380.

31. Schrader ME. Ultrahigh vacuum techniques in the measurement of contact angles. IV. Water on graphite (0001). The Journal of Physical Chemistry 1975,79:2508-2515.

32. Lee SJ, Huang CH, Lai JJ, Chen YP. Corrosion-resistant component for PEM fuel cells. Journal of Power Sources 2004,131:162-168.

33. Taniguchi A, Yasuda K. Highly water-proof coating of gas flow channels by plasma polymerization for PEM fuel cells. Journal of Power Sources 2005,141:8-12.

34. Nakajima A, Hashimoto K, Watanabe T. Recent studies on super-hydrophobic films. Monatshefte Fur Chemie 2001,132:31-41.

35. BorroniBird CE. Fuel cell commercialization issues for light-duty vehicle applications. Journal of Power Sources 1996,61:33-48.

36. Mukundan R, Davey J, Fairweather JD, Spernjak D, Spendelow JS, Hussey DS, et al. Effect of Hydrophilic Treatment of Microporous Layer on Fuel Cell Performance. Proton Exchange Membrane Fuel Cells 8, Pts 1 and 2 2010,33:1109-1114.

37. Bevers D, Rogers R, vonBradke M. Examination of the influence of PTFE coating on the properties of carbon paper in polymer electrolyte fuel cells. Journal of Power Sources 1996,63:193-201.

38. Kumbur EC, Sharp KV, Mench MM. A design tool for predicting the capillary transport characteristics of fuel cell diffusion media using an artificial neural network. Journal of Power Sources 2008,176:191-199.

39. Paganin VA, Ticianelli EA, Gonzalez ER. Development and electrochemical studies of gas diffusion electrodes for polymer electrolyte fuel cells. Journal of Applied Electrochemistry 1996,26:297-304.

40. Giorgi L, Antolini E, Pozio A, Passalacqua E. Influence of the PTFE content in the diffusion layer of low-Pt loading electrodes for polymer electrolyte fuel cells. Electrochimica Acta 1998,43:3675-3680.

41. Wang ED, Shi PF, Du CY. Treatment and characterization of gas diffusion layers by sucrose carbonization for PEMFC applications. Electrochemistry Communications 2008,10:555-558.

42. Pai YH, Ke JH, Huang HF, Lee CM, Jyh-Myng Z, Shieu FS. CF4 plasma treatment for preparing gas diffusion layers in membrane electrode assemblies. Journal of Power Sources 2006,161:275-281.

43. Nguyen TV, White RE. A Water and Heat Management Model for Proton-Exchange-Membrane Fuel-Cells. Journal of the Electrochemical Society 1993,140:2178-2186.

44. Tuber K, Pocza D, Hebling C. Visualization of water buildup in the cathode of a transparent PEM fuel cell. Journal of Power Sources 2003,124:403-414.

45. Yang XG, Zhang FY, Lubawy AL, Wang CY. Visualization of liquid water transport in a PEFC. Electrochemical and Solid State Letters 2004,7:A408-A411.

46. Liu X, Guo H, Ma CF. Water flooding and two-phase flow in cathode channels of proton exchange membrane fuel cells. Journal of Power Sources 2006,156:267-280.

47. Kim HS, Ha TH, Park SJ, Min K, Kim M. Visualization study of cathode flooding with different operating conditions in a PEM unit fuel cell. Proceedings of the 3rd International Conference on Fuel Cell Science, Engineering, and Technology 2005:57-63.

48. Ma HP, Zhang HM, Hu J, Cai YH, Yi BL. Diagnostic tool to detect liquid water removal in the cathode channels of proton exchange membrane fuel cells. Journal of Power Sources 2006,162:469-473.

49. Atiyeh HK, Karan K, Peppley B, Phoenix A, Halliop E, Pharoah J. Experimental investigation of the role of a microporous layer on the water transport and performance of a PEM fuel cell. Journal of Power Sources 2007,170:111-121.

50. Gostick JT, Fowler MW, Ioannidis MA, Pritzker MD, Volfkovich YM, Sakars A. Capillary pressure and hydrophilic porosity in gas diffusion layers for polymer electrolyte fuel cells. Journal of Power Sources 2006,156:375-387.

51. Litster S, Sinton D, Djilali N. Ex situ visualization of liquid water transport in PEM fuel cell gas diffusion layers. Journal of Power Sources 2006,154:95-105.

52. Kumbur EC, Sharp KV, Mench MM. Liquid droplet behavior and instability in a polymer electrolyte fuel cell flow channel. Journal of Power Sources 2006,161:333-345.

53. Theodorakakos A, Ous T, Gavaises A, Nouri JM, Nikolopoulos N, Yanagihara H. Dynamics of water droplets detached from porous surfaces of relevance to PEM fuel cells. Journal of Colloid and Interface Science 2006,300:673-687.

54. Bazylak A, Sinton D, Djilali N. Dynamic water transport and droplet emergence in PEMFC gas diffusion layers. Journal of Power Sources 2008,176:240-246.

55. Owejan JP, Trabold TA, Jacobson DL, Arif M, Kandlikar SG. Effects of flow field and diffusion layer properties on water accumulation in a pem fuel cell. Icnmm2007: Proceedings of the 5th International Conference on Nanochannels, Microchannels, and Minichannels 2007:311-320.

56. Zhu W, Dunbar ZW, Masel RI. MicroCT X-ray imaging of water movement in a PEM fuel cell. Proton Exchange Membrane Fuel Cells 8, Pts 1 and 2 2008,16:995-1000.

57. Bazylak A, Heinrich J, Djilali N, Sinton D. Liquid water transport between graphite paper and a solid surface. Journal of Power Sources 2008,185:1147-1153.

58. Turhan A, Kim S, Hatzell M, Mench MM. Impact of channel wall hydrophobicity on through-plane water distribution and flooding behavior in a polymer electrolyte fuel cell. Electrochimica Acta 2010,55:2734-2745.

59. Wenzel RN. RESISTANCE OF SOLID SURFACES TO WETTING BY WATER. Industrial & Engineering Chemistry 1936,28:988-994.

60. Cassie ABD, Baxter S. Wettability of porous surfaces. Transactions of the Faraday Society 1944,40:546-551.

61. Gao L, McCarthy TJ. How Wenzel and Cassie Were Wrong. Langmuir 2007,23:3762-3765.

62. McHale G. Cassie and Wenzel: Were They Really So Wrong? Langmuir 2007,23:8200-8205.

63. Marmur A, Bittoun E. When Wenzel and Cassie Are Right: Reconciling Local and Global Considerations. Langmuir 2009,25:1277-1281.

64. Tsujii K, Yamamoto T, Onda T, Shibuichi S. Super oil-repellent surfaces. Angewandte Chemie-International Edition in English 1997,36:1011-1012.

65. Youngblood JP, McCarthy TJ. Ultrahydrophobic Polymer Surfaces Prepared by Simultaneous Ablation of Polypropylene and Sputtering of Poly(tetrafluoroethylene) Using Radio Frequency Plasma. Macromolecules 1999,32:6800-6806.

66. Feng XJ, Jiang L. Design and Creation of Superwetting/Antiwetting Surfaces. Advanced Materials 2006,18:3063-3078.

67. Ahn J, Holze R. Bifunctional electrodes for an integrated water-electrolysis and hydrogen-oxygen fuel cell with a solid polymer electrolyte. Journal of Applied Electrochemistry 1992,22:1167-1174.

68. Park G-G, Sohn Y-J, Yang T-H, Yoon Y-G, Lee W-Y, Kim C-S. Effect of PTFE contents in the gas diffusion media on the performance of PEMFC. Journal of Power Sources 2004,131:182-187.

69. Kennedy GL, Butenhoff JL, Olsen GW, O'Connor JC, Seacat AM, Perkins RG, et al. The toxicology of perfluorooctanoate. Critical reviews in toxicology 2004,34:351-384.

70. Sinclair E, Kim SK, Akinleye HB, Kannan K. Quantitation of Gas-Phase Perfluoroalkyl Surfactants and Fluorotelomer Alcohols Released from Nonstick Cookware and Microwave Popcorn Bags. Environmental Science & Technology 2007,41:1180-1185.

71. Wang Y, Al Shakhshir S, Li X. Development and impact of sandwich wettability structure for gas distribution media on PEM fuel cell performance. Applied Energy 2011,88:2168-2175.

72. Al Shakhshir S, Wang Y, Alaefour IE, Li X. The Influence of Channel Wettability on Two-Phase Flow and Polymer Electrolyte Membrane Fuel Cell Performance. Proton Exchange Membrane Fuel Cells 8, Pts 1 and 2 2012,42:109-115.

73. Camenzind A, Schweizer T, Sztucki M, Pratsinis SE. Structure & strength of silica-PDMS nanocomposites. Polymer 2010,51:1796-1804.

74. Kraus G. Reinforcement of elastomers by carbon black. Rubber Chemistry and Technology 1978,51:297-321.

75. Shim SE, Isayev AI. Rheology and structure of precipitated silica and poly (dimethyl siloxane) system. Rheologica Acta 2004,43:127-136.

76. Wang Y, Al Shakhshir S, Li X. Fabrication of Hydrophobic Coating on GDL with Silicone Based Materials. In: ECS; 2010.

77. Mehendale SS, Jacobi AM, Shah RK. Fluid Flow and Heat Transfer at Micro- and Meso-Scales With Application to Heat Exchanger Design. Applied Mechanics Reviews 2000,53:175-193.

78. Li X. Principles of fuel cells: Taylor & Francis; 2006.

79. Li XG, Sabir I, Park J. A flow channel design procedure for PEM fuel cells with effective water removal. Journal of Power Sources 2007,163:933-942.

80. Volfkovich YM, Bagotzky VS, Sosenkin VE, Blinov IA. The standard contact porosimetry. Colloids and Surfaces a-Physicochemical and Engineering Aspects 2001,187:349-365.

81. Li XG, Sabir M. Review of bipolar plates in PEM fuel cells: Flow-field designs. International Journal of Hydrogen Energy 2005,30:359-371.

82. Maharudrayya S, Jayanti S, Deshpande AP. Pressure losses in laminar flow through serpentine channels in fuel cell stacks. Journal of Power Sources 2004,138:1-13.

83. White FM. Fluid mechanics. 2nd ed. New York: McGraw-Hill; 1986.

84. Cverna F, ASM International. Materials Properties Database Committee. ASM ready reference. Thermal properties of metals. Materials Park, Ohio: ASM International; 2002.

85. Hydrogenics. Fuel Cell Automated Test Station User Guide In: S-Series Edited by Waterloo. U. 1 ed. Mississauga: Hydrogenics Corporation; 2003.

86. Qi Z, Kaufman A. Activation of low temperature PEM fuel cells. Journal of Power Sources 2002,111:181-184.

87. Holman JP. Experimental methods for engineers-7/E. 2001.

88. Kiuru M, Alakoski E. Low sliding angles in hydrophobic and oleophobic coatings prepared with plasma discharge method. Materials Letters 2004,58:2213-2216.

89. Murase H, Fujibayashi T. Characterization of molecular interfaces in hydrophobic systems. Progress in Organic Coatings 1997,31:97-104.

90. Miwa M, Nakajima A, Fujishima A, Hashimoto K, Watanabe T. Effects of the surface roughness on sliding angles of water droplets on superhydrophobic surfaces. Langmuir 2000,16:5754-5760.

91. Ranjan R, Brittain WJ. Combination of living radical polymerization and click chemistry for surface modification. Macromolecules 2007,40:6217-6223.

92. Liu KS, Yao X, Jiang L. Recent developments in bio-inspired special wettability. Chemical Society Reviews 2010,39:3240-3255.

93. Herminghaus S. Roughness-induced non-wetting. Europhysics Letters 2000,52:165-170.

94. Patankar NA. Mimicking the lotus effect: Influence of double roughness structures and slender pillars. Langmuir 2004,20:8209-8213.

95. Shibuichi S, Onda T, Satoh N, Tsujii K. Super water-repellent surfaces resulting from fractal structure. Journal of Physical Chemistry 1996,100:19512-19517.

96. Wang Y, Al Shakhshir S, Chen P, Li X. Preparation of super coating on graphite channel with silica particle/ poly(dimethylsiloxane)(PDMS) composite. In: International Green Energy Conference V. Waterloo, Ontario, Canada. ; June 01-03, 2010.

97. Johnson RE, Dettre RH. Contact Angle Hysteresis .3. Study of an Idealized Heterogeneous Surface. Journal of Physical Chemistry 1964,68:1744-&.

98. Dettre RH, Johnson R. Contact angle hysteresis II. Contact angle measurements on rough surfaces. Adv. Chem. Ser 1964,43:136-144.

99. Sheng XL, Zhang JH, Jiang L. Application of the Restricting Flow of Solid Edges in Fabricating Superhydrophobic Surfaces. Langmuir 2009,25:9903-9907.

100. Kim JW, Kim LU, Kim CK. Size control of silica nanoparticles and their surface treatment for fabrication of dental nanocomposites. Biomacromolecules 2007,8:215-222.

101. Callies M, Quere D. On water repellency. Soft Matter 2005,1:55-61.

102. Bonnet C, Didierjean S, Guillet N, Besse S, Colinart T, Carre P. Design of an 80 kWe PEM fuel cell system: Scale up effect investigation. Journal of Power Sources 2008,182:441-448.

103. Leelasupakorn H, Kaewchada A, Traisantikul W, Tiengtrakarnsuk W, Limtrakul S, Vatanatham T. Scaleup effect on performance of proton exchange membrane fuel cell. Chiang Mai Journal of Science 2008,35:89-94.

104. Nguyen TV, Lin G, Ohn H, Hussey D, Jacobson D, Arif M. Measurements of Two-Phase Flow Properties of the Porous Media Used in PEM Fuel Cells. Proton Exchange Membrane Fuel Cells 8, Pts 1 and 2 2006,3:415-423.

105. Gerteisen D, Heilmann T, Ziegler C. Enhancing liquid water transport by laser perforation of a GDL in a PEM fuel cell. Journal of Power Sources 2008,177:348-354.

106. Pasaogullari U, Wang CY. Two-phase transport and the role of micro-porous layer in polymer electrolyte fuel cells. Electrochimica Acta 2004,49:4359-4369.

107. Anderson WG. Wettability Literature Survey .2. Wettability Measurement. Journal of Petroleum Technology 1986,38:1246-1262.

108. Yan AH, Xiao XC, Kulaots I, Sheldon BW, Hurt RH. Controlling water contact angle on carbon surfaces from 5 degrees to 167 degrees. Carbon 2006,44:3116-3120.

109. Mathias MF, Roth J, Fleming J, Lehnert W. Diffusion media materials and characterisation. In: Handbook of Fuel Cells-Fundamentals, Technology and Applications: John Wiley & Sons, Ltd; 2003. pp. 517-537.

110. Gurau V, Bluemle MJ, De Castro ES, Tsou YM, Mann JA, Zawodzinski TA. Characterization of transport properties in gas diffusion layers for proton exchange membrane fuel cells - 1. Wettability (internal contact angle to water and surface energy of GDL fibers). Journal of Power Sources 2006,160:1156-1162.

111. Bazylak A, Sinton D, Liu ZS, Djilali N. Effect of compression on liquid water transport and microstructure of PEMFC gas diffusion layers. Journal of Power Sources 2007,163:784-792.

112. Berning T, Djilali N. A 3D, multiphase, multicomponent model of the cathode and anode of a PEM fuel cell. Journal of the Electrochemical Society 2003,150:A1589-A1598.

113. Manke I, Hartnig C, Grunerbel M, Lehnert W, Kardjilov N, Haibel A, et al. Investigation of water evolution and transport in fuel cells with high resolution synchrotron x-ray radiography. Applied Physics Letters 2007,90.

114. Lemons RA. Fuel-Cells for Transportation. Journal of Power Sources 1990,29:251-264.

115. Preli F. Technical Challenges for Fuel Cells in Mobile Applications. Fuel Cells 2002,2.

116. Maynard HL, Meyers JP. Miniature fuel cells for portable power: Design considerations and challenges. Journal of Vacuum Science & Technology B 2002,20:1287-1297.

117. Borup RL, Vanderborgh NE. Design and testing criteria for bipolar plate materials for PEM fuel cell applications. Materials for Electrochemical Energy Storage and Conversion - Batteries, Capacitors and Fuel Cells 1995,393:151-155.

118. Yang GH, Zhang Y, Kang ET, Neoh KG, Huan ACH, Lai DMY. Plasma polymerization of allylpentafluorobenzene on copper surfaces. Journal of Materials Chemistry 2002,12:426-431.

119. Ioroi T, Kitazawa N, Yasuda K, Yamamoto Y, Takenaka H. Iridium oxide/platinum electrocatalysts for unitized regenerative polymer electrolyte fuel cells. Journal of the Electrochemical Society 2000,147:2018-2022.